AUTOMATED APPROACHES FOR SNOW AND ICE COVER MONITORING USING OPTICAL REMOTE SENSING

by

David James Selkowitz

A dissertation submitted to the faculty of
The University of Utah
in partial fulfillment of the requirements for the degree of

Doctor of Philosophy

in

Geography

College of Social and Behavioral Science

The University of Utah

August 2017

The University of Utah Graduate School

STATEMENT OF DISSERTATION APPROVAL

The dissertation of **David James Selkowitz**

has been approved by the following supervisory committee members:

Richard Forster	, Chair	**2/3/2017** Date Approved
Phillip Dennison	, Member	**2/3/2017** Date Approved
Simon Brewer	, Member	**2/3/2017** Date Approved
Mitchell Power	, Member	**2/3/2017** Date Approved
Dennis Dye	, Member	**2/3/2017** Date Approved

and by **Andrea Brunelle** , Chair of

the Department of **Geography**

and by David B. Kieda, Dean of The Graduate School.

ABSTRACT

Snow and ice cover exhibits a high degree of spatial and temporal variability. Data from multispectral optical remote sensing instruments such as Landsat are an underutilized resource that can extend our ability for mapping these phenomena.

High resolution imagery is used to demonstrate that even at finer spatial resolutions (below 100 m), pixels with partial snow cover are common throughout the year and nearly ubiquitous during the meltout period. This underscores the importance of higher spatial resolution datasets for snow cover monitoring as well as the utility of fractional snow covered area (fSCA) monitoring approaches.

Landsat data are used to develop a fully automated approach for mapping persistent ice and snow cover (PISC). This approach relies on the availability of numerous Landsat scenes, an improved technique for automated cloud cover mapping, and a series of automated postprocessing routines. Validation at 12 test sites suggest that the automated PISC mapping approach provides a good approximation of debris-free glacier extent across the Arctic.

The PISC mapping approach is then used to produce the first single-source, temporally well-constrained (2010-2014) map of PISC across the conterminous western U.S. The Landsat-derived PISC map is more accurate than both a previously published dataset based on aerial photography acquired during the 1960s, 1970s

and 1980s and the National Land Cover Database (NLCD) 2011 extent of perennial snow and ice cover. Further analysis indicates differences between the newly developed Landsat-derived PISC dataset and the previously published glacier dataset can likely be attributed to changes in the extent of PISC over time.

Finally, in order to map mean annual snow cover persistence across the entire landscape, we implement a novel canopy adjustment approach designed to improve the accuracy of Landsat-derived fSCA in forested areas. In situ observations indicate canopy-adjusted snow covered area calculated from all available Landsat scenes can provide an accurate estimate of mean annual snow cover duration.

The work presented here lays the groundwork for addressing scientific questions regarding the spatial and temporal variability of snow cover, snow accumulation and ablation processes, and the impact of changes in snow cover on physical and ecological systems.

This dissertation is dedicated to Suka, superstar Siberian husky and connoisseur of fine snow conditions from Alaska to Utah and everywhere in between.

You will be missed.

TABLE OF CONTENTS

LIST OF TABLES

LIST OF FIGURES

ACKNOWLEDGEMENTS

I wish to acknowledge all members of my committee for all they have taught me. I also wish to acknowledge the USGS Land Remote Sensing Program for funding much of the research contained within this dissertation. Finally, I wish to thank Melanie Cota, who encouraged and supported me throughout the entire long process of earning a PhD.

CHAPTER 1

INTRODUCTION

Glaciers and seasonal snow cover serve as a crucial water resource across many regions of the world. Changes in glaciers and seasonal snow cover also serve as a key climate indicator across the globe and are particularly valuable where long term in situ measurements are unavailable. The quantity and timing of seasonal snow exerts a strong (and in some cases dominant) influence on a wide range of arctic, alpine, montane and boreal ecosystem processes, ranging from tree seedling establishment to ungulate travel routes and habitat selection.

At the broadest spatial scales (i.e., regional to global), existing remotely sensed and modeled data products provide a clear picture of the status and variability in snow and ice cover and have been used extensively in assessments of global and regional climate. The spatial resolution of the existing datasets (such as those derived from MODIS), however, is often insufficient to resolve much of the finer scale variability in snow and ice cover that impacts regional water supplies and ecological processes. For instance, a collection of late lying snow patches approximately 1 ha in size that would not typically be resolved in most regional to global scale snow cover products can provide substantial summer runoff or serve as

crucial habitat for caribou seeking refuge from mosquitos. Consequently, the ability to map and monitor snow and ice cover at finer spatial resolutions has the potential to provide major benefits for science and society.

The Landsat Thematic Mapper (TM), Enhanced Thematic Mapper Plus (ETM+), and Operational Land Imager (OLI) have provided a nearly continuous time series of optical remote sensing data appropriate for snow cover mapping across many regions of the globe since the mid 1980s. Landsat data have often been overlooked as a tool for snow cover monitoring because the 16-day interval between scene acquisitions is insufficient for many snow cover monitoring applications requiring a higher temporal resolution. However, the high spatial resolution (nominally 30 m) and extensive archive of scenes stretching back to the mid 1980s allow for a unique contribution to snow cover monitoring and snow hydrology. For many regions, the Landsat archive can be used to compute snow cover duration metrics (e.g., monthly and for the entire year for periods of 5 years or more) as well as the extent of glaciers and perennial snow cover.

In addition to this introduction and a concluding chapter, this dissertation is composed of four individual chapters which have been published or submitted as peer-reviewed journal manuscripts which address the potential for using data from Landsat or similar multispectral instruments for mapping and monitoring snow and ice cover at 30 m spatial resolution.

Chapter 2, “Prevalence of pure versus mixed snow cover pixels across spatial resolutions in alpine environments,” uses a combination of very high spatial resolution spaceborne imagery and in situ measurements to document the

frequency of partially snow-covered pixels in mountainous environments. The data presented in this chapter indicate that in mountain regions, pure snow cover pixels are rare at the scale of most regional to global datasets such as the MODIS snow cover products, and quite uncommon even at the Landsat spatial scale. The data show that even in locations where deep and spatially contiguous snowpacks accumulate during the winter, heterogeneity in accumulation and ablation processes results in extended periods during the spring and summer when Landsat scale pixels are partially snow covered. This underscores the utility of higher spatial resolution datasets, as well as the benefits of remote sensing approaches that provide estimates of fractional snow covered area for each pixel over more traditional approaches that only provide binary snow covered area.

Chapter 3, "An automated approach for mapping persistent ice and snow cover over high latitude regions," documents an approach developed for automated classification of glaciers and perennial snow cover across high latitude regions. A key development presented in this manuscript is a revised version of the CFMask algorithm for cloud masking optimized for use in mountainous regions where snow, ice, and rock surfaces are commonly located in close proximity to one another. Mixed areas of snow, ice and rock are frequently misclassified by the original version of the CFMask algorithm included with Landsat surface reflectance products. The revised cloud masking algorithm incorporates the original CFMask cloud cover classification but substantially reduces errors of commission for cloud cover.

Chapter 4, “Automated mapping of persistent ice and snow cover across the western US with Landsat,” expands upon the work presented in Chapter 2. In this manuscript, the approach developed in the previous chapter is adapted for use at lower latitudes and applied to the entire western conterminous United States. Validation of the persistent ice and snow cover (PISC) map using high spatial resolution imagery indicates the new dataset is more accurate than the 2011 National Land Cover Database snow/ice cover map and more accurate than a USGS atlas of glacier outlines compiled from topographic maps based on aerial photography. While the higher accuracy relative to the NLCD snow/ice cover class can be attributed to differences in mapping methods, the differences between the Landsat-derived PISC dataset and the dataset compiled from topographic maps appear to be due primarily to decreases in the extent of persistent ice and snow cover over time.

Chapter 5, “The USGS Landsat snow covered area products: methods and preliminary validation,” describes the development and validation of a new set of Landsat-derived snow covered area products. These products are now available for production on demand by user request and will eventually be included as standard products available alongside raw Landsat imagery and surface reflectance data. The Landsat snow covered area products include scene-based fractional snow covered area and canopy-adjusted fractional snow covered area as well as mean annual snow cover duration computed over the period 1986-2015. While viewable fractional snow covered area is validated in a separate publication, canopy adjusted fractional snow covered area for individual Landsat scenes is validated using a

network of in situ sensor arrays in the Sierra Nevada. Mean annual snow cover duration for the period 1986-2015, as well as for shorter 5-year periods, is validated using data from the SNOTEL network in California, Washington, and Wyoming. Results indicate that the RMSE for scene-based canopy-adjusted fSCA is 0.21, while the RMSE for 30-year mean annual snow cover duration is 14.7 days. The canopy adjustment approach introduced in this manuscript substantially improves accuracy and reduces bias for both scene-based fSCA and mean annual snow cover duration.

While the research presented in Chapters 2-5 focuses on the remote sensing and image processing approaches necessary for development and production of Landsat-derived snow and ice cover datasets, Chapter 6 briefly delves into the broader scientific questions that can be addressed using these datasets.

CHAPTER 2

PREVALENCE OF PURE VERSUS MIXED SNOW COVER PIXELS ACROSS SPATIAL RESOLUTIONS IN ALPINE ENVIRONMENTS

Selkowitz, D. J., Forster, R. R., & Caldwell, M. K. (2014). Prevalence of pure versus mixed snow cover pixels across spatial resolutions in alpine environments. *Remote Sensing*, *6*(12), 12478-12508. Published by MDPI 2014.

Remote Sens. **2014**, *6*, 12478-12508; doi:10.3390/rs61212478

OPEN ACCESS

remote sensing

ISSN 2072-4292

www.mdpi.com/journal/remotesensing

Article

Prevalence of Pure Versus Mixed Snow Cover Pixels across Spatial Resolutions in Alpine Environments

David J. Selkowitz [1,2,*], Richard R. Forster [2], and Megan K. Caldwell [3,4]

[1] US Geological Survey, Alaska Science Center, 4210 University Drive, Anchorage, AK 99508, USA

[2] Department of Geography, University of Utah, 260 S. Central Campus Dr., Room 270, Salt Lake City, UT 84112–9155, USA; E-Mail: rick.forster@geog.utah.edu

[3] US Geological Survey, Geosciences and Environmental Change Science Center, P.O. Box 25046, DFC, MS 980, Denver, CO 80225, USA; E-Mail: mcaldwell@usgs.gov

[4] Department of Ecology and Evolutionary Biology, University of Colorado, Campus Box 334, Boulder, CO 80339–0334, USA

* Author to whom correspondence should be addressed; E-Mail: dselkowitz@usgs.gov; Tel.: +1-907-786-7146; Fax: +1-907-786-7020.

External Editors: Ioannis Gitas and Prasad S. Thenkabail

Received: 2 October 2014; in revised form: 29 November 2014 / Accepted: 1 December 2014 / Published: 11 December 2014

Abstract: Remote sensing of snow-covered area (SCA) can be binary (indicating the presence/absence of snow cover at each pixel) or fractional (indicating the fraction of each pixel covered by snow). Fractional SCA mapping provides more information than binary SCA, but is more difficult to implement and may not be feasible with all types of remote sensing data. The utility of fractional SCA mapping relative to binary SCA mapping varies with the intended application as well as by spatial resolution, temporal resolution and period of interest, and climate. We quantified the frequency of occurrence of partially snow-covered (mixed) pixels at spatial resolutions between 1 m and 500 m over five dates at two study areas in the western U.S., using 0.5 m binary SCA maps derived from high spatial resolution imagery aggregated to fractional SCA at coarser spatial resolutions. In addition, we used *in situ* monitoring to estimate the frequency of partially snow-covered conditions for the period September 2013–August 2014 at 10 60-m grid cell footprints at two study areas with continental snow climates. Results from the image analysis indicate that at 40 m, slightly above the nominal spatial resolution of Landsat, mixed pixels accounted for 25%–93% of total pixels, while at 500 m, the nominal spatial resolution of MODIS bands used for snow

cover mapping, mixed pixels accounted for 67%–100% of total pixels. Mixed pixels occurred more commonly at the continental snow climate site than at the maritime snow climate site. The *in situ* data indicate that some snow cover was present between 186 and 303 days, and partial snow cover conditions occurred on 10%–98% of days with snow cover. Four sites remained partially snow-free throughout most of the winter and spring, while six sites were entirely snow covered throughout most or all of the winter and spring. Within 60 m grid cells, the late spring/summer transition from snow-covered to snow-free conditions lasted 17–56 days and averaged 37 days. Our results suggest that mixed snow-covered snow-free pixels are common at the spatial resolutions imaged by both the Landsat and MODIS sensors. This highlights the additional information available from fractional SCA products and suggests fractional SCA can provide a major advantage for hydrological and climatological monitoring and modeling, particularly when accurate representation of the spatial distribution of snow cover is critical.

Keywords: remote sensing of snow cover; snow-covered area; mixed pixels; spatial resolution; Landsat; MODIS

1. Introduction

Remotely sensed snow-covered area (SCA) provides crucial information for scientists across a variety of disciplines. SCA can be used along with ancillary data to estimate the spatial distribution of snow water equivalent (SWE) [1–4] and can be assimilated into hydrological and land surface model runs to improve model accuracy [5,6]. The presence of an insulating snow cover also has a large effect on ground surface temperatures and permafrost [7,8] as well as drainage characteristics [9], and thus SCA time series data can provide important information for scientists monitoring and modeling permafrost and soil conditions. Finally, snow cover can have a large impact on plant species distribution [10,11], plant phenology [12], and animal movement patterns [13–15], and thus SCA data can provide valuable information for ecologists and wildlife biologists.

Remote sensing of SCA has been conducted for nearly four decades using a variety of techniques and platforms. While the earlier efforts, as well as many more recent efforts, have focused on monitoring binary SCA (*i.e.*, the presence/absence of snow cover within each pixel) [16–21], several approaches have been developed to monitor the per-pixel snow cover fraction, often referred to as fractional SCA or fSCA [22–26]. Fractional SCA mapping extracts more information than binary SCA mapping from the same source dataset and, for the MODIS instrument, 500 m fSCA from the MODIS Snow-Covered Area and Grain Size (MODSCAG) algorithm has been demonstrated to more accurately represent SCA imaged at finer spatial resolutions with Landsat [27]. Fractional SCA mapping is, however, more difficult to implement, typically requiring more complicated algorithms as well as additional computational resources, and it may be more difficult to validate than binary SCA data. Additionally, some types of data possibly suitable for binary SCA mapping may not be suitable for fractional SCA mapping, such as panchromatic imagery or Landsat Multi-Spectral Scanner (MSS) imagery. While fractional SCA mapping can provide major advantages in some cases, such as with coarse resolution

sensors and when snow cover exhibits fine scale heterogeneity, in other cases, such as with very fine resolution sensors and where snow cover is homogenous across large areas, fractional SCA monitoring may not offer the same advantages.

One of the primary factors in determining whether or not a fractional mapping approach is necessary or highly beneficial is the prevalence of mixed pixels. The effect of spatial resolution on remotely sensed maps of land surface phenomena, including the prevalence of mixed pixels and the relationship between accuracy and spatial resolution, has been well documented in the remote sensing literature [28–34]. Fractional mapping approaches have been used for monitoring a wide range of cover types and environmental phenomena for several decades [22–26,35–39]. Nevertheless, production and widespread usage of standard (non-fractional) classification products has continued. This is at least partly because the benefits of fractional remote sensing datasets depend on the spatial resolution of the imagery and the spatial distribution characteristics of the phenomenon of interest. Snow cover has its own spatial distribution and scaling characteristics, which depend heavily on meteorological conditions and terrain. While extensive research has been conducted on the spatial distribution and scaling characteristics of snow [40–45] to our knowledge, the question of how these affect the choice of remote sensing approach at fine to moderate spatial resolutions has not been explicitly addressed. In order to better understand when, where, and at which spatial resolutions fractional SCA mapping would be most and least beneficial relative to binary SCA mapping, we quantified the frequency of mixed snow-covered/snow-free pixels across resolutions, over time, and at sites with different snow climate regimes. Our analysis is limited to high-elevation alpine environments, where remote sensing is particularly crucial due to the paucity of ground-based monitoring and where estimation of SCA is not significantly affected by vegetation canopies.

Our analysis covers spatial resolutions between 1 m and 500 m, but we focus our analysis on the spatial resolutions most relevant to the Landsat and MODIS sensors, with nominal spatial resolutions of 30 m and 500 m, respectively. For our analysis, we aggregate finer spatial resolution data to coarser spatial resolutions, a well-established approach to simulating coarser spatial resolution pixels in both remote sensing and modeling [27,28,34]. We employ this approach to estimate the frequency of mixed pixels across spatial resolutions for five dates between 2010 and 2014 at maritime and continental snow climate study areas.

An alternate approach to characterization of conditions across a remotely sensed or modeled pixel footprint is to collect *in situ* data at point locations throughout the pixel footprint and use the point data to characterize the aggregate conditions across the pixel. We also employ this approach, using arrays of temperature data loggers to monitor the daily snow cover fraction between September 2013 and August 2014 at ten 60 × 60 m grid cell footprints at two alpine study areas. The fractional SCA time series from these sites allows us to provide a more precise estimate of the temporal frequency of days with partial snow cover at the 60 m pixel resolution, as well as to identify and estimate the length of the transition period between fully snow-covered and fully snow-free conditions at sites with deep winter snowpacks.

2. Study Area and Methods

Our study areas consisted of two *in situ* (field) study areas (FSAs) in the Rocky Mountains of Colorado and two separate imagery study areas (ISAs) in the Rocky Mountains of Colorado and the

Oregon Cascades (Figure 1). Under ideal circumstances, *in situ* snow cover monitoring and analysis of high resolution image data would have occurred at the same locations. The need for cloud-free, high spatial resolution imagery from five dates spanning a wide variety of snow cover conditions at an alpine location, however, severely constrained the areas where this sort of analysis would be feasible. Both locations where we were able to obtain imagery meeting the above specifications were difficult to access and managed primarily as wilderness (where installation of sensors is typically discouraged or prohibited). Therefore, we opted to conduct our *in situ* analysis and image-based analysis at separate study areas.

2.1. Imagery Study Areas

The two ISAs, both located in the Western United States, consist of an alpine area in the Cascade Mountains in Oregon and an alpine area in the Rocky Mountains in Colorado (Figure 1). While the Oregon Cascades ISA exhibits a maritime snow climate characterized by winter temperatures near 0 °C and abundant precipitation, the Rocky Mountain National Park ISA exhibits a continental snow climate characterized by winter temperatures well below 0 °C and substantially less precipitation. Geographic and climatic characteristics of the two ISAs are shown in Table 1. While temperature and precipitation estimates are derived from the PRISM dataset [46], mean wind speed estimates were calculated from wind speed data collected at the nearest meteorological stations similar in elevation to the study area with available wind speed data. The Oregon Cascades ISA is located along the eastern slopes of the Three Sisters (a group of three volcanic peaks) in central Oregon (Figure 2a). Land cover consists of barren, rocky slopes with some herbaceous vegetation, several small lakes covering < 10 hectares each, and a few small glaciers and perennial snow patches, the largest covering < 0.5 km^2, amounting to < 14% of the total study area (determined by the total snow cover fraction on 1 September 2013, which most likely included substantial areas of late-lying seasonal snow cover). Patches of trees also cover approximately 1% of the study area. The Rocky Mountain NP ISA is located within Rocky Mountain National Park in central Colorado (Figure 2b). Land cover consists of barren, rocky slopes interspersed with herbaceous and dwarf shrub vegetation, along with a handful of small glaciers and perennial snow patches, none larger than 0.1 km^2.

Table 1. Geographic and climatic characteristics for each study area. Climatic characteristics are derived from the PRISM Climate Dataset [46].

Attribute	Oregon Cascades ISA	Rocky Mountain NP ISA	Cinnamon Pass FSA	Niwot Ridge FSA
Area	9.7 km^2	7.7 km^2	-	-
Elevation	2124 to 3157 m	3081 to 3910 m	3669 to 3864 m	3425 to 3666 m
Mean January Temperature (1981–2010)	−5.9 to −4.3°C	−11.5 to −9.7°C	−9.7 to −8.6°C	−10.7 to−9.4°C
Mean July Temperature (1981–2010)	8.8 to 12.1°C	8.4 to 11.0°C	8.4 to 10.0°C	9.3 to 11.1°C
Mean Annual Precip. (1981–2010)	2318 to 3737 mm	1066 to 1195 mm	1169 to 1329 mm	1017 to 1068 mm

Table 1. *Cont.*

Attribute	Oregon Cascades ISA	Rocky Mountain NP ISA	Cinnamon Pass FSA	Niwot Ridge FSA
Mean January Wind Speed (2005–2010) *	3.2 m/s *	11.9 m/s **	6.9 *** m/s	11.9 m/s **
Mean July Wind Speed (2005–2010)	3.6 m/s *	4.6 m/s **	4.5 *** m/s	4.6 m/s **

* Mean wind speed for Oregon Cascades ISA calculated from hourly data from Round Mountain RAWS, elevation 1798 m, maintained by the U.S. Forest Service and archived at the Western Regional Climate Center [47]. ** Mean wind speed for Rocky Mountain NP ISA and Niwot Ridge SA calculated from daily data from Niwot Ridge LTER Saddle Meteorological Station, elevation 3525 m, archived at the Niwot Ridge LTER [48]. *** Mean wind speed for Cinnamon Pass SA calculated from daily data from Putney Study Plot, elevation 3756 m, maintained by the Center for Snow and Avalanche Studies [49].

Figure 1. Study area locations in the Western United States. The Oregon Cascades ISA is located in Oregon while the Rocky Mountain NP ISA, Niwot Ridge FSA, and Cinnamon Pass FSA are located in Colorado.

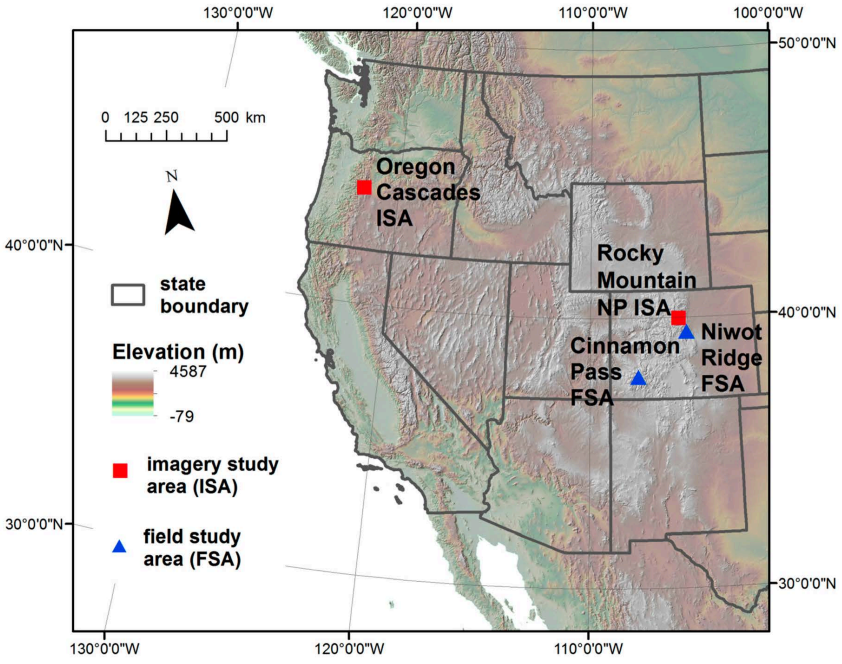

Figure 2. (**a**) Oregon Cascades ISA and (**b**) Rocky Mountain NP ISA. Extent of ISA is outlined in red, while the extent of high-relief subsets are outlined in blue and low-relief subsets are outlined in orange. Image sources: Digital elevation models for both study areas are from the National Elevation Dataset (NED) [50]. Draped imagery for the Oregon Cascades ISA is from 0.4 m pan-sharpened natural color WorldView 2 imagery, acquired 1 September 2013. Draped imagery for the Rocky Mountain NP ISA is from 1 m aerial orthoimagery available from the National Map [51], precise acquisition date not available.

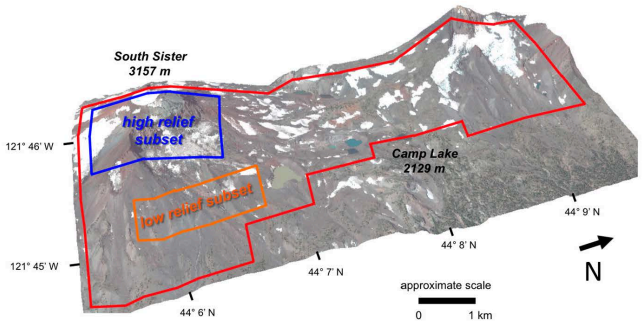

a. Oregon Cascades ISA

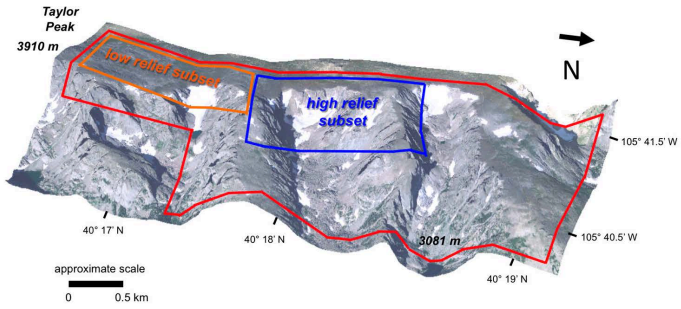

b. Rocky Mountain NP ISA

2.2. Image Data

High spatial resolution imagery used for classification of snow-covered area in each ISA was derived from the WorldView-1 and WorldView-2 earth observation satellites operated by DigitalGlobe corporation. WorldView-1 was launched in 2007 and acquires panchromatic imagery at a nominal spatial resolution of 0.5 m, while WorldView-2 was launched in 2009 and acquires panchromatic imagery at a nominal spatial resolution of 0.46 m and multispectral imagery at a nominal spatial resolution of 1.84 m. For each ISA, we selected five dates (Table 2) when mostly cloud-free WorldView-1 or WorldView-2 image strips covering our study areas were available from the EnhancedView archive provided by DigitalGlobe. For each date selected, we acquired high spatial resolution panchromatic (WorldView-1) or natural color pan-sharpened (WorldView-2) orthorectified image strips. The final analysis extent

boundary for each ISA was defined by the availability of cloud-free imagery for all five of the selected image dates as well as the extent of non-forested terrain. We excluded areas with forest cover from our analysis because for this study, we wanted to focus our analysis on the frequency of mixed pixels resulting from partially snow-covered ground, rather than mixed pixels that might occur when forest canopy is present above snow-covered ground. Areas with cloud cover on any of the five dates as well as areas with any significant forest cover were excluded from the analysis extent, resulting in the final analysis extents shown in Figure 2. Image strips were clipped to the extent of the study area boundary and resampled from the delivered panchromatic or pan-sharpened image product (~0.4 m resolution, with bands other than the panchromatic band acquired at ~1.9 m resolution) to 0.5 m resolution using nearest neighbor resampling prior to further processing. Resampling to 0.5 was done to maintain consistency with a larger database of 0.5 m resolution images not used in this study.

Table 2. Study area, image type, date, snow cover fraction, 0.5 m binary SCA classification accuracy, and recent snowfall history (in terms of snow water equivalent, SWE) for each WorldView (panchromatic) or WorldView-2 (3 band) image strip included in the analysis.

Location	Image Type	Acquisition Date	Snow Cover Fraction	0.5 m Classification Accuracy	2 Day Snowfall (mm SWE)*	10 Day Snowfall (mm SWE)*
Oregon	3-band	12 May 2011	0.93	92%	0	0
Oregon	panchromatic	15 July 2011	0.67	98%	0	0
Oregon	3-band	1 September 2013	0.14	92%	0	0
Oregon	panchromatic	29 November 2011	0.90	89%	0	36
Oregon	3-band	26 December 2013	0.93	89%	8	15
Colorado	3-band	26 February 2014	0.83	87%	3	46
Colorado	3-band	20 March 2010	0.93	93%	23	28
Colorado	panchromatic	7 May 2011	0.83	81%	0	16
Colorado	3-band	26 May 2012	0.42	85%	0	0
Colorado	3-band	29 September 2013	0.52	91%	3	6

* Recent snowfall history in table 2 is calculated from snowpack telemetry (SNOTEL) station data at nearby sites. Oregon Cascades ISA snowfall history was derived from Three Creeks Meadow, elevation 1734 m. Rocky Mountain NP ISA snowfall history was derived from Bear Lake, elevation 2896 m.

2.3. Image Processing Techniques

We used a version of the ISODATA algorithm [52] to create an unsupervised classification with 7–9 spectral classes for each image date for each ISA with multispectral imagery available. Spectral classes were determined through visual examination to represent primarily snow-covered or primarily snow-free pixels. For the three dates where only panchromatic image data was available, we visually determined the most appropriate value to distinguish between snow-covered and snow-free pixels. In all cases, initial classifications resulting from either the ISODATA classification approach or the threshold classification approach required further adjustment. Steep topography at both study sites resulted in variable illumination, necessitating manual editing in order to accurately map the extent of snow cover for each image date. Results from the original classifications were examined carefully and polygons identifying areas where the original classification did not accurately represent the presence or absence of snow cover

were manually identified. The majority of pixels misclassified in the original classification were in areas with topographic shading. We used a 500 × 500 m grid to ensure all portions of the image were examined for areas requiring manual editing. The manually identified polygons indicating incorrectly classified pixels were then used to revise the original classification, resulting in the final binary SCA classification used for subsequent analysis.

We conducted a basic accuracy assessment of each 0.5 m binary SCA classification. For the accuracy assessment, we used an image analyst who had not been involved in the production of the binary snow cover classifications. The analyst identified snow cover presence or absence at separate sets of 100 randomly selected 0.5 m pixels for each date at each ISA based on visual interpretation of the 0.5 m panchromatic WorldView-1 or 0.5 m pan-sharpened natural color WorldView-2 imagery. Snow cover presence/absence identified by the analyst was compared to the 0.5 m binary snow cover classification values at the corresponding pixel locations for each classified image and used to calculate an estimate for overall classification accuracy for each date at each ISA.

2.4. Snowfall History for Each Date

Significant snow accumulation can quickly transform a patchy snow-covered landscape, where mixed pixels occur frequently, into a fully (or nearly fully) snow-covered landscape, where mixed pixels are rare or absent. This transformation from a landscape with abundant mixed pixels to one with few or none is even more likely if the new snowfall moisture content is high and wind speeds remain relatively low. Thus recent snowfall history is a key factor that can influence SCA and the prevalence of mixed snow-covered/snow-free pixels across the landscape. In order to inform our analysis of mixed pixel prevalence, we estimated two-day and 10-day snowfall accumulation totals (in mm of snow water equivalent, often referred to as SWE) prior to each image acquisition date at each ISA using data from nearby snowpack telemetry (SNOTEL) sites. Recent snowfall for the Oregon Cascades ISA was estimated using data from the Three Creeks Meadow SNOTEL station 10 km east of the ISA at an elevation of 1734 m, while recent snowfall for the Rocky Mountain NP ISA was estimated using data from the Bear Lake SNOTEL station 3 km east of the ISA at an elevation of 2896 m. We calculated daily new SWE accumulation as the difference between SWE reported at 12 p.m. on the current and previous day and reported new total new snow accumulation for the two-day and 10-day periods prior to the date of image acquisition.

2.5. Analysis of Snow-Covered Area Images

We used the high spatial resolution binary SCA classifications to calculate several metrics for each date from each ISA, including total snow cover fraction for the ISA and the fraction of mixed (partially snow-covered) pixels across a range of spatial resolutions between 1 m and 500 m. Based on the original binary snow cover image, where the value of s at pixel p is 1 for snow-covered pixels and 0 at snow-free pixels, fSCA, the fractional snow-covered area for pixel sizes larger than the original binary spatial resolution (0.5 m in this case) was calculated using Equation (1):

$$\text{fSCA} = \frac{\sum_{p=1}^{p=n} s_p}{n} \quad (1)$$

$fSCA_{ISA}$, the snow cover fraction for the entire ISA, was calculated using the same approach, using all the high-resolution pixels within the ISA rather than only pixels within a smaller grid cell footprint corresponding to a specific spatial resolution. We calculated fSCA for each pixel size between 1 m and 500 m that could fit evenly (*i.e.*, with no remainder) into both the horizontal and vertical dimensions of the clipped ISA images. The Oregon Cascades ISA image dimensions were 12,000 × 4000 pixels, while the Rocky Mountain NP ISA image dimensions were 8000 × 4000 pixels. Pixel sizes used for calculation of the frequency of mixed pixel occurrence are indicated in Table 3, along with the resulting number of pixels at each spatial resolution within the ISA boundary. For our analysis, at each spatial resolution, pixels were considered mixed if fSCA was between 0.02 and 0.98. These threshold values were chosen instead of counting only pixels with all snow-covered or no snow-covered fine-resolution pixels as pure in order to reduce the effect of noise in the data. We calculated the fraction of mixed pixels for the ISA at each spatial resolution, fM_r, using Equation (2):

$$fM_r = \frac{\sum_{p=1}^{p=n} m_p \begin{cases} m_p = 0 & \text{for fSCA} < 0.02 \text{ and fSCA} > 0.98 \\ m_p = 1 & \text{for } 0.02 \leq \text{fSCA} \geq 0.98 \end{cases}}{n} \quad (2)$$

Table 3. Pixel sizes used to compute frequency of mixed pixels and corresponding pixel sample sizes for each ISA.

Pixel Size	Oregon Cascades ISA Sample Size	Rocky Mountain NP ISA Sample Size
1	7,925,962	6,812,343
2	1,981,062	1,702,693
2.5	1,267,546	1,089,691
4	494,784	425,503
5	316,572	272,312
8	123,625	106,267
10	79,021	67,957
12.5	50,496	43,513
16	30,765	26,495
20	19,661	16,931
25	12,598	10,859
40	4893	4203
50	3121	2705
62.5	1995	1723
80	1199	1037
100	767	666
125	491	425
200	187	162
250	113	102
400	42	39
500	27	24

Although the differences between minimum and maximum elevation at each ISA were similar (1033 m for the Oregon Cascades ISA and 829 m for the Rocky Mountain NP ISA), comparison of elevation semivariograms based on 10 m digital elevation data (Figure 3a) indicated higher semi-variance in

elevation at the Rocky Mountain NP ISA. In order to allow for comparison between the frequency of occurrence of mixed snow cover pixels at the ISAs that would not be biased by differences in topography, we selected a 1500 × 750 m high-relief subset from each ISA as well as a 1500 × 500 m low-relief subset from each study area (Figure 2). The elevation semivariograms for the high- and low-relief subsets from each study area are shown Figure 3b. For the high- and low-relief subsets at each study area, we repeated the analysis described above for spatial resolutions between 1 m and 125 m. The analysis for the subsets was constrained to 125 m pixels due to the smaller extent of the image subsets.

Figure 3. Semivariograms for elevation derived from 10 m DEM for (**a**) the Oregon Cascades and Rocky Mountain NP ISAs, and (**b**) high- and low-relief subsets from the Oregon Cascades and Rocky Mountain NP ISAs.

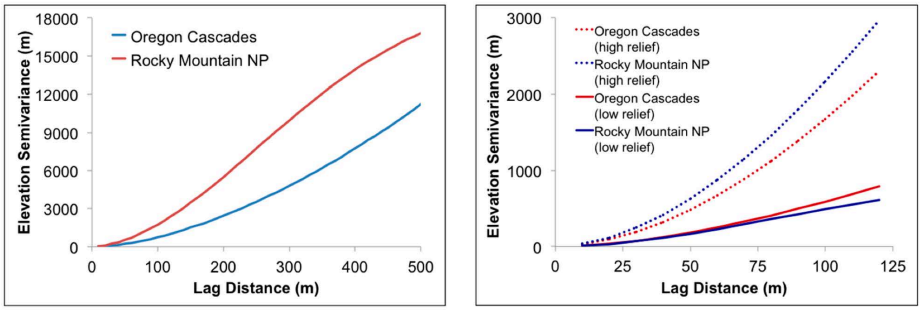

a. semivariance for full ISAs

b. semivariance for high and low relief subsets

In order to determine the potential for error in total study area snow cover fraction that might be introduced by monitoring binary SCA rather than fractional SCA at various spatial resolutions, we also calculated total ISA snow cover fraction based on binary SCA at spatial resolutions greater than the original 0.5 m resolution. To accomplish this, at each spatial resolution, *r*, we first calculated fSCA for each pixel at resolution *r* using Equation (1) and then calculated the binary SCA-derived study area snow cover fraction, bSCA_r using Equation (3):

$$\mathrm{bSCA}_r = \frac{\sum_{p=1}^{p=n} s_p \begin{cases} s_p = 0, & \text{for fSCA} < 0.5 \\ s_p = 1, & \text{for fSCA} \geq 0.5 \end{cases}}{n} \quad (3)$$

where *n* was equal to the total number of pixels at resolution *r* within the ISA. For this comparison, it was essential that nearly identical samples of high resolution pixels were used for calculations at all spatial resolutions considered. For this reason, we were unable to conduct this analysis at spatial resolutions > 250 m, since the irregularly shaped ISA analysis extent resulted in the elimination of a substantial number of high resolution pixels that fell within the analysis extent but also within an aggregated grid cell that extended beyond the boundary extent.

For the Rocky Mountain NP ISA, we conducted additional analysis to determine the overall frequency and spatial distribution of areas where a Landsat scale (~30 m) binary SCA representation characterizing pixels with ≥ 50% snow cover as snow-covered and pixels with < 50% snow cover as snow-free would be prone to error. We chose 40 m spatial resolution for this analysis because, of the pixel resolutions we

evaluated (shown in Table 3), the 40 m resolution offered the closest approximation of the estimated ground instantaneous field of view (GIFOV) for the Landsat TM instrument, which is slightly larger than the nominal spatial resolution of 30 m [53]. To map the spatial distribution of potential errors arising from the use of binary SCA, we calculated fSCA using Equation (1) for 40 m pixels, and then calculated $bSCA_{40\,m}$ for 400 m blocks corresponding with 10 × 10 arrays of 40 m pixels (rather than for the full ISA extent), using Equation (3). The position of the 10 × 10 (400 m) pixel blocks was determined by the ISA boundary, with the origin point for the grid located at the northwestern corner of the image. We then calculated fSCA for each 400 × 400 m block using the original 0.5 m resolution binary image and the approach described in Equation 1 and compared fSCA to $bSCA_{40m}$ at each block, calculating the mean absolute difference between fSCA and $bSCA_{40m}$. By comparing fSCA and $bSCA_{40m}$ at each block, we calculated the error that would be expected to occur for blocks of 100 40 m pixels if 40 m binary, rather than 40 m fractional SCA, was used. It is important to note that we were estimating differences that might arise from binary *vs.* fraction SCA mapping at 40 m spatial resolution, and in this case, 400 m was the size of the aggregation unit that corresponded to a 10 × 10 array of 40 m pixels, but not the spatial resolution of interest.

2.6. In Situ Snow Cover Monitoring Overview

In order to estimate the prevalence of partially snow-covered conditions for individual grid cells similar in size to Landsat pixels, we conducted *in situ* fractional SCA monitoring at 60 m grid cells at two field study areas in the Rocky Mountains of Colorado (Figure 1) between September 2013 and August 2014. *In situ* fractional SCA data collected at these footprints will be used as part of an ongoing effort for validation of a Landsat fractional SCA product currently under development, and consequently we opted for monitoring 60 m footprints rather than 30 m footprints (the nominal pixel size for Landsat). The 60 m footprint size was selected because the effective resolution of Landsat has been shown to be larger than the 30 m nominal resolution [53], and also because monitoring the larger 60 m footprint would reduce the impact of spatial registration errors on comparisons between *in situ* and remotely sensed data.

2.7. In Situ Snow Cover Monitoring Study Sites

At the first FSA, referred to from this point forward as the Cinnamon Pass FSA, we measured daily snow cover fraction over six 60 × 60 m footprints in the vicinity of Cinnamon Pass in the San Juan range of the Colorado Rocky Mountains (Figure 4a). Sites ranged in elevation from 3669 to 3864 m, with slope angles ranging from 11° to 28° (Table 3). Modeled mean annual precipitation at the study area for the period 1981–2010 computed from the PRISM climate dataset [46] ranged from 1169 to 1320 mm; mean January temperatures ranged from −9.7 °C to −8.6 °C and mean July temperatures ranged from 8.4 °C to 10.0° C for the same period.

Figure 4. Locations for 60 × 60 m grid cells instrumented with arrays of temperature data loggers at (**a**) the Cinnamon Pass FSA and (**b**) the Niwot Ridge FSA.

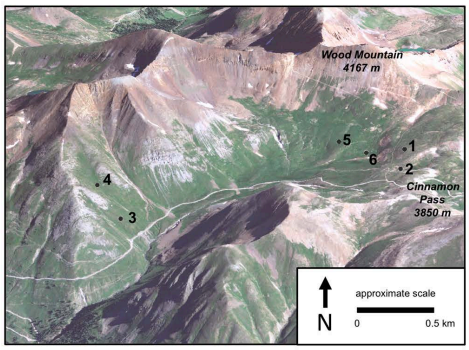

a. Cinnamon Pass Study Area

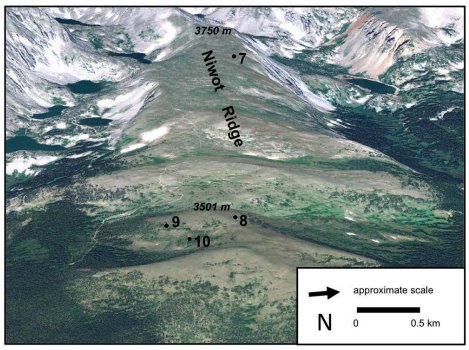

b. Niwot Ridge Study Area

At the second FSA, referred to from this point forward as the Niwot Ridge FSA, we measured daily snow cover fraction at four 60 × 60 m footprints at and above the alpine tree line on Niwot Ridge (Figure 4b), located about 3 km east of the continental divide in the Rocky Mountains west of Boulder, Colorado. Footprints at the Niwot Ridge FSA ranged in elevation from 3425 to 3666 m and included slope angles from 10°–19° (Table 4). While two of the four sites were > 200 m above tree line and included only herbaceous and dwarf shrub vegetation, two sites were within 20 m of stunted spruce and fir trees, which could be found throughout the area above the upper limit of contiguous upright forest. Modeled mean annual precipitation at the study area for the period 1981–2010 computed from the PRISM climate dataset ranged from 1017 to 1068 mm, with mean January temperatures ranging from −10.7 °C to −9.4 °C and mean July temperatures ranging from 9.3 °C to 11.1 °C for the same period (Table 3).

Table 4. Study area location and site characteristics for 60 × 60 m grid cell footprints where *in situ* monitoring was conducted. CP indicates Cinnamon Pass, while NR indicates Niwot Ridge.

Site	Field Study Area	Elevation (m)	Slope (Degrees)	Aspect	Land Cover	Local Topographic Position
1	CP	3850	11	W	rocky alpine meadow	ridgetop
2	CP	3845	15	NW	rocky alpine meadow	ridgetop
3	CP	3669	28	SE	alpine meadow	mid-slope
4	CP	3784	27	E	alpine meadow	mid-slope
5	CP	3779	15	S	alpine meadow	mid-slope
6	CP	3776	12	NW	alpine meadow	valley
7	NR	3666	19	N	rocky alpine meadow	near ridgetop
8	NR	3496	10	N	rocky alpine meadow	ridgetop
9	NR	3425	19	S	talus slope	mid-slope
10	NR	3430	14	S	rocky alpine meadow	valley

2.8. In Situ Snow Cover Monitoring Approach

At each of 10 monitoring sites within our field study areas, we buried 16 HOBO Pendant temperature data loggers 2–5 cm below the soil surface (Mention of a particular product does not constitute endorsement by the U.S. federal government). At one site where the pixel footprint was dominated by a rocky talus slope, some data loggers were placed below rocks near the surface of the talus pile. Our placement of data loggers varied from the approach used by Raleigh *et al.* [54] in the spatial resolution of the footprint monitored (60 × 60 m in our study *vs.* 500 × 500 m in Raleigh *et al.* [54]), the number of sensors deployed, and the placement of sensors within the footprint. While Raleigh *et al.* [54] deployed between 37 and 89 sensors in several different sensor configurations, including quasi-regular grids and transects, all of which covered 500 × 500 m or larger areas, we used regular 4 × 4 grids with 20 m spacing at each site, for a total of 16 sensors covering each 60 × 60 m footprint (Figure 5).

Figure 5. Schematic diagram of the arrangement of temperature data loggers at each 60 × 60 m grid cell footprint. Data loggers are indicated by black circles.

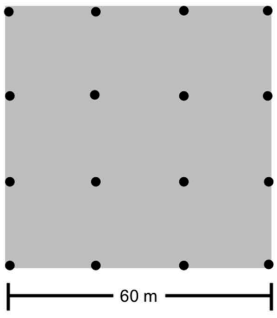

Each data logger recorded the temperature at 1.5-hourly intervals. At the Cinnamon Pass study area, loggers were installed in mid-September 2013 and collected in July–August 2014, while at the Niwot Ridge study area loggers were installed in mid-October 2013 and also collected in July–August 2014. While 16 temperature data loggers were installed at each site, in a few cases, we were unable to locate a buried temperature data logger, and in a few other cases, data loggers stopped recording due to malfunction or insufficient battery voltage. All data from temperature data loggers that stopped recording prior to retrieval were discarded in order to ensure that calculated snow cover fraction would be based on the same set of points for the entire monitoring period.

We used the algorithm introduced by Raleigh *et al.* [54] to convert the 1.5-hourly temperature time series from individual sensors to a daily snow cover fraction value for each 60 m grid cell footprint. Snow cover located above a sensor insulates the uppermost layer of the soil, resulting in a substantial reduction of the range in temperature variability experienced near the soil surface [7]. At temperate sites, in the absence of snow cover there is typically a strong diurnal ground temperature oscillation that disappears when snow cover is present. Monitoring this daily ground temperature variation allows for the identification of periods of snow cover using time series data collected at hourly to several hour increments [54–57]. Automated classification of periods with snow cover requires the selection of an appropriate 24-hour temperature range threshold; 24-hour periods where the temperature range is below this value will be classified as snow-covered. No single value has been established in the literature as appropriate for all conditions, as ground surface temperature variability is affected by a number of factors, including soil type, soil moisture, depth of burial, air temperature variability, and incoming solar radiation. We selected a 24-hour temperature range threshold of 2 °C, considerably larger than the temperature threshold used by Raleigh *et al.* and other studies [54–57]. Visual interpretation of temperature time series data suggested that this higher value allowed for identification of shallow snow cover during mid-winter while having minimal impact on the classification of snow cover conditions during the spring and summer melt period.

For each sensor that recorded data for the entire monitoring period, for each interval in the 1.5-hourly time series we calculated the difference between minimum and maximum temperatures recorded for the previous 24 h as well as the next 24 h in the time series. If the 24-hour temperature range value exceeded 2 °C for either the previous 24-hour period or the upcoming 24-hour period, the 1.5-hourly time series snow cover value was set to 0, indicating snow-free conditions. If the 24-hour temperature range values for both periods were less than 2 °C, the 1.5-hourly time series snow cover value was set to 1, indicating snow-covered conditions. Snow cover fraction on the ground at time series interval t, $\mathrm{fSCA_t}$ was then calculated for each interval in the time series using Equation (4):

$$\mathrm{fSCA_t} = \frac{\sum_{l=1}^{l=n} s_l}{n} \quad (4)$$

where s_l was binary snow presence, indicated by 1, or absence, indicated by 0, at temperature data logger l. We then computed the mean daily snow cover fraction for the footprint, $\mathrm{fSCA_d}$, using Equation (5):

$$\mathrm{fSCA_d} = \frac{\sum_{t=1}^{t=16} \mathrm{fSCA}_t}{16} \quad (5)$$

While we were not able to validate the methodology for monitoring grid cell snow cover fraction at any of the 60 m footprints in this study, photographic survey data collected at five 60 m footprints at

high-elevation subalpine forest and meadow sites in Utah and California indicated good agreement between photo-derived snow cover fraction and snow cover fraction calculated from similar grids of temperature data loggers using the same approach (mean absolute difference 0.09) [58].

In order to gauge the impact of the 24-hour temperature range value threshold on computed snow cover fraction, we conducted a sensitivity analysis where we computed the daily snow cover fraction using values of 0.5 °C, 1 °C, 2 °C and 3 °C. For each day in the time series, we calculated uncertainty in grid cell snow cover fraction, $fSCA_u$, by calculating the difference between snow cover fraction computed using the 0.5 °C threshold, $fSCA_{0.5}$, and snow cover fraction computed using the 3 °C threshold, $fSCA_{3.0}$, using Equation (6):

$$fSCA_u = fSCA_{3.0} - fSCA_{0.5} \quad (6)$$

$fSCA_u$ had a theoretical range from 0 (indicating no difference between snow cover fraction computed using a 0.5° C threshold and snow cover fraction computed using a 3 °C threshold) to 1 (indicating no snow cover computed using a 0.5 °C threshold and full snow cover computed using a 3 °C threshold).

3. Results

3.1. High Spatial Resolution Binary Snow-Covered Area

Binary SCA classifications at 0.5 m spatial resolution for the Oregon Cascades and Rocky Mountain NP ISAs are shown in Figures 6 and 7, with examples from each study area shown in Figure 8. Total study area snow cover fraction for each date from the two ISAs ranged from 0.143 to 0.943 (Table 2). Classification accuracy for the 0.5 m binary SCA classifications ranged from 81%–98%, with a mean of 90% for all 10 images (Table 2). Mean classification accuracy was slightly higher at the Oregon Cascades ISA (92.0%) than at the Rocky Mountain NP ISA (87.4%). Mean classification accuracy was very similar for the three dates where pan-sharpened three-band imagery was used (89.9%) and the three dates where panchromatic imagery was used (89.3%)

3.2. Prevalence of Mixed Pixels across Spatial Resolutions and between Study Areas

The fraction of mixed pixels at spatial resolutions between 1 m and 500 m is shown in Figure 9. At 40 m spatial resolution, slightly larger than the estimated GIFOV for Landsat at nadir, mixed pixels accounted for 25%–50% of total pixels at the Oregon Cascades ISA (mean of 36% for five dates), and 41%–93% of total pixels at the Rocky Mountain NP ISA (mean of 69% for five dates). At 500 m, the nominal spatial resolution for MODIS, mixed pixels accounted for 67%–93% of total pixels at the Oregon Cascades ISA (mean of 81% for five dates) and from 79%–100% of total pixels at the Rocky Mountain National Park ISA (mean of 93% for five dates). While the fraction of mixed pixels varied substantially across the available imagery dates for each ISA, the fraction of mixed pixels was consistently higher at the Rocky Mountain NP ISA than at the Oregon Cascades ISA.

Figure 6. WorldView imagery (**top row**) and high-resolution binary snow-covered area maps (**bottom row**) for the Oregon Cascades ISA. Panchromatic band data is displayed for the 15 July 2011 and 29 November 2013 images, while red band data is displayed for the 12 May 2011, 1 September 2013, and 26 December 2013 images.

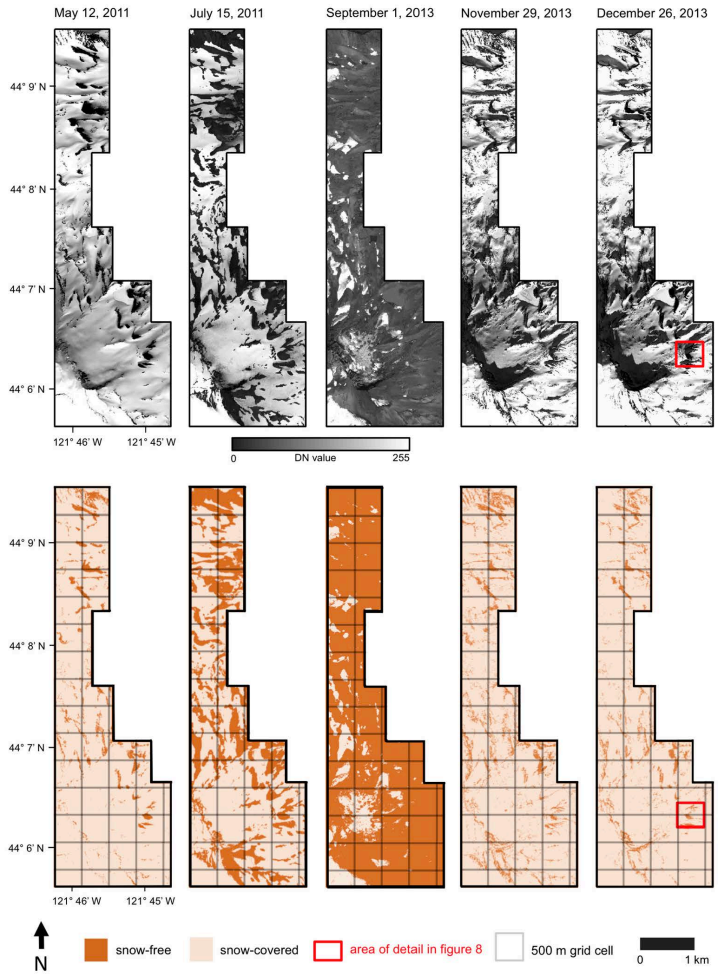

Figure 7. WorldView imagery **(top row)** and high-resolution binary snow-covered area maps **(bottom row)** for the Rocky Mountain NP ISA. Panchromatic band data is displayed for 7 May, while red band data is displayed for the 26 February 2014, 20 March 2010, 26 May 2012, and 29 September 2013 images.

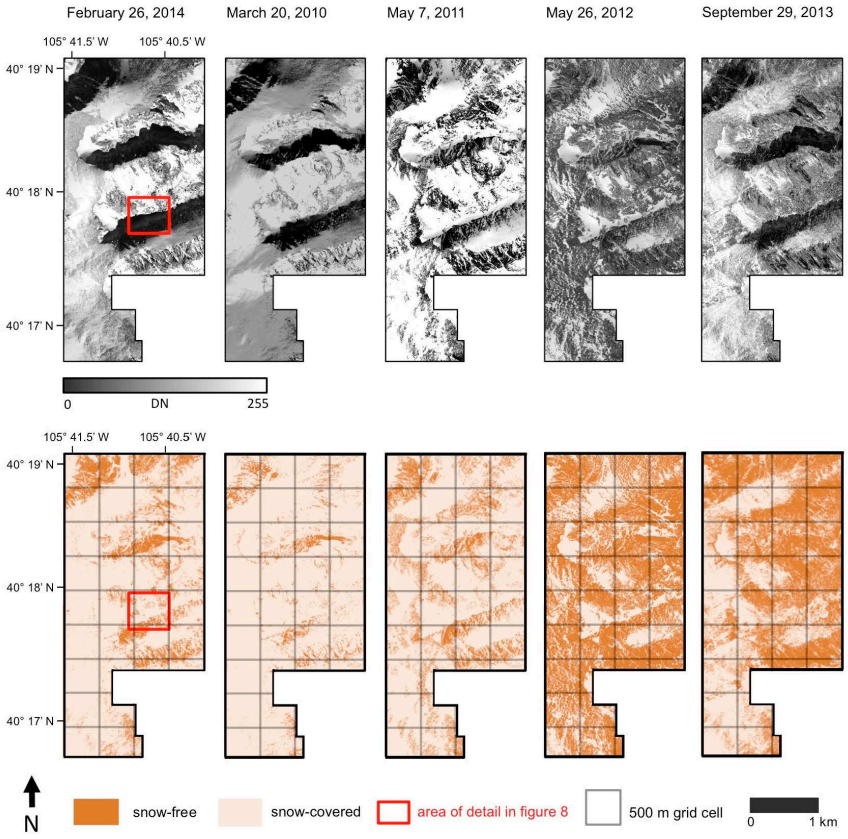

Figure 8. Examples of 0.5 m binary snow-covered area classifications (**right side**) based on WorldView 2 imagery (**left side**). Oregon Cascades, 26 December 2013, (panels **a** and **b**) and Colorado Rocky Mountains, 26 February 2014 (panels **c** and **d**).

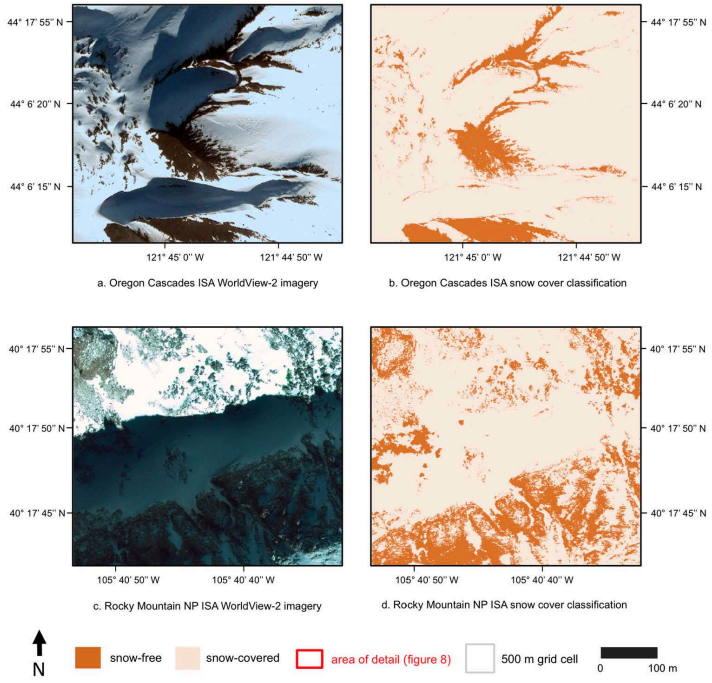

Figure 9. Fraction of mixed (partially snow-covered) pixels for pixel resolutions between 1 m and 500 m, for (**a**) the Oregon Cascades imagery study area, and (**b**) the Rocky Mountain NP imagery study area. Vertical blue lines indicate 40 m spatial resolution (slightly above the nominal spatial resolution for Landsat) and 500 m spatial resolution (the nominal spatial resolution for MODIS).

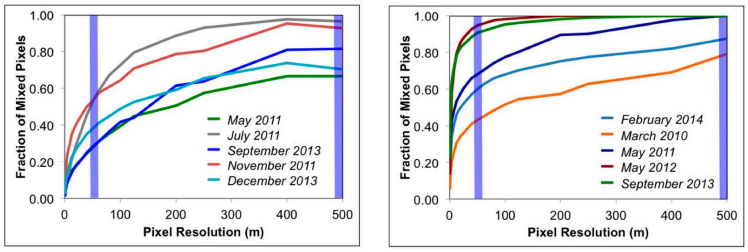

The high-relief subset from the Oregon Cascades ISA and the corresponding high-relief subset from the Rocky Mountain NP ISA exhibit similar semivariograms, while the low-relief subsets from the two study areas exhibit nearly identical semivariograms (Figure 3b). Comparisons of the fraction of mixed pixels at spatial resolutions between 1 m and 125 m indicate higher prevalence of mixed pixels at the Rocky Mountain NP ISA in both the high-relief and low-relief subsets (Figure 10).

Figure 10. (**a**) Fraction of mixed pixels for Oregon Cascades ISA high-relief subset, (**b**) fraction of mixed pixels for the Rocky Mountain NP ISA high-relief subset, (**c**) fraction of mixed pixels for the Oregon Cascades ISA low-relief subset, and (**d**) fraction of mixed pixels for the Rocky Mountain NP ISA low-relief subset. Vertical blue lines indicate 40 m, slightly above the nominal spatial resolution of Landsat.

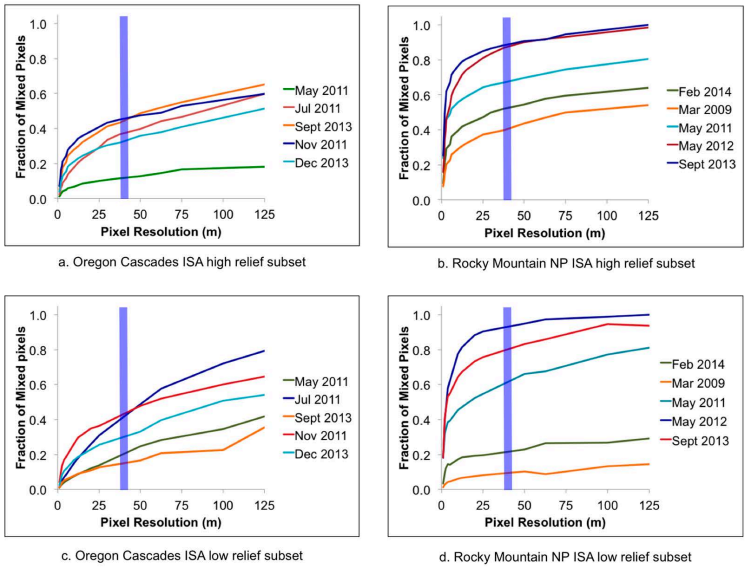

a. Oregon Cascades ISA high relief subset

b. Rocky Mountain NP ISA high relief subset

c. Oregon Cascades ISA low relief subset

d. Rocky Mountain NP ISA low relief subset

3.3. Differences between Binary and Fractional SCA

Our analysis indicated that as spatial resolution became coarser, the difference between study area snow cover fraction computed from binary SCA and fractional SCA, and thus the potential for error in binary SCA mapping, tended to increase (Figure 11). In general, if the 0.5 m snow cover fraction was > 0.6, binary snow cover fraction for the study area tended to increase at coarser spatial resolutions, while if the 0.5 m snow cover fraction was < 0.6, binary snow cover fraction for the study area tended to decrease at coarser spatial resolutions. While differences between study area snow cover fractions derived from binary versus fractional SCA were generally small, the change in study area snow cover fraction with spatial resolution was more significant for the July 2011 image from the Oregon Cascades ISA, with the study area snow cover fraction increasing from 0.67 at 0.5 m to 0.85 at 250 m.

Figure 11. Relationship between pixel resolution and total study area snow cover fraction derived from binary SCA for (**a**) Oregon Cascades ISA (**b**) and Rocky Mountain NP imagery ISA. Vertical blue lines indicate 40 m, slightly above the nominal spatial resolution of Landsat.

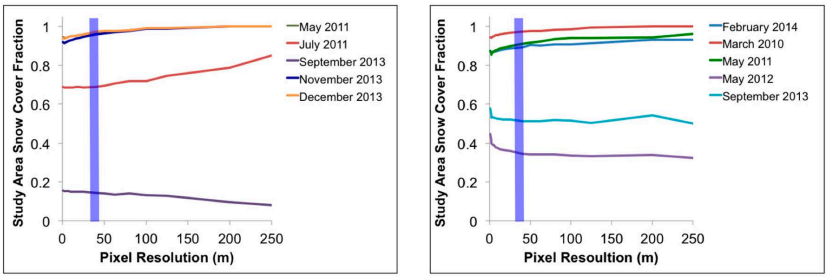

a. Oregon Cascades ISA b. Rocky Mountain NP ISA

Figure 12. Spatial distribution of 400 × 400 m blocks from the Rocky Mountain NP imagery study area where absolute differences between binary and fractional SCA were low (< 0.05), medium (0.05–0.10), high (0.10–0.15), and highest (> 0.15).

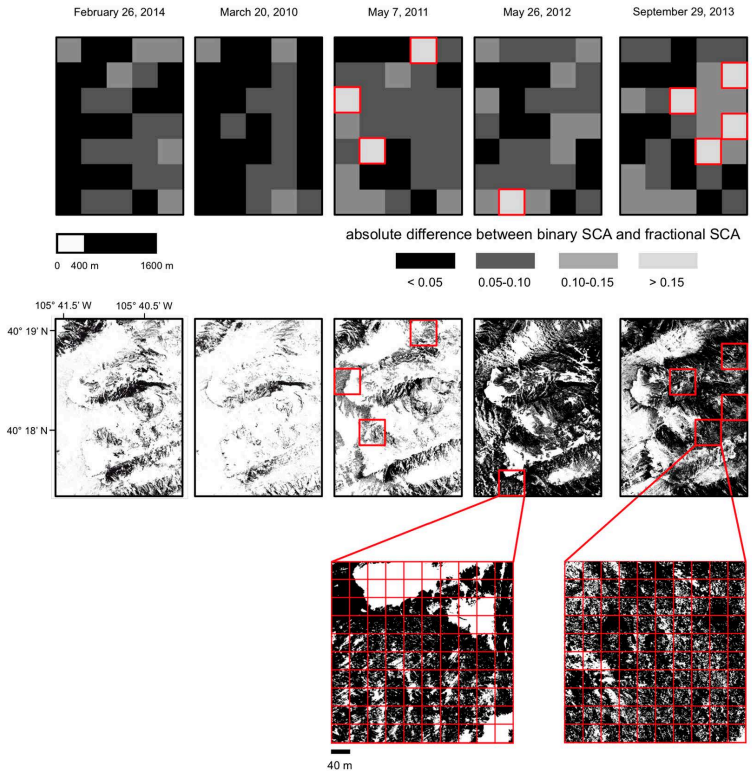

More detailed analysis of the spatial and temporal distribution of the differences between binary and fractional SCA at 40 m spatial resolution were conducted for the Rocky Mountain NP ISA. For a grid of 400 × 400 m blocks, we mapped the absolute difference between block snow cover fraction derived from 40 m binary SCA and block snow cover fraction derived from the original 0.5 m binary SCA image. Although the majority of 400 m blocks indicated absolute differences between binary and fractional SCA < 0.10, a number of blocks with absolute differences between binary and fractional SCA > 0.15 were identified at the Rocky Mountain National Park ISA (Figure 12). Snow cover within each of these blocks exhibited very fine scale variability in the original 0.5 m snow cover image.

3.4. Prevalence of Partially Snow-Covered Conditions at In Situ Monitoring Sites

In contrast to the results of the imagery analysis, which allowed us to calculate the prevalence of partially snow-covered pixels over a range of scales for many pixels on just a few dates, the *in situ* snow cover fraction measurements allowed us to calculate the prevalence of partial snow cover conditions at ten 60 m pixel footprints over all days for a 10-month period. Summary fractional SCA statistics computed from temperature data loggers are presented in Table 5. As mentioned previously, in a few cases, we were unable to locate a buried temperature data logger, and in a few other cases, data loggers malfunctioned or stopped recording due to insufficient battery voltage. The total number of temperature data loggers used for calculation of snow cover fraction varied between 12 and 16, with valid data available from at least 14 sensors for eight of the 10 sites (Table 5).

Daily time series of snow cover fraction for five of the six grid cells monitored at the Cinnamon Pass FSA and three of the four grid cells monitored at Niwot Ridge FSA are shown in Figure 13. Daily grid cell snow cover fraction calculated from temperature data logger arrays indicate that snow cover conditions at grid cell footprints fell into two distinct categories. At four of the 10 sites, full snow cover across the grid cell footprint occurred only rarely (3–45 days), despite snow covering a portion of the footprint for as many as 243 days during the monitoring period. At the remaining six sites, the grid cell footprint was fully snow covered between February 1 and late spring or early summer, with partial snow cover conditions common for some footprints during the earlier part of the season. For the six footprints with continuous or near continuous full winter snow cover, the first day with less than full snow cover after 1 April occurred between 3 May and 5 July. The length of the transition period between fully snow-covered and fully snow-free conditions ranged from 17–56 days, while the mean transition period length was 37 days.

Table 5. Full, partial, and total snow cover days, as well as snow-covered to snow-free transition period metrics for 60 × 60 m footprints. Transition period metrics were not calculated for sites with intermittent winter snow cover. CP indicates Cinnamon Pass, while NR indicates Niwot Ridge. fSCA indicates fractional snow-covered area.

Site	Study Area	Valid Sensors	Snow Cover Days			Partial/Total Ratio	First Day			
			Full	Partial	Total		< 1.0 fSCA	< 0.5 fSCA	Snow-Free	Length (days)
1	CP	14	17	223	240	0.93	-	-	-	-
2	CP	16	16	243	259	0.94	-	-	-	-

Table 5. *Cont.*

Site	Study Area	Valid Sensors	Snow Cover Days			Partial/Total Ratio	First Day			
			Full	Partial	Total		< 1.0 fSCA	< 0.5 fSCA	Snow-Free	Length (days)
3	CP	15	144	99	243	0.41	3 May	21 May	15 June	43
4	CP	16	235	25	260	0.10	9 June	23 June	2 July	23
5	CP	16	229	39	268	0.15	1 June	16 June	10 July	39
6	CP	16	242	61	303	0.20	18June	7 July	13 Aug.	56
7	NR	15	45	223	268	0.83	-	-	-	-
8	NR	12	3	183	186	0.98	-	-	-	-
9	NR	15	186	88	274	0.32	5 July	17 July	22 July	17
10	NR	13	162	137	299	0.46	29 June	15 July	13Aug.	45

Figure 13. Daily 60 m grid cell snow cover fraction time series from (**a**) grid cells 1, 5, and 6 at Cinnamon Pass FSA (**b**), grid cells 3 and 4 at Cinnamon Pass FSA, and (**c**) grid cells 8, 9, and 10 at Niwot Ridge FSA. Time series depicted in the same panel are all from grid cells within 500 m and could thus be contained within a single 500 m MODIS grid cell. Time series from the two 60 m grid cells not shown are similar to #1 (south facing) in panel (a) and #8 (ridgetop) in panel (c).

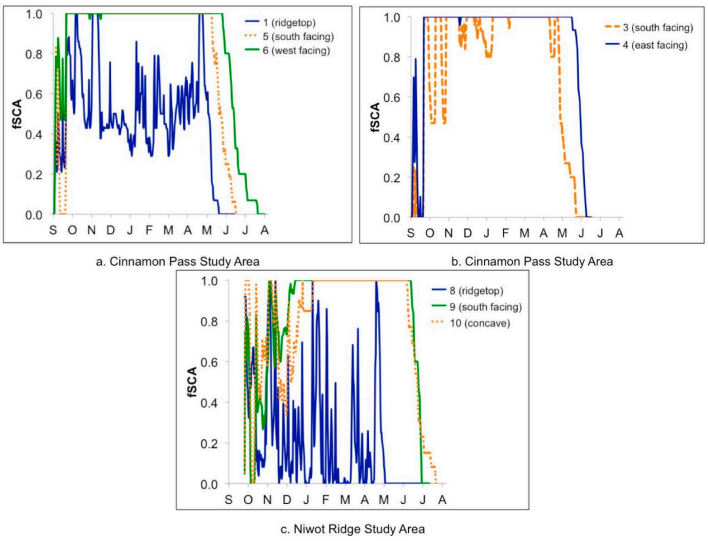

3.5. Sensitivity of Calculated Snow Cover Fraction to 24-Hour Temperature Range Threshold

Results from the sensitivity analysis of the effect of 24-hour temperature range threshold on calculated snow cover fraction at each footprint indicate that, at sites where partially snow-covered conditions were common throughout the winter, calculated snow cover fraction was highly sensitive to the temperature threshold value used in the algorithm (Figure 14a, Table 6). At sites where fully snow-covered conditions

persisted throughout the winter, calculated snow cover fraction was much less affected by varying the temperature threshold (Figure 14b, Table 6). The mean grid cell snow cover fraction uncertainty (in terms of snow cover fraction, ranging from 0–1) for all days between 15 October and the last day with snow cover ranged from 0.01 to 0.39 (Table 6), with an overall mean of 0.16 for all sites and all days. When only the period between 1 April and the last day of snow cover was considered, mean uncertainty was lower at all sites, ranging from 0 to 0.24, with an overall mean of 0.08. For the 15 October—snow-free period, the fraction of days with uncertainty in snow cover fraction > 0.1 ranged from < 0.01–0.86, while for the 1 April—snow-free period, the fraction of days with uncertainty in snow cover fraction > 0.1 ranged from 0–0.67. During the 1 April—snow-free period, the fraction of days with > 0.1 uncertainty at five of the 10 sites was ≤ 0.03.

Figure 14. Results from sensitivity analysis indicating 60 m grid cell snow cover fraction using 0.5 °C, 1 °C, 2 °C, and 3 °C temperature thresholds for (**a**) an example site with partially snow-covered conditions throughout the winter and spring (site #2) and (**b**) for an example site with consistent fully snow-covered conditions throughout the winter and spring (site #9).

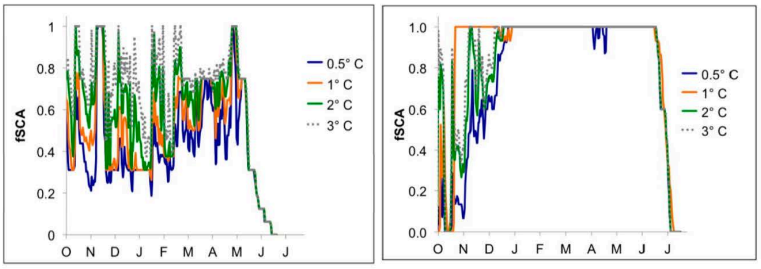

Table 6. Snow cover fraction uncertainty metrics for each 60 m grid cell. Uncertainty is expressed in terms of snow cover fraction ranging from 0 to 1.

Site	Valid Sensors	Partial/Total Snow Cover Days Ratio	15 October—Snow-Free Date			1 April—Snow-Free Date		
			Total Days	Mean Uncertainty	Fraction of Days with Uncertainty > 0.10	Total Days	Mean Uncertainty	Fraction of Days with Uncertainty > 0.10
1	14	0.93	240	0.29	0.86	72	0.22	0.67
2	16	0.94	258	0.26	0.76	91	0.13	0.45
3	15	0.41	241	0.11	0.35	75	0.02	0.00
4	16	0.10	257	0.01	0.00	92	0.00	0.00
5	16	0.15	264	0.04	0.12	100	0.03	0.13
6	16	0.20	297	0.03	0.13	135	0.02	0.00
7	15	0.83	262	0.39	0.81	100	0.16	0.49
8	12	0.98	216	0.29	0.81	55	0.24	0.69
9	15	0.32	272	0.09	0.26	112	0.01	0.03
10	13	0.46	293	0.12	0.29	134	0.01	0.01
Mean:	-	-	-	0.16	0.44		0.08	0.25

4. Discussion

Our analysis of mixed pixel prevalence across spatial resolutions indicates that mixed pixels occur frequently across the alpine landscape even at fine spatial resolutions (< 10 m), and that they often dominate the landscape at the spatial resolution imaged by Landsat (nominally 30, with true GIFOV closer to 40 m). For our analysis, we defined mixed pixels as pixels with fSCA between 0.02 and 0.98. While these thresholds may seem quite lax for identification of mixed pixels (or conversely, quite strict for identification of pure pixels), our goal was to estimate the fraction of the alpine landscape at different places, times, and spatial resolutions where sub-pixel variability in snow-covered area was present. The thresholds of 0.02 and 0.98 were chosen in lieu of 0 and 1 to account for occasional noise in the data. Our definition of mixed pixels will likely result in identification of more mixed pixels than would be mapped using Landsat and MODIS, since fSCA mapping algorithms such as MODSCAG often have difficulty mapping snow cover at fractions < approximately 0.15, while Landsat-based algorithms will be prone to overestimation of snow cover when saturation of the visible bands occurs, resulting in fewer mixed pixels when snow cover fractions are slightly below 1. Nevertheless, we believe it is important to quantify the prevalence of all mixed snow cover pixels, including those where the fraction of snow-covered or snow-free ground is quite small. Even very small differences in pixel fSCA, such as the difference between fSCA fractions of 1.0 and 0.97 can potentially indicate substantial differences in snow cover conditions, such as the difference between end of winter conditions with deep snow cover and conditions later in the spring where snow water equivalent has been reduced by 50% but only a tiny fraction of the pixel has melted out.

We found that mixed pixels were more common across all spatial scales and dates at our continental ISA in Colorado than at our maritime ISA in Oregon. It is possible that the more rugged topography at the Rocky Mountain NP ISA may be partially responsible for this difference. The increased prevalence of mixed pixels across all dates can still be observed, however, even when subsets with similar topographic characteristics are compared, at least for spatial resolutions < 125 m.

Differences between recent snowfall histories at the two ISAs prior to image acquisition are also insufficient to explain the greater prevalence of mixed pixels at the Rocky Mountain NP ISA, although heavy snow accumulation prior to the date of image acquisition did appear to reduce the incidence of mixed pixels in the Rocky Mountain NP ISA relative to other dates without recent heavy snow accumulation at the same ISA. At the Rocky Mountain NP ISA, the prevalence of mixed pixels was much lower for the three dates with ≥ 16 mm snow water equivalent accumulation over the previous 10 days (26 February 2014, 20 March 2010, and 7 May 2011) than for the two dates with little or no new snow over the previous 10 days (26 May 2012 and 29 September 2013) (Figure 9b). Heavy snow accumulation did not appear to have as pronounced an effect on the prevalence of mixed pixels in the Oregon Cascades ISA (Figure 9).

If differences in recent snow accumulation were the primary factor responsible for differences in the prevalence of mixed pixels between the two ISAs, we would expect to find a higher incidence of mixed pixels at the Oregon Cascades ISA than at the Rocky Mountain NP ISA, since no snowfall occurred within 10 days for three of the five dates analyzed at the Oregon Cascades ISA. Instead, we found the incidence of mixed pixels at the Oregon Cascades ISA was actually consistently lower than the incidence of mixed pixels at the Rocky Mountain NP ISA. We hypothesize that, over the course of the winter, the

combined effects of lower moisture content during snow accumulation events, lower overall precipitation, and higher wind speeds (Table 1) resulted in the development of a more heterogeneous snow cover at the continental Rocky Mountain NP ISA than at the Oregon Cascades ISA. Snowfall events with high moisture content (a common occurrence in the maritime snow climate of the Oregon Cascades) are more likely to coat all terrain surfaces evenly during accumulation. In contrast, snowfall events with lower moisture content (a common occurrence in the Colorado Rockies) often result in less uniform accumulation, a situation that is exacerbated by consistently higher wind speeds.

Finally, it is also possible that differences in very fine scale surface roughness that cannot be captured by a 10-m DEM may also play a role in explaining the differences between the prevalence of mixed pixels at these two study areas.

It is worth noting that a significant but unknown fraction of the snow cover mapped in the 1 September 2013 image from the Oregon Cascades ISA consisted of exposed glacial ice as well as snow cover from the current year on top of glacial ice, particularly within the high-relief subset image (Figure 2). While the presence of glacier cover raises the overall ISA snow cover fraction, it is also likely to reduce the prevalence of mixed pixels at the spatial resolutions considered here, since glaciers represent a large mass of contiguous ice and snow that might otherwise be occupied by a patchy distribution of late-lying seasonal snow cover patches.

The observation that portions of the alpine landscape remain free of snow cover across much of the winter and spring while other areas remain snow covered well into the summer is not novel. The daily 60 m snow cover fraction time series computed from 1.5-hourly temperature data collected near the ground surface, however, allowed us to quantify the frequency of partially snow-covered conditions at a scale similar to that provided by Landsat. While the calculated snow cover fraction for pixel footprints with intermittent snow cover appeared to be quite sensitive to the 24-hour temperature range threshold used to classify the presence or absence of snow cover above each sensor, the results from the uncertainty analysis still indicated that, regardless of the temperature range threshold value used, partial snow cover conditions occurred with great frequency throughout the winter and spring. For the remaining sites, where snow covered the entire pixel footprint for most or all days prior to the spring snowmelt period, the temperature range threshold value appeared to matter very little, suggesting that snow cover fraction estimates for these footprints can be considered more reliable.

At the four sites where partially snow-covered conditions were common throughout the winter and spring, monitoring per-pixel snow cover fraction provides a clear advantage over binary monitoring approaches that use an arbitrary, potentially variable fractional snow cover threshold to classify a pixel as snow-covered or snow-free. At this type of site, binary snow cover classifications will consistently overestimate the true snow cover fraction for most instances when snow covers $> 50\%$ of the pixel footprint and consistently underestimate the true snow cover fraction for most instances when snow covers $< 50\%$ of the land surface, although aggregation of results from many pixels can reduce the magnitude of the error. While at first glance, the need for a fractional monitoring approach may seem less obvious for sites where fully snow-covered conditions occur throughout the winter, the spring transition period between fully snow-covered and fully snow-free conditions at these sites spanned a period when 2–4 scenes would be collected by a single Landsat instrument (with the potential for even more scenes during periods of concurrent Landsat missions and in areas covered by more than one orbital path). During this transition period, there is an obvious benefit to retrieving per-pixel snow cover

fraction, rather than simply the presence or absence of snow cover, as per-pixel fractional snow-covered area can provide detailed information on the progression of snowmelt at the pixel rather than just a vague approximation of the time when the pixel transitioned from > 50% snow cover to < 50% snow cover.

The rarity of pure pixels at 500 m spatial resolution and the sometimes dramatic differences in snow cover conditions that often exist in close proximity within 500 m grid cells (as demonstrated in Figure 13) present a strong case for the necessity of adopting a fractional SCA mapping approach when working with MODIS data in high mountain areas. It is important to note that for an instrument such as MODIS, the actual ground instantaneous field of view (GIFOV) represented by a single pixel is always larger than the nominal spatial resolution of 500 m, as only approximately 75% of the signal originates from within the nominal 500 m field of view [59]. In addition, for pixels imaged near the edge of the scan, where the scan angle can be as high as 55°, the GIFOV represented in a single pixel is approximately 10× as large as at nadir [60]. While this study does not directly address the frequency of mixed pixels for ground instantaneous fields of view larger than 500 × 500 m, for resolutions between 1 m and 500 m, the probability of mixed pixels generally continues to increase with increasing pixel size, and thus it seems likely that mixed pixels would occur even more frequently for cases where the GIFOV is substantially larger, as it is for MODIS pixels not located near the center of the scan. Ultimately, the vast diversity of conditions within a single MODIS pixel footprint, even at the nominal 500 m spatial resolution, emphasizes the utility of finer scale remote sensing using Landsat or a similar finer resolution platform.

The lower incidence of mixed pixels at the Landsat spatial resolution suggests that a binary SCA mapping approach may be acceptable for some applications in mountain regions at the Landsat scale. For example, in a larger basin with a diversity of slopes and aspects, binary SCA overestimation of snow cover on north-facing slopes with 75% snow cover may often be offset by underestimation of snow cover on south-facing slopes with 25% snow cover, resulting in a basin-wide SCA estimate that closely approximates the true SCA for the basin. However, for basins with more homogeneous terrain at scales > 30 m, monitoring of individual slopes, and any applications where highly accurate spatial distributions are essential, the additional information provided by a fractional SCA dataset provides a major advantage.

For many applications, the most important measure of snowpack is the snow water equivalent (SWE) or snow depth. While optical remote sensing cannot be used directly for monitoring either SWE or snow depth, there is a strong link between SWE and SCA [61], and SCA retrievals from optical sensors can be used in a variety of ways to assist with the estimation of snow depth or SWE. These include the provision of melt-out dates used for SWE reconstruction [1–3], constraining modeled SWE to areas where snow cover is actually present [4], and providing the spatial distribution of snow cover for validation of modeled snow cover evolution over space and time [62,63]. In all of these cases, there is a benefit to using fractional SCA at 30 m spatial resolution, particularly if the modeling occurs at 30 m spatial resolution or finer.

It is important to note that the above discussion assumes similar accuracy in retrievals of both binary and fractional SCA. Highly accurate binary SCA data will always remain more useful than fractional SCA data of poor quality. Likewise, highly accurate fractional SCA data will always be more useful than poorer quality binary SCA data.

5. Conclusions

While mixed snow-covered/snow-free pixels can occur at any spatial resolution, at both of our ISAs, mixed pixels become increasingly common at coarser spatial resolutions. The curves representing the fraction of mixed pixels versus spatial resolution varied substantially depending on total study area snow cover fraction, time of year, and snow climate regime. Mixed pixels were more prevalent at the colder, drier continental study area. At the Landsat spatial resolution, mixed pixels comprised 36% of the total pixels over all dates in the Oregon Cascades ISA and 69% of the total pixels for the Rocky Mountain NP ISA. At the MODIS spatial resolution, mixed pixels comprised 81% of the total pixels over all dates in the Oregon Cascades and 93% of the total pixels for the Rocky Mountain NP ISA.

Daily fractional SCA calculated from *in situ* temperature data loggers covering 60 m grid cell footprints at two high elevation sites in Colorado suggested sites could be divided into two distinct categories. Four of the 10 footprints could be characterized as intermittently snow-covered sites where full snow cover across the entire 60 m footprint occurred rarely (as few as three days at one site), despite continuous or near continuous partially snow-covered conditions throughout the winter and spring. The remaining six footprints could be characterized as sites that remained fully snow-covered for most or all days between late fall and late spring or summer. While these sites experienced fewer days overall with partially snow-covered conditions, a period of continuous or nearly continuous partially snow-covered conditions occurred at each site during the transition between fully snow-covered and fully snow-free conditions. The mean length of this transition period was 37 days, with length varying from as few as 17–56 days.

At the MODIS spatial resolution, the rarity of pure pixels make fractional SCA mapping the obvious choice for snow cover monitoring in mountainous environments. At the finer Landsat spatial resolution, binary SCA mapping may be acceptable for some applications, but fractional SCA mapping offers substantial advantages for a variety of applications, particularly in cases where the accurate representation of snow cover spatial distributions (rather than just total SCA integrated over larger areas) is important.

Acknowledgments

Funding for this research was provided by the Land Remote Sensing Program of the U.S. Geological Survey. The authors gratefully acknowledge assistance in the field provided by Melanie Cota and Barry Middleton.

Author Contributions

David J. Selkowitz has been the primary author of the manuscript, conceived the study design, and was involved in all aspects of the data collection and analysis. Richard R. Forster assisted with development of the study design and interpretation of the results. Megan K. Caldwell assisted with development of the study design, secured the permits for *in situ* monitoring at Niwot Ridge, conducted some of the field work, and provided an assessment of the accuracy of the high-resolution binary SCA images.

Conflicts of Interest

The authors declare no conflict of interest.

References

1. Cline, D.W.; Bales, R.C.; Dozier, J. Estimating the spatial distribution of snow in mountain basins using remote sensing and energy balance modeling. *Water Resour. Res.* **1998**, *34*, 1275–1285.
2. Durand, M.; Molotch, N.P.; Margulis, S.A. Merging complementary remote sensing datasets in the context of snow water equivalent reconstruction. *Remote Sens. Environ.* **2008**, *112*, 1212–1225.
3. Molotch, N.P.; Margulis, S.A. Estimating the distribution of snow water equivalent using remotely sensed snow cover data and a spatially distributed snowmelt model: A multi-resolution, multi-sensor comparison. *Adv. Water Resour.* **2008**, *31*, 1503–1514.
4. Harshburger, B.J.; Humes, K.S.; Walden, V.P.; Blandford, T.R.; Moore, B.C.; Dezzani, R.J. Spatial interpolation of snow water equivalency using surface observations and remotely sensed images of snow-covered area. *Hydrol. Processes* **2010**, *24*, 1285–1295.
5. Andreadis, K.M.; Lettenmaier, D.P. Assimilating remotely sensed snow observations into a macroscale hydrology model. *Adv. Water Resour.* **2006**, *29*, 872–886.
6. Clark, M.P.; Slater, A.G.; Barrett, A.P.; Hay, L.E.; McCabe, G.J.; Rajagopalan, B.; Leavesley, G.H. Assimilation of snow covered area information into hydrologic and land-surface models. *Adv. Water Resour.* **2006**, *29*, 1209–1221.
7. Zhang, T. Influence of the seasonal snow cover on the ground thermal regime: An overview. *Rev. Geophys.* **2005**, *43*, doi:10.1029/2004RG000157.
8. Groffman, P.M.; Driscoll, C.T.; Fahey, T.J.; Hardy, J.P.; Fitzhugh, R.D.; Tierney, G.L. Colder soils in a warmer world: A snow manipulation study in a northern hardwood forest ecosystem. *Biogeochemistry* **2001**, *56*, 135–150.
9. Quinton, W.L.; Bemrose, R.K.; Zhang, Y.; Carey, S.K. The influence of spatial variability in snowmelt and active layer thaw on hillslope drainage for an alpine tundra hillslope. *Hydrol. Process.* **2009**, *23*, 2628–2639.
10. Billings, W.D.; Bliss, L.C. An alpine snowbank environment and its effects on vegetation, plant development, and productivity. *Ecology* **1959**, *40*, 388–397.
11. Walker, D.A.; Halfpenny, J.C.; Walker, M.D.; Wessman, C.A. Long-term studies of snow-vegetation interactions. *Bioscience* **1993**, *43*, 287–301.
12. Kudo, G. Effects of snow-free period on the phenology of alpine plants inhabiting snow patches. *Arct. Alp. Res.* **1991**, *23*, 436–443.
13. Eastland, W.G.; Bowyer, R.T.; Fancy, S.G. Effects of snow cover on selection of calving sites by caribou. *J. Mammal.* **1989**, *70*, 824–828.
14. Huggard, D.J. Effects of snow depth on predation and scavenging by gray wolves. *J. Wildlife Manage.* **1993**, *57*, 382–388.
15. Stenseth, N.C.; Shabbar, A.; Chan, K.S.; Boutin, S.; Rueness, E.K.; Ehrich, D.; Hurrell, J.W.; Lingjaerde, O.C.; Jakobsen, K.S. Snow conditions may create an invisible barrier for lynx. In Proceedings of the National Academy of Sciences of the United States of America, Princeton, NJ, USA, 7 June 2004; pp. 10632–10634.
16. Rango, A; Itten, K. Satellite potentials in snowcover monitoring and runoff prediction. *Nord. Hydrol.* **1976**, *7*, 209–230.

17. Dozier, J. Spectral signature of alpine snow cover from the Landsat Thematic Mapper. *Remote Sens. Environ.* **1989**, *28*, 9–22.
18. Hall, D.K.; Riggs, G.A.; Salomonson, V.V. Development of methods for mapping global snow cover using moderate resolution imaging spectroradiometer data. *Remote Sens. Environ.* **1995**, *54*, 127–140.
19. Klein, A.G.; Hall, D.K.; Riggs, G.A. Improving snow cover mapping in forests through the use of a canopy reflectance model. *Hydrol. Processes* **1998**, *12*, 1723–1744.
20. Hall, D. K.; Riggs, G. A.; Salomonson, V. V.; DiGirolamo, N. E.; Bayr, K. J. MODIS snow-cover products. *Remote Sens. Environ.* **2002**, *83*, 181–194.
21. Crawford, C.J.; Manson, S.M.; Bauer, M.E.; Hall, D.K. Multitemporal snow cover mapping in mountainous terrain for Landsat climate data record development. *Remote Sens. Environ.* **2013**, *135*, 224–233
22. Rosenthal, W.; Dozier, J. Automated mapping of montane snow cover at subpixel resolution from the Landsat Thematic Mapper. *Water Resour. Res.* **1996**, *32*, 115–130.
23. Painter, T.H.; Dozier, J.; Roberts, D.A.; Davis, R.E.; Green, R.O. Retrieval of subpixel snow-covered area and grain size from imaging spectrometer data. *Remote Sens. Environ.* **2003**, *85*, 64–77.
24. Vikhamar, D.; Solberg, R. Snow-cover mapping in forests by constrained linear spectral unmixing of MODIS data. *Remote Sens. Environ.* **2003**, *88*, 309–323.
25. Salomonson, V.V.; Appel, I. Estimating fractional snow cover from MODIS using the normalized difference snow index. *Remote Sens. Environ.* **2004**, *89*, 351–360.
26. Painter, T.H.; Rittger, K.; McKenzie, C.; Slaughter, P.; Davis, R.E.; Dozier, J. Retrieval of subpixel snow covered area, grain size, and albedo from MODIS. *Remote Sens. Environ.* **2009**. *113*, 868–879.
27. Rittger, K.; Painter, T. H.; Dozier, J. Assessment of methods for mapping snow cover from MODIS. *Adv. Water Resour.* **2013**, *51*, 367–380.
28. Woodcock, C.E.; Strahler, A.H. The factor of scale in remote sensing. *Remote Sens. Environ.* **1987**, *21*, 311–332.
29. Moody, A.; Woodcock, C.E. The influence of scale and the spatial characteristics of landscapes on land-cover mapping using remote sensing. *Landscape Ecol.* **1995**, *10*, 363–379.
30. Cracknell, A.P. Review article Synergy in remote sensing—What's in a pixel? *Int. J. Remote Sens.* **1998**, *19*, 2025–2047.
31. Marceau, D.J.; Howarth, P.J.; Gratton, D.J. Remote sensing and the measurement of geographical entities in a forested environment. 1. The scale and spatial aggregation problem. *Remote Sens. Environ.* **1994**, *49*, 93–104.
32. Chen, J.M. Spatial scaling of a remotely sensed surface parameter by contexture. *Remote Sens. Environ.* **1999**, *69*, 30–42.
33. Pax-Lenney, M.; Woodcock, C.E. The effect of spatial resolution on the ability to monitor the status of agricultural lands. *Remote Sens. Environ.* **1997**, *61*, 210–220.
34. Kustas, W.P.; Li, F.; Jackson, T.J.; Prueger, J.H.; MacPherson, J.I.; Wolde, M. Effects of remote sensing pixel resolution on modeled energy flux variability of croplands in Iowa. *Remote Sens. Environ.* **2004**, *92*, 535–547.
35. Smith, M.O.; Ustin, S.L.; Adams, J.B.; Gillespie, A.R. Vegetation in deserts: I. A regional measure of abundance from multispectral images. *Remote Sens. Environ.* **1990**, *31*, 1–26.

36. DeFries, R.S.; Field, C.B.; Fung, I.; Justice, C.O.; Los, S.; Matson, P.A.; Vitousek, P.M. Mapping the land surface for global atmosphere-biosphere models: Toward continuous distributions of vegetation's functional properties. *J. Geophys. Res. Atmos.* **1995**, *100*, 20867–20882.
37. Hansen, M.C.; DeFries, R.S.; Townshend, J.R.G.; Carroll, M.; Dimiceli, C.; Sohlberg, R.A. Global percent tree cover at a spatial resolution of 500 meters: First results of the MODIS vegetation continuous fields algorithm. *Earth Interact.* **2003**, *7*, 1–15.
38. Wu, C.; Murray, A.T. Estimating impervious surface distribution by spectral mixture analysis. *Remote Sens. Environ.* **2003**, *84*, 493–505.
39. Fily, M.; Royer, A.; Goıta, K.; Prigent, C.A. Simple retrieval method for land surface temperature and fraction of water surface determination from satellite microwave brightness temperatures in sub-arctic areas. *Remote Sens. Environ.* **2003**, *85*, 328–338.
40. Cline, D.; Elder, K.; Bales, R. Scale effects in a distributed snow water equivalence and snowmelt model for mountain basins. *Hydrol. Process.* **1998**, *12*, 1527–1536
41. Bloschl, G. Scaling issues in snow hydrology. *Hydrol. Processes* **1999**, *13*, 2149–2175.
42. Deems, J.S.; Fassnacht, S.R.; Elder, K.J. Fractal distribution of snow depth from LiDAR data. *J. Hydrometeorol.* **2006**, *7*, 285–297.
43. Fassnacht, S.R.; Deems, J.S. Measurement sampling and scaling for deep montane snow depth data. *Hydrol. Processes* **2006**, *20*, 829–838.
44. Trujillo, E.; Ramírez, J.A.; Elder, K.J. Scaling properties and spatial organization of snow depth fields in sub-alpine forest and alpine tundra. *Hydrol. Process.* **2009**, *23*, 1575–1590.
45. Mott, R.; Schirmer, M.; Lehning, M. Scaling properties of wind and snow depth distribution in an Alpine catchment. *J. Geophys. Res. Atmos.* **2011**, *116*, doi:10.1029/2010JD014886.
46. PRISM Climate Group. PRISM Climate Data. Available online: http://prism.oregonstate.edu (accessed on 15 April 2014).
47. Raws USA Climate Archive. Available online: http://raws.dri.edu (accessed on 1 November 2013).
48. Saddle (3525 m) Climate Station: CR23X Data. Available online: http://culter.colorado.edu/ (accessed on 1 November 2014).
49. Landry, C.C.; Buck, K.A.; Raleigh, M.S.; Clark, M.P. Mountain system monitoring at Senator Beck Basin, San Juan Mountains, Colorado: A new integrative data source to develop and evaluate models of snow and hydrologic processes. *Water Resour. Res.* **2014**, *50*, doi:10.1002/2013WR013711.
50. Gesch, D.; Oimoen, M.; Greenlee, S.; Nelson, C.; Steuck, M.; Tyler. D. The national elevation dataset. *Photogramm. Eng. Remote Sens.* **2002**, *68*, 5–32.
51. Mauck, J.; Brown, K.; Carswell, W.J., Jr. The National Map—Orthoimagery. Available online: http://pubs.usgs.gov/fs/2009/3055/pdf/FS2009-3055.pdf (accessed on 2 October 2014).
52. Ball, G.H.; Hall, D.J. *Isodata, A Novel Method of Data Analysis and Pattern Classification*; Stanford Research Institute: Menlo Park, CA, USA, 1965.
53. Markham, B.L. The Landsat sensors' spatial responses. *IEEE Trans. Geosci. Remote Sens.* **1985**, *6*, 864–875.
54. Raleigh, M.S.; Rittger, K.; Moore, C.E.; Henn, B.; Lutz, J.A.; Lundquist, J.D. Ground-based testing of MODIS fractional snow cover in subalpine meadows and forests of the Sierra Nevada. *Remote Sens. Environ.* **2013**, *128*, 44–57.

55. Danby, R.K.; HIK, D.S. Responses of white spruce (Picea glauca) to experimental warming at a subarctic alpine treeline. *Glob. Change Biol.* **2007**, *13*, 437–451.
56. Lundquist, J.D.; Lott, F. Using inexpensive temperature sensors to monitor the duration and heterogeneity of snow-covered areas. *Water Resour. Res.* **2008**, *44*, doi:10.1029/2008WR007035.
57. Schmid, M.O.; Gubler, S.; Fiddes, J.; Gruber, S. Inferring snowpack ripening and melt-out from distributed measurements of near-surface ground temperatures. *Cryosphere* **2012**, *6*, 1127–1139.
58. Selkowitz, D.; Forster, R., Caldwell, M. US Geological Survey, Alaska Science Center. Unpublished work, 2014.
59. Wolfe, R.E.; Roy, D.P.; Vermote, E. MODIS land data storage, gridding, and compositing methodology: Level 2 grid. *IEEE Trans. Geosci. Remote Sens.* **1998**, *36*, 1324–1338.
60. Tan, B.; Woodcock, C.E.; Hu, J.; Zhang, P.; Ozdogan, M.; Huang, D.; Yang, W.; Knyazikhin, Y.; Myneni, R.B. The impact of gridding artifacts on the local spatial properties of MODIS data: Implications for validation, compositing, and band-to-band registration across resolutions. *Remote Sens. Environ.* **2006**, *105*, 98–114.
61. Liston, G.E. Interrelationships among snow distribution, snowmelt, and snow cover depletion: Implications for atmospheric, hydrologic, and ecologic modeling. *J. Appl. Meteorol.* **1999**, *38*, 1474–1487.
62. Letsinger, S.L.; Olyphant, G.A. Distributed energy-balance modeling of snow-cover evolution and melt in rugged terrain: Tobacco Root Mountains, Montana, USA. *J. Hydrol.* **2007**, *336*, 48–60.
63. Bernhardt, M.; Liston, G.E.; Strasser, U.; Zangl, G.; Schulz, K. High resolution modeling of snow transport in complex terrain using downscaled MM5 wind fields. *Cryosphere* **2010**, *4*, 99–113.

CHAPTER 3

AN AUTOMATED APPROACH FOR MAPPING PERSISTENT ICE AND SNOW COVER OVER HIGH LATITUDE REGIONS

Selkowitz, D. J., & Forster, R. R. (2015). An automated approach for mapping persistent ice and snow cover over high latitude regions. *Remote Sensing*, *8*(1), 16. Published by MDPI 2015. This work was produced as part of the lead author's fulfillment of official government duties and is therefore considered to be in the public domain and not subject to copyright protection.

remote sensing

MDPI

Article

An Automated Approach for Mapping Persistent Ice and Snow Cover over High Latitude Regions

David J. Selkowitz [1,2,*] and Richard R. Forster [2]

Received: 30 June 2015; Accepted: 21 December 2015; Published: 25 December 2015
Academic Editors: Daniel J. Hayes, Santonu Goswami, Guido Grosse, Benjamin Jones, Richard Gloaguen and Prasad S. Thenkabail

[1] U.S. Geological Survey, Alaska Science Center, 4210 University Drive, Anchorage, AK 99508, USA
[2] Department of Geography, University of Utah, 260 S. Central Campus Dr., Room 270, Salt Lake City, UT 84112, USA; rick.forster@geog.utah.edu
* Correspondence: dselkowitz@usgs.gov; Tel.: +1-907-786-7146; Fax: +1-907-786-7020

Abstract: We developed an automated approach for mapping persistent ice and snow cover (glaciers and perennial snowfields) from Landsat TM and ETM+ data across a variety of topography, glacier types, and climatic conditions at high latitudes (above ~65°N). Our approach exploits all available Landsat scenes acquired during the late summer (1 August–15 September) over a multi-year period and employs an automated cloud masking algorithm optimized for snow and ice covered mountainous environments. Pixels from individual Landsat scenes were classified as snow/ice covered or snow/ice free based on the Normalized Difference Snow Index (NDSI), and pixels consistently identified as snow/ice covered over a five-year period were classified as persistent ice and snow cover. The same NDSI and ratio of snow/ice-covered days to total days thresholds applied consistently across eight study regions resulted in persistent ice and snow cover maps that agreed closely in most areas with glacier area mapped for the Randolph Glacier Inventory (RGI), with a mean accuracy (agreement with the RGI) of 0.96, a mean precision (user's accuracy of the snow/ice cover class) of 0.92, a mean recall (producer's accuracy of the snow/ice cover class) of 0.86, and a mean F-score (a measure that considers both precision and recall) of 0.88. We also compared results from our approach to glacier area mapped from high spatial resolution imagery at four study regions and found similar results. Accuracy was lowest in regions with substantial areas of debris-covered glacier ice, suggesting that manual editing would still be required in these regions to achieve reasonable results. The similarity of our results to those from the RGI as well as glacier area mapped from high spatial resolution imagery suggests it should be possible to apply this approach across large regions to produce updated 30-m resolution maps of persistent ice and snow cover. In the short term, automated PISC maps can be used to rapidly identify areas where substantial changes in glacier area have occurred since the most recent conventional glacier inventories, highlighting areas where updated inventories are most urgently needed. From a longer term perspective, the automated production of PISC maps represents an important step toward fully automated glacier extent monitoring using Landsat or similar sensors.

Keywords: remote sensing of glaciers; snow and ice; Landsat; arctic

1. Introduction

Glaciers have been identified as one of the most sensitive indicators of changes in climate [1,2] and have been identified as an essential climate variable that should be monitored globally [3]. Glaciers not only respond to changes in climate, but can also drive changes in the earth climate system through changes in albedo and contribution to sea level rise [4–7]. From a more local to regional

perspective, glaciers often serve as a crucial source of runoff for downstream populations [8] and can present a potential hazard due to glacier lake outburst floods [9,10].

While the presence of exposed ice at the end of the melt season allows most glaciers to be positively identified under the right conditions, smaller glaciers cannot always be reliably distinguished from perennial snow cover patches. The challenge of discriminating between perennial snow cover patches and glaciers is confounded by the lack of satellite imagery acquired under ideal conditions when the maximum amount of ice is exposed. Consequently, even high quality glacier inventories created by image analysts may include some large perennial snow cover patches or omit some small glaciers. Image analysts are able to use contextual information (such as topographic position, patch shape, or ice or snow texture) to assist in discriminating between perennial snow cover patches and glaciers. Here we present a relatively simple automated approach designed to map glaciers that is likely to include a larger amount of perennial and consistently late lying seasonal snow cover patches than would be included in more traditional approaches. Therefore, although our intent is ultimately to map glaciers, we refer to the automated maps produced by the approach we describe as persistent ice and snow cover (PISC) maps, acknowledging that some perennial snow cover and late lying seasonal snow cover may be included.

Despite the important role of glaciers in the global earth system, *in situ* monitoring efforts are limited to a tiny fraction of the areas containing glaciers [11]. While field measurements of mass balance are irreplaceable indicators of the status of specific glaciers, spaceborne remote sensing can provide crucial complementary information such as the areal extent of ice cover over large regions encompassing numerous glaciers. For this reason, remote sensing approaches have been implemented as a key component of the tiered global glacier monitoring strategy for the Global Terrestrial Network for Glaciers (GTN-G) [12]. Optical remote sensing using the visible through middle infrared bands has been the method of choice for the majority of remote sensing efforts attempting to map glaciers. This is due to both the widespread availability of optical remote sensing data from sensors such as those from the Landsat series and the Advanced Spaceborne Thermal Emission and Reflection Radiometer (ASTER) as well as the relatively unique spectral signature of snow and ice cover in the optical remote sensing wavelengths.

Landsat image data have been used for a wide variety of glacier monitoring applications for more than 30 years. Early work with Landsat MultiSpectral Scanner (MSS) and Landsat Thematic Mapper (TM) focused on identification of glacier zones and calculation of corresponding reflectance values [13–18]. This was soon followed by glacier area mapping as well as change detection for areas covered by a single Landsat path-row [19–21]. Since the launch of the Landsat Enhanced Thematic Mapper Plus (ETM+) in 1999, numerous studies have used either the TM or ETM+ sensors (or in some cases, both sensors) to create glacier maps for increasingly large areas [22–26], with data from many of these studies included in the Global Land Ice Measurements from Space (GLIMS) database [27,28]. Even more recently, the Randolph Glacier Inventory (RGI) was compiled to be the first comprehensive glacier database with global coverage [29].

Despite the potential offered by remote sensing, comprehensive, fully inclusive glacier monitoring at spatial resolutions fine enough to detect changes in glacier area that typically occur over a decade or less has remained elusive in some regions. While global monitoring efforts such as GLIMS and more recently the RGI have been effective for mapping glaciers across many large regions, global coverage has only been achieved very recently and the glacier inventory dates within the global database span several decades. In addition, for many regions, mapping of changes in glacier area over time has not been conducted.

One reason why such large area inventories have not been completed more regularly or for more regions is because existing approaches have required a substantial time investment by skilled image analysts. While previous work has demonstrated that automated classification results are typically as good or better than manually digitized results [30], even automated mapping approaches still require investment of an analyst's time in the pre-processing stage (selection and acquisition of appropriate

scenes with minimal cloud cover and minimal seasonal snow cover) as well as the post-processing stage (manual editing to correct classification errors, add areas of debris-covered glacier ice, and remove areas of perennial and seasonal snow cover, sea ice and icebergs) [31]. In many cases, input from an image analyst is also necessary to determine appropriate thresholds for band ratios or individual bands during the main processing stage. Manual correction of automatically-derived drainage divides from digital elevation models can also be a time consuming part of the process in some cases.

We demonstrate that, across the circumpolar Arctic, and perhaps globally, the extent of PISC can be regularly monitored using fully automated processing of Landsat data that exploits all available cloud-free, shadow-free data available from the late summer period. This approach represents an important step toward fully automated monitoring of glacier extent across large regions. In addition, PISC maps generated by this approach can also be used to rapidly identify areas where substantial changes may have occurred since the most recent conventional glacier inventories were conducted and thus highlight areas where updated glacier inventories are most urgently needed. Finally, many applications can potentially benefit from regularly updated PISC maps, including land surface models, runoff models, and general circulation models (GCMs).

2. Study Regions

We developed and tested the automated PISC mapping approach using data from four regions distributed throughout the Arctic, which we refer to as RGI calibration study areas (Figure 1, Table 1). Each RGI calibration study area covered a 35 × 35 km area, with glaciers covering as much as 66% of the study domain at Bylot Island, Canada and as little as 11% of the study domain in the Brooks Range in the United States (as indicated by the RGI dataset). We tested the PISC mapping algorithm at four additional 35 × 35 km study areas, referred to as RGI validation study areas, as well as at four smaller (approximately 15 × 15 km) study areas where we acquired very high resolution imagery (VHRI) (Figure 1, Table 1), referred to as VHRI validation study areas. The selection of 35 × 35 km bounding regions for the RGI calibration and RGI validation study areas was constrained to areas within the RGI database above 65°N with >5% ice cover where the dates of imagery used to construct the RGI glacier inventory were known to be within a single year. Allowing for these constraints, we selected 35 × 35 km study areas to represent a range of glacier types, topography, and climatic conditions. The selection of VHRI validation study areas was constrained to areas above 65°N with >5% ice cover where acceptable very high resolution imagery from the period 2010–2015 was available from the DigitalGlobe archive of data from the WorldView 2 or WorldView 3 satellites (mention of a particular product does not constitute endorsement by the U.S. federal government). To be considered acceptable for our purposes, very high resolution imagery needed to contain a contiguous area of ~15 × 15 km or larger with >5% ice cover that was cloud-free and nearly or completely free of late lying seasonal snow cover from the previous winter as well as nearly or completely free of recently accumulated snowfall. Allowing for these constraints, as with the selection of RGI calibration and RGI validation study areas, we selected study areas intended to represent a range of glacier types, topography, and climate conditions. Two of the four VHRI validation study areas were 15 × 15 km in size, while the others were 16 × 14 km and 17.5 × 12.9 km due to cloud cover.

Table 1. Study area locations and characteristics.

Study Area	Country	Type	VHRI Sensor	Lat	Lon	Ice Cover	WRS-2 Path/Row
Brooks Range 1	USA	RGI calibration	n/a	69.3°N	144.0°W	11%	68/11, 69/12, 70/11, 71/11, 72/11
Saltfjellet	Norway	RGI calibration	n/a	66.7°N	14.2°E	26%	197/13, 198/13, 199/13, 200/13
Bylot Island	Canada	RGI calibration	n/a	73.4°N	79.0°W	66%	30/8, 31/8, 32/8, 33/8, 34/8, 35/8
Jamesonland	Greenland	RGI calibration	n/a	71.8°N	25.0°W	61%	226/9, 226/10, 227/9, 228/9, 229/9, 230/9, 231/9
Clavering Island	Greenland	RGI validation	n/a	74.3°N	21.0°W	20%	227/8, 228/7, 228/8, 229/7, 230/7, 231/7
Barnes Ice Cap	Canada	RGI validation	n/a	69.6°N	72.0°W	47%	22/11, 23/11, 24/11, 25/11
Trollaskagi Peninsula	Iceland	RGI validation	n/a	65.7°N	18.8°W	8%	218/14, 219/14, 220/14
Sarek NP	Sweden	RGI validation	n/a	67.3°N	17.7°E	10%	196/13, 197/13, 198/13
Brooks Range 2	USA	VHRI validation	WorldView 2	69.2°N	144.8°W	6%	69/11, 70/11, 71/11, 72/11
Borden Peninsula	Canada	VHRI validation	WorldView 2	73.3°N	82.7°W	47%	33/8, 34/8, 35/8, 36/8
Pond Inlet	Canada	VHRI validation	WorldView 3	72.3°N	75.7°W	83%	27/9, 28/9, 29/9, 30/9
Sverny Island	Russia	VHRI validation	WorldView 2	74.3°N	55.7°E	34%	177/8, 178/7, 178/8, 179/7, 180/7

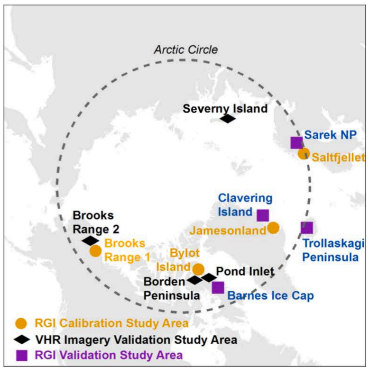

Figure 1. Study area locations across the circumpolar Arctic.

3. Data

3.1. Landsat Data

Most land areas on the surface of the Earth are imaged by each active Landsat sensor every 16 days, resulting in 22 or 23 potential scenes each year that cover a specific area of interest. For most regions outside of the conterminous United States, however, only a limited selection of scenes imaged by the Landsat TM and ETM+ instruments have been downloaded and archived [32], resulting in the availability of far less than 22–23 scenes per year for many areas [33]. Finally, persistent cloud cover is an additional factor that further reduces the number of useful surface views. A typical glacier monitoring or mapping effort involves identifying cloud-free images (or portions of images), or for larger regions, collection of images, acquired during the seasonal minimum snow cover extent period.

While in theory this is straightforward, the typically short duration of the snow-free period on and around glaciers does not always coincide with the availability of a cloud-free satellite acquisition. As a result, accurate glacier mapping requires careful scene selection by skilled analysts with knowledge of the region and the seasonal snow cover conditions during the period of interest. The analyst must select optimal scenes for automated or semi-automated glacier classification [30].

Overlapping Landsat paths result in more frequent image acquisitions for locations covered by more than 1 path. While only about 5% of the land surface is covered by multiple paths at the equator [34], at high latitudes, due to the convergence of Landsat paths, path overlap is ubiquitous, with many ground locations covered by three or more Landsat paths. This results in a doubling or even tripling of the number of Landsat scenes covering an area of interest. Assuming a substantial portion of these scenes have been acquired and archived (global scene availability is described in [33]), the odds of finding one or more scenes (or portions thereof) that capture the minimum annual extent of snow and ice under cloud-free conditions theoretically increases substantially with latitude. In our approach, we exploit this relative abundance of scenes available at many high latitude locations and consider all available Landsat TM or ETM+ data for each location, using an automated cloud classification algorithm to identify all instances of cloud-free views for each pixel location.

The majority of studies mapping glacier area using Landsat data have used uncorrected raw digital number (DN) or top-of-atmosphere (TOA) reflectance image data. Previous work has shown, however, that the use of atmospherically corrected surface reflectance image data can improve the accuracy of the results [35], and that atmospheric correction is particularly crucial if the Normalized Difference Snow Index (NDSI), which incorporates Landsat band 2 where atmospheric scattering is particularly high, is used [36]. To limit errors that could be introduced by variable atmospheric conditions when applying a standardized algorithm across large regions and over different dates, we make use of the atmospherically corrected USGS surface reflectance climate data record (CDR) product available for the Landsat TM and ETM+ sensors [37]. The surface reflectance CDR applies atmospheric correction routines originally developed for the Moderate Resolution Imaging Spectroradiometer (MODIS) to Landsat data. Surface reflectance is computed using the Second Simulation of a Satellite Signal in the Solar Spectrum (6S) radiative transfer model, which requires water vapor, ozone, geopotential height, aerosol optical thickness, and a digital elevation model along with Landsat TOA reflectance data. Application of 6S at high latitudes does violate the assumption of a plane-parallel atmosphere, which can impact the quality of surface reflectance product. However, because this is the standard atmospheric correction approach currently applied to all Landsat scenes and because we have not seen any evidence of errors large enough to affect the ability to discriminate between ice or snow and other surfaces in high latitude Landsat surface reflectance data, we have opted to use the standardized Landsat surface reflectance product.

For the RGI calibration and RGI validation study areas, we acquired and processed Landsat top-of-atmosphere (TOA) reflectance and surface reflectance products [36] from all available Landsat TM and ETM+ scenes available during the late summer (in this case defined as 1 August–15 September) for five-year periods. The TOA and surface reflectance Landsat scene products were produced by and acquired from the USGS EROS Data Center. We used the EarthExplorer interface to identify scenes acquired during the time period of interest at each of our study areas and then submitted orders for the identified scenes, subset to our study areas, using the EROS Science Processing Architecture (ESPA) interface. For the RGI calibration and RGI validation study areas, scenes were acquired for the five-year period centered on the date of the RGI inventory. At the Saltfjellet, Norway primary study area we acquired data from an additional year (for a total of six years) due to the poor availability of cloud-free scenes over the five-year period centered on the RGI mapping year. For the VHRI validation study areas, we acquired Landsat scenes for the 2010–2014 period, as the very high resolution imagery was acquired during 2014 or 2015.

3.2. *Randolph Glacier Inventory Data*

At each of the four RGI calibration study areas, we used glacier polygons provided by the RGI (version 4.0) to conduct sensitivity analysis for two key thresholds described below, as well as to conduct an accuracy assessment of mapped glacier area using our automated approach. The RGI provides polygon datasets of all glaciers in a region mapped using a variety of image resources, including Landat TM and ETM+ data. While the imagery source and mapping approach are not identified in the RGI database, the date or range of dates used to map each glacier are included in the database for most entries. Although some RGI polygons indicate a range of years and others provide no information about date or year of the image or other resource used for mapping, all RGI data used in this study indicated a specific date or range of dates within a single year covering the entire extent of each 35 × 35 km study area.

4. Methods

For each pixel in the study domain, our approach identifies the available cloud-free, shadow-free (and otherwise valid) land surface views and then compiles a stack of NDSI values corresponding to each valid land surface view. A threshold value is then applied to the stack of NDSI values to identify each land surface view in the stack as snow or ice-covered or snow or ice-free. The ratio of days with snow/ice to the total days, which we refer to as the fraction of Days with Ice or Snow Cover (fDISC) is then computed and a second threshold value is used to identify the pixel as PISC or PISC-free. A diagram of this processing flow is presented in Figure 2.

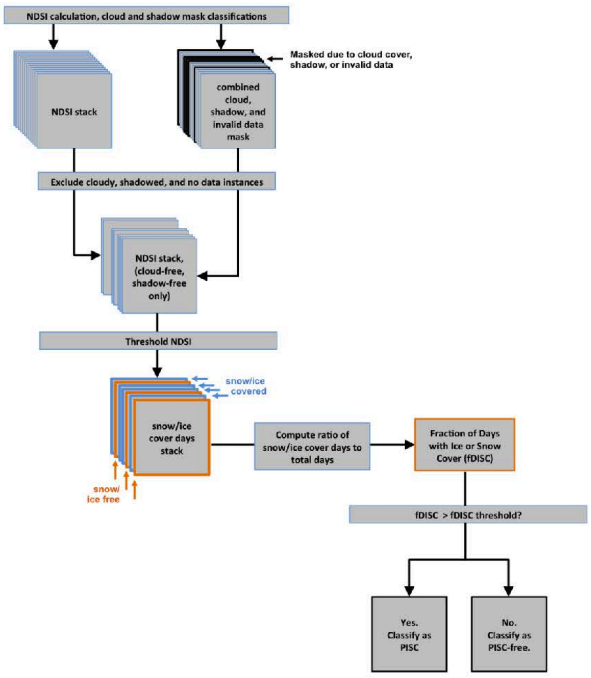

Figure 2. Diagram of processing flow for classification of Persistent Ice and Snow Cover (PISC) for a single pixel.

4.1. Cloud and Shadow Masking

Analysis of stacks of numerous Landsat scenes requires an accurate automated cloud-masking approach. The CFmask algorithm [38] uses a series of rules based on cloud physical properties to develop a potential cloud layer from Landsat top-of-atmosphere reflectance data in bands 1–5 and 7 as well as brightness temperature from band 6. The potential cloud layer is then segmented to produce cloud objects, and ultimately a cloud mask and cloud-shadow mask that is provided with each USGS Climate Data Record (CDR) Landsat surface reflectance scene. While the overall accuracy of the CFmask cloud mask has been reported as 96.4%, our evaluation of CFmask cloud masks found that in rocky, alpine terrain and areas with a mixture of snow, ice, and other land cover types, the CFmask algorithm was prone to errors of commission (false positives) for cloud cover (an example is shown in Figure 3). More importantly, the errors of commission were not randomly distributed across areas with rock and ice cover, but were consistently present at the same patches of land cover on multiple occasions, thus resulting in a potential bias in available cloud-free data. We considered the high rate of errors of commission and particularly the potential for bias to be unacceptable for our purposes. We implemented a revised cloud masking approach designed to reduce errors of commission from the CFmask cloud masks over mountainous environments dominated by rock, snow, and ice, allowing us to fully exploit nearly all available cloud-free land surface views acquired during the late summer period. The revised cloud masking approach employed classification trees that reevaluated all instances of pixels where the CFmask product indicated cloud cover. The classification trees were originally developed for a seasonal snow covered area monitoring project and are based on over 100,000 pixels acquired from 20 Landsat scenes from mountainous areas across the globe. The classification tree approach relies on data from Landsat bands 1–5 and 7 to make a final distinction between cloud-covered and cloud-free pixels in cases where the original CFmask indicated cloud cover. Testing of the classification tree approach in conjunction with the original CFmask data indicated a slight improvement in overall accuracy (from 89% to 91%), with a major improvement in accuracy for high mountain areas from around the globe with substantial snow and ice cover (from 66% to 88%).

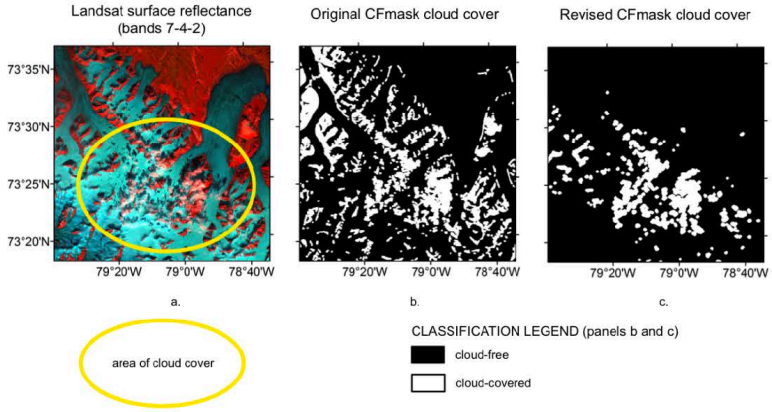

Figure 3. Comparison of original CFmask and revised CFmask for Bylot Island Landsat scene acquired 12 August 1999. (**a**) Landsat surface reflectance 7-4-2 band combination; (**b**) original CFmask cloud cover classification; and (**c**) revised CFmask cloud cover classification.

In addition to cloud cover, both cloud shadows and terrain shadows can impact surface reflectance to the extent that band ratios such as the NDSI no longer provide a reliable indication

of land surface characteristics. We excluded the most deeply shadowed pixels from further analysis by masking pixels where apparent surface reflectance in both bands 2 and 4 was <7%, as all land surface types in our region (with the exception of water) would be expected to exceed 7% reflectance in one or both of these bands. While our shadow masking approach was relatively unsophisticated and did not differentiate between cloud shadows and terrain shadows, we found it to be effective for our needs and ideal in that it required neither accurate cloud heights (for cloud shadow masking) nor accurate digital elevation model data (for terrain shadow masking).

All ETM+ scenes acquired after 2002 included missing data due to the failure of the Landsat 7 scan line corrector. Pixels that were not sampled due to the scan line corrector failure were identified and excluded from further analysis along with pixels identified as cloud-covered or shadowed.

4.2. *Snow and Ice Mapping*

For each late summer cloud-free, shadow-free view of the earth surface within our study areas, the normalized difference snow index (NDSI) [39,40] was used to discriminate between snow and ice free land and snow or ice cover. The NDSI typically exhibits positive values for partially and fully snow or ice covered land and negative values for most other land surface types. For the Landsat TM and ETM+ sensors, NDSI is defined by the following equation [39]:

$$\text{NDSI} = (\text{TM}_2 - \text{TM}_5)/(\text{TM}_2 + \text{TM}_5) \quad (1)$$

where TM_2 is surface reflectance in Landsat TM or ETM+ band 2, and TM_5 is surface reflectance in Landsat TM or ETM+ band 5. The Landsat TM and ETM+ sensors are prone to saturation in the visible bands, including band 2 used in the calculation of the NDSI, over bright surfaces such as snow and ice cover. This problem is more pronounced, however, at lower latitudes where higher levels of incoming solar radiation result in higher levels of reflected solar radiation over comparable surfaces. We calculated the incidence of saturation in band 2 for all scene subsets used in our study areas and found that saturation occurred in only 0.7% of cloud-free surface views.

While NDSI values close to 1.0 almost always indicate relatively fresh snow cover with high albedo and values <0 almost always indicate snow-free or ice-free land, the threshold used for identification of snow cover presence has varied considerably in previous applications, prompting us to undertake an uncertainty analysis, described in detail below. The most appropriate threshold value for discrimination between snow-covered and snow-free pixels depends on several factors, including contamination with dust or fine debris, snow grain size, illumination characteristics, as well as the minimum subpixel snow cover fraction for which positive identification of snow cover is desired.

In addition to an NDSI threshold used to discriminate between ice/snow cover and ice/snow-free land for each available cloud-free, shadow-free land surface view, it was also necessary to establish a threshold for the total fraction of late summer days with ice/snow cover above which a pixel is considered to be PISC (Figure 2). We refer to this second threshold as fDISC (fraction of Days with Ice or Snow Cover). If ice/snow cover could be identified with perfect accuracy, it would make sense to identify a pixel as PISC only if the selected NDSI threshold was exceeded in all available cloud-free and shadow-free land surface views. However, the lack of a well-established NDSI threshold as well as the occasional errors of omission in the cloud masking approach (resulting in the inclusion of cloud-covered pixels in the dataset of cloud-free and shadow-free pixel observations) complicated the situation. Due to these and potentially other complicating factors, we hypothesized that the optimum threshold for fDISC indicating PISC at a pixel would be lower than 1.0.

We addressed the uncertainty in optimum values for both the NDSI threshold and the fDISC threshold by conducting sensitivity analyses to determine the impact of variation in threshold values on classification results. For NDSI threshold values ranging from 0.2 to 0.5 (using increments of 0.1) and for fDISC threshold values ranging from 0.6 to 1.0 (using increments of 0.05), we computed PISC maps for each incremental value and compared the PISC maps to the RGI glacier outlines for the

period, calculating the fraction of total pixels in agreement for each instance. Results of the sensitivity analysis, as well as the threshold value we selected for the final version of our algorithm are discussed in Section 5.

4.3. Additional Processing Steps

We reduced the number of cases where small perennial snow patches or very late lying seasonal snow patches were mapped as PISC by applying stricter standards for mapping PISC in smaller patches less than 300 pixels (27 ha) in size. This was accomplished by applying a sieve routine [41] at two different steps in the processing. The initial sieve routine was applied to identify patches mapped as PISC (based on an fDISC threshold of 0.8) <300 contiguous pixels (27 ha) in size. Pixels within these patches were then reclassified as snow/ice-free if they did not exceed the NDSI threshold in all available cloud-free, shadow-free Landsat surface views. Pixels located within larger patches of PISC (>300 contiguous pixels in size) were not subject to the stricter threshold and were mapped as PISC as long as they exceeded the NDSI threshold in at least 80% of cloud-free, shadow-free views. We also applied a second sieve routine to remove any mapped patches of PISC <100 pixels (9 ha) in size. While the implementation of the sieve routines did result in some errors of omission (false negatives) for small glaciers, it substantially reduced the error of commission and ensured that only the largest perennial snow cover patches were included in our inventory of PISC. Finally, to minimize speckle in the resulting classification, we implemented a post-processing 5 × 5 pixel median filter.

4.4. Accuracy Assessment

We assessed the accuracy of the resulting PISC maps at each study area by comparing PISC maps from our approach to the glacier outlines from the RGI. While the accuracy at the four RGI calibration study areas could potentially be biased because those study areas were used to identify optimal threshold values for NDSI and fDISC used in the algorithm, the four RGI validation study areas and the VHRI validation study areas were included to allow for an unbiased assessment at study areas that had not been used in the algorithm development.

For each VHRI study area, an image analyst manually identified polygons of glacier ice. The set of polygons mapped as ice-covered were then converted to a binary 30-m raster dataset. The 30-m binary ice cover image was then compared to the PISC maps produced from the automated approach.

For the calculation of accuracy assessment metrics, we considered the RGI-derived or VHRI-derived glacier maps to be "truth" in the comparison with PISC maps computed using our approach. Using this assumption, we placed each pixel into one of four categories: (1) true positive (PISC mapped in both our approach and in the RGI or VHRI dataset); (2) false positive (PISC mapped in our approach, but ice-free land indicated by the RGI or VHRI dataset); (3) true negative (ice-free land mapped in both our approach and the RGI or VHRI dataset); and (4) false negative (ice free land mapped in our approach, but ice-cover mapped in the RGI or VHRI dataset). Based on these four categories, for each study area we calculated metrics commonly employed in assessment of binary snow and ice cover maps [42,43]: overall accuracy, precision (the user's accuracy for the glacier and perennial snow cover class), recall (the producer's accuracy for the glacier and perennial snow cover class), and F (a metric that incorporates both precision and recall). Accuracy, precision, recall, and F metrics were calculated using the following equations:

$$\text{Accuracy} = (\text{TP} + \text{TN})/(\text{TP} + \text{TN} + \text{FP} + \text{FN}) \quad (2)$$

$$\text{Precision} = \text{TP}/(\text{TP} + \text{FP}) \quad (3)$$

$$\text{Recall} = \text{TP}/(\text{TP} + \text{FN}) \quad (4)$$

$$\text{F} = 2\text{TP}/(2\text{TP} + \text{FP} + \text{FN}) \quad (5)$$

where TP is the number of true positive pixels, TN is the number of true negative pixels, FP is the number of false positive pixels, and FN is the number of false negative pixels. At each study area, we also calculated each assessment metric for all pixels with a given number of cloud-free and shadow-free land surface views to assess the impact of the number of observations on accuracy.

5. Results

5.1. Overall Accuracy

After considering the effect of the NDSI and fDISC thresholds on accuracy, discussed further below, we selected an NDSI threshold of 0.4 and fDISC threshold of 0.8. All results presented below use these threshold values (unless otherwise noted).

The mean overall accuracy for the primary and RGI validation datasets, defined here as agreement with the RGI validation dataset, was 0.964, while mean overall precision (user's accuracy for the PISC class) was 0.918, mean overall recall (producer's accuracy for the PISC class) was 0.863, and mean F was 0.883. The mean overall accuracy for the VHRI validation study areas was 0.968, while mean overall precision was 0.948, mean overall recall was 0.928, and mean overall F was 0.935. Accuracy, precision, and recall, as well as the spatial distribution of errors, are shown in Figure 4 for the RGI calibration and RGI validation study areas and in Figure 5 for the VHRI validation study areas.

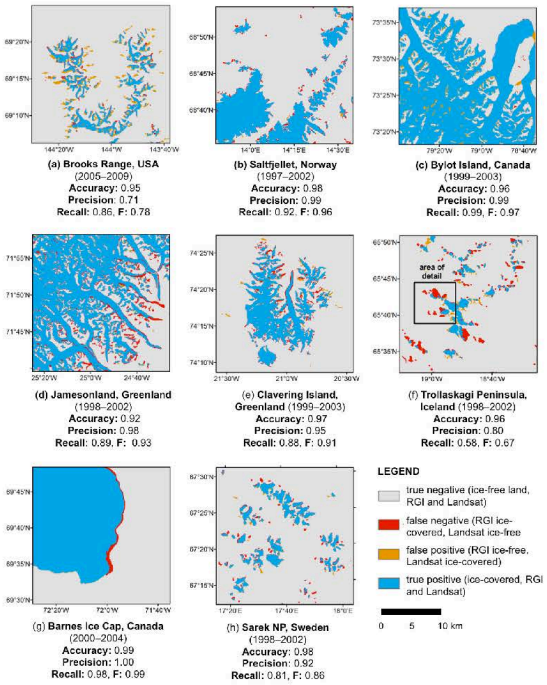

Figure 4. Agreement with the Randolph Glacier Inventory (RGI) glacier extent for each full study area and validation study area. (**a**) Brooks Range, USA; (**b**) Saltfjellet, Norway; (**c**) Bylot Island, Canada; (**d**) Jamesonland, Greenland; (**e**) Clavering Island, Greenland; (**f**) Trollaskagi Peninsula, Iceland; (**g**) Barnes Ice Cap, Canada; (**h**) Sarek NP, Sweden.

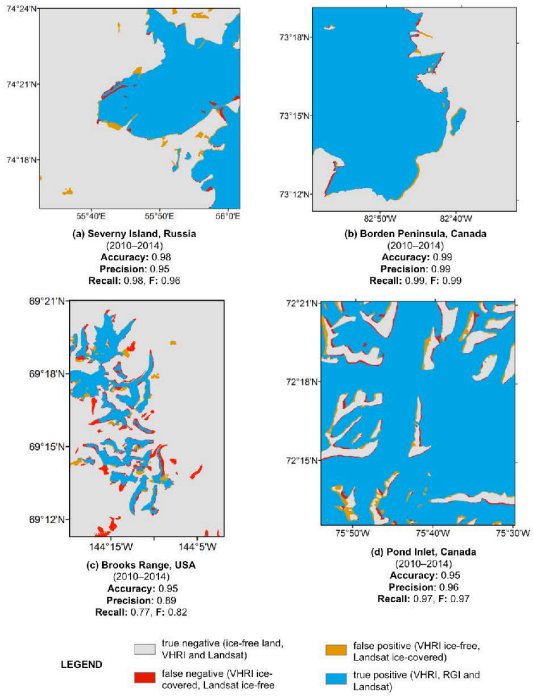

Figure 5. Agreement with VHRI-derived glacier extent for each VHRI validation study area. (**a**) Severny Island, Russia; (**b**) Borden Peninsula, Canada; (**c**) Brooks Range, USA; (**d**) Pond Inlet, Canada.

While most Landsat-derived PISC maps closely resemble those from the RGI or from VHRI, we observed several notable differences. At the Trollaskagi Peninsula study area (Figure 4f), a substantial area mapped as ice-covered by the RGI was mapped as PISC-free by our technique. Closer examination of imagery data from this area, shown in Figure 6, indicated that most of the difference between glacier extent mapped by the RGI and PISC mapped by our technique was due to the RGI's inclusion of substantial areas of debris-covered ice that is spectrally more similar to nearby ice-free land than to ice or snow cover. For the Brooks Range RGI calibration study area, our approach mapped numerous patches of PISC not mapped by the RGI (Figure 4a). Most of these false positive ice cover patches mapped by our technique were located in areas that were deeply shadowed by surrounding terrain during the latter part of our mapping period. As a result, our mapping approach was only able to consider data from the earlier part of the mapping period. Areas that become heavily shadowed later in the mapping period tend to receive lower levels of incoming solar radiation throughout the earlier part of the summer as well, and consequently often retain seasonal snow cover for all but a few weeks of the year. In many cases, this brief snow-free period does not begin until these areas have already become heavily shadowed, and consequently, there are no valid Landsat surface views of these areas after they have become snow free. Finally, at the Brooks Range VHRI validation study area, several small- and medium-sized glaciers identified by the RGI were not mapped as PISC. This is likely due to the strict requirement that patches of PISC smaller than 300 contiguous pixels be mapped as snow or ice covered in every cloud-free and shadow-free surface

view. As a result, if NDSI dropped below 0.4 due to debris cover or cloud-contamination for any of the available cloud-free and shadow-free surface views, pixels part of these smaller patches of PISC were not mapped as PISC.

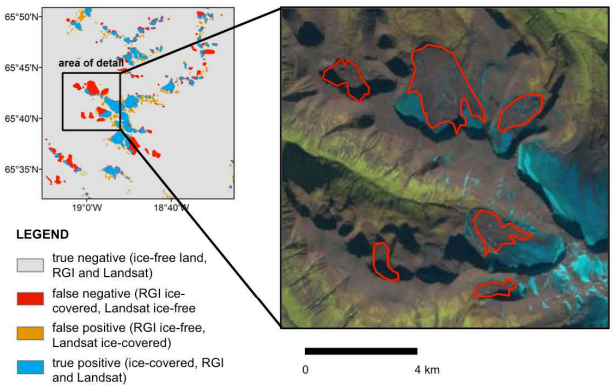

Figure 6. Agreement between mapped PISC and glaciers mapped with RGI for the Trollaskagi Peninsula, Iceland, with area of detail showing Landsat imagery and areas of false positives for PISC outlined in red.

5.2. Factors Affecting Persistent Ice and Snow Cover Map Accuracy

5.2.1. Use of Original CFmask *vs.* Revised Cloud Masking Approach

The number of cloud-free and shadow-free land surface views available differed considerably depending on the cloud masking approach used, with substantially more views available for some pixels when the revised cloud masking approach, rather than the original CFmask cloud classification provided with the Landsat surface reflectance product, was used (Table 2, Figure 7). In addition, well-defined fine scale spatial patterns related to terrain and land cover type were apparent in the mapped total number of cloud-free and shadow-free views calculated using the original CFmask algorithm cloud masks, but not in the mapped total number of cloud-free and shadow-free views calculated using the revised cloud masking approach (Figure 7). While coarser scale patterns in the geographic distribution of cloud cover likely do exist, the well-defined fine scale patterns in the number of cloud-free views mapped by CFmask suggest a tendency to classify specific types of land cover and terrain as cloud-covered even in the absence of actual cloud cover (such as the example provided in Figure 3). While in some cases the mean number of cloud and shadow free surface views was not substantially different, at three of the four study areas, the percentage of pixels with <5 cloud-free and shadow-free surface views was substantially higher when the original CFmask was used for cloud identification (Table 2).

The reduced frequency of pixels with <5 cloud-free and shadow-free surface views for the revised cloud masking approach is not, in and of itself, an indication that the revised cloud masking approach is more effective, as this could simply indicate increased errors of omission for cloud cover. Analysis from previous work we conducted to assess the suitability of the standard CFmask product for seasonal snow cover monitoring applications does, however, indicate that in mountainous areas where fine scale mixtures of rock, snow, and ice are common, errors of commission (false positives) for cloud cover are widespread for the standard CFmask product. A different but equally useful way to compare the utility of the original and revised cloud masking approaches is to compare the accuracy (in this case, agreement with the RGI glacier extent) of mapped PISC using the original

CFmask algorithm with the accuracy of mapped PISC using the revised cloud masking approach. This comparison indicated that in the majority of cases, the revised cloud masking approach yielded more accurate final results, and that at some study areas (particularly the Brooks Range), the improvement in accuracy was substantial (Figure 8).

Table 2. Comparison of cloud-free and shadow-free surface views (CFSFSV) for each study area using the original CFmask and the revised cloud masking approach.

Study Area	Original CFmask		Revised Approach	
	Mean CFSFSV	Pixels with <5 CFSFSV	Mean CFSFSV	Pixels with <5 CFSFSV
Brooks Range	15.0	11.0%	20.8	1.2%
Saltfjellet	7.3	28.2%	10.0	9.1%
Bylot Island	29.4	0.0%	29.5	0.0%
Jamesonland	14.4	4.3%	16.4	0.8%

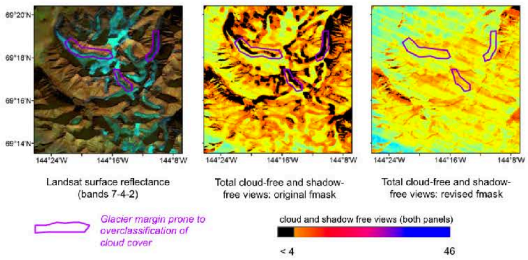

Figure 7. Cloud-free and shadow-free views for a subset of the Brooks Range study area using the original CFmask and the revised cloud masking approach. Examples of glacier margins where false cloud cover was consistently identified, resulting in <4 cloud-free and shadow-free surface views are highlighted in purple.

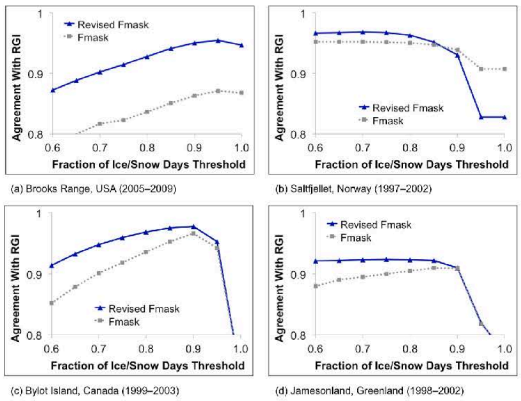

Figure 8. Accuracy (agreement with the RGI) for each study area as a function of late summer snow cover days threshold using the original CFmask and the revised cloud masking approach. (**a**) Brooks Range, USA; (**b**) Saltfjellet, Norway; (**c**) Bylot Island, Canada; (**d**) Jamesonland, Greenland.

5.2.2. Normalized Difference Snow Index (NDSI) threshold

The NDSI threshold value used to distinguish between ice/snow covered and ice/snow free land for individual dates had a relatively small effect on accuracy in most instances, although the impact of NDSI threshold was often larger for cases well outside the optimum range of thresholds for fraction of late summer snow cover days (Figure 9). At the optimum fDISC threshold (between 0.7 and 0.95, depending on the study area), differences in accuracy associated with variable NDSI thresholds between 0.2 and 0.5 were minimal.

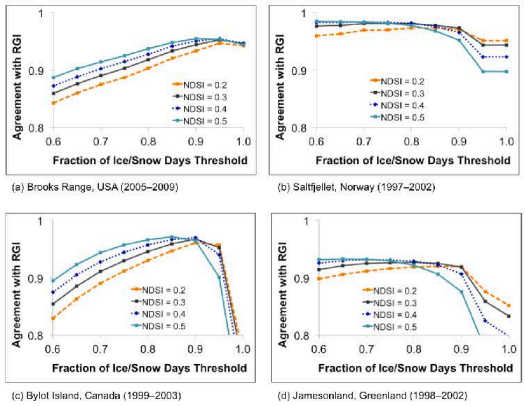

Figure 9. Effect of fraction of Days With Ice and Snow Cover (fDISC) threshold and Normalized Difference Snow Index (NDSI) threshold on PISC map accuracy (defined as agreement with RGI glacier area) for each RGI calibration study area. (**a**) Brooks Range, USA; (**b**) Saltfjellet, Norway; (**c**) Bylot Island, Canada; (**d**) Jamesonland, Greenland.

5.2.3. Fraction of Days with Ice and Snow Cover (fDISC) Threshold

The fDISC threshold used to classify pixels as PISC had a larger impact on accuracy than the NDSI threshold (Figure 9). The optimal fDISC threshold value fell between 0.7 (for Saltjellet, Norway) and 0.95 (for the Brooks Range, USA). For the Brooks Range and Bylot Island study areas, agreement with the RGI increased steadily for threshold values above 0.6, peaked around 0.9, and then decreased (dramatically in the case of Bylot Island). For the Saltjellet, Norway, and Jamesonland, Greenland study areas, accuracy was quite stable for threshold values between 0.6 and 0.8, with a gradual decline in accuracy at higher threshold values.

5.2.4. Selection of Algorithm Threshold Values for NDSI fDISC

Based on the sensitivity analysis presented above, we selected an NDSI threshold value of 0.4 and an fDISC threshold value of 0.8. We selected the NDSI threshold of 0.4 because in all cases we analyzed, the 0.4 NDSI curve included the optimum accuracy value or fell only slightly below the optimum accuracy value. The wider variability in the value of the optimum fDISC threshold presented more of a challenge for selecting the ideal threshold for the algorithm that would be applied across all study areas. While a higher threshold between 0.9 and 0.95 worked best at the Bylot Island and Brooks Range study areas, a lower threshold around 0.7 resulted in the highest accuracy at the Saltfjellet, Norway, and Jamesonland, Greenland sites. To select the threshold with the highest accuracy across the greatest range of sites, we selected a threshold of 0.8, which had yielded accuracy above 0.9 for all four RGI calibration study areas.

5.2.5. Number of Cloud-Free and Shadow-Free Land Surface Views

In the majority of cases, both the precision and recall accuracy metrics increased as the number of cloud-free and shadow-free surface views increased (Figure 10), as we might intuitively expect. In addition, the rate of increase leveled off in almost all cases, although the number of cloud free views at which this plateau was reached varied substantially across sites, from as few as 4 cloud-free and shadow-free views to as many as 30 cloud-free and shadow-free views. The Trollaskagi Peninsula in Iceland presented an unusual exception, with the recall metric decreasing steadily as a function of number of cloud and shadow free views. The poor overall accuracy as well as the inverse relationship between cloud-free, shadow-free views and recall for the Trollaskagi Peninsula study area are likely due to large areas of debris-covered ice mapped in the RGI but not identified as PISC in our approach. In most cases, precision was low when <10 cloud-free and shadow-free surface views were available. The Barnes Ice Cap study area provided a notable exception, where high precision was observed regardless of the number of cloud-free, shadow-free surface views. Conversely, the recall metric was low at the Barnes Ice Cap Study Area for cases where <20 cloud-free and shadow-free surface views were available, although this did not have a large effect on overall accuracy at this study area since >20 cloud-free and shadow-free surface views were available at the vast majority of pixels.

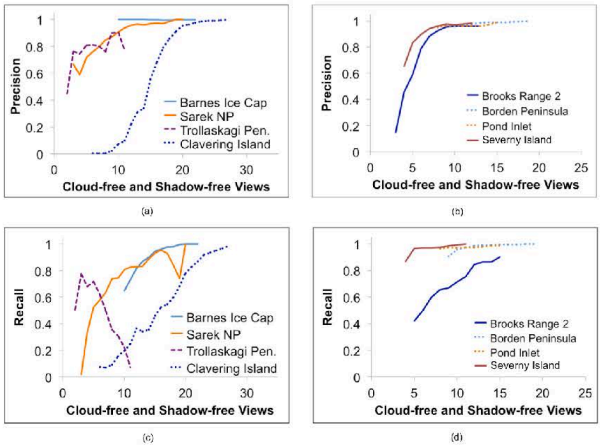

Figure 10. Effect of number of cloud and shadow free views on precision (user's accuracy for the ice covered class) and recall (producer's accuracy for the ice-covered class) for RGI validation study areas and VHRI validation study areas. (**a**) Effect of the number cloud-free and shadow-free views on precision for the RGI validation study areas; (**b**) effect of the number of cloud-free and shadow-free views on precision for VHRI validation study areas; (**c**) effect of the number of cloud-free and shadow-free views on recall for the RGI validation study areas; and (**d**) effect of the number of cloud-free and shadow-free views on recall for VHRI validation study areas.

5.3. Spatial Distribution of Errors

Figures 4 and 5 depict the spatial distribution of errors of commission (false positives) and errors of omission (false negatives) for each of the twelve study areas. While the frequency, type, and distribution of errors varies by study area, some common patterns emerge. False negatives are often concentrated along the margins of glaciers, and particularly near the end of glacier tongues where heavy debris cover is present. False positives, on the other hand, are more frequently concentrated in patches that are not contiguous with larger glaciers, particularly in the Brooks Range RGI calibration

study area, Brooks Range VHRI validation study area, and Severny Island VHRI validation study area. These small patches appear to be primarily patches of late lying or perennial snow cover. Late lying seasonal snow cover patches mapped as PISC appear to be most common in areas that experience deep shadowing during the latter part of the image acquisition period. As a result, valid surface views are only available for these locations during the earlier part of the image acquisition period, when these areas are still snow covered, and as a result they are classified as PISC.

6. Discussion

6.1. Effect of Fraction of Days with Ice/Snow Cover (fDISC) Threshold

Our results suggest that a standardized approach where pixels with fDISC values >0.8 are classified as PISC should work well across much of the northern high latitude regions. However, the data also suggest that it may be possible to optimize the algorithm for specific regions by adjusting the fDISC threshold. The optimum value for this threshold will depend on a number of factors, including the prevalence of late lying seasonal snow patches in the region, the typical duration of seasonal snow cover, the prevalence of partially debris-covered ice on the lower portions of the glacier, and the number of cloud-free land surface views available.

Although we might intuitively expect a PISC mapping approach would perform best by mapping PISC only at pixels where all cloud-free and shadow-free views contained snow or ice cover, our results suggest this is not the case. While the optimum fDISC threshold value varies by study region, the optimum threshold is <1.0 for all study areas, and for the Bylot Island and Jamesonland study areas, accuracy drops off substantially as fDISC approaches 1.0. There are two primary reasons why the optimum threshold is consistently <1.0. First, because we know that the cloud mapping approach will occasionally classify cloud-contaminated pixels as cloud-free, we expect that cloud-contaminated observations of snow or ice cover will typically have lower NDSI values than cloud-free snow or ice and will often be mapped as free of snow and ice. Using a strict approach (equivalent to an fDISC threshold value of 1.0) would ensure that PISC pixels with even one cloud-contaminated view would be mapped as ice-free. Second, areas of PISC with debris cover will generally have NDSI values that decline over the course of the summer as more debris is exposed. While areas of PISC with partial debris cover will likely always maintain a positive NDSI value (as opposed to the majority of other land surface types, which will indicate negative NDSI values when snow-free), the NDSI value may briefly drop below the NDSI threshold (in this case 0.4), resulting in an occasional surface view that would be classified as free of snow and ice. Again, in these situations, using the strict approach with an fDISC threshold value of 1.0 would classify these pixels as ice-free.

6.2. Advantages and Disadvantages in Comparison to Traditional Semi-Automated Approaches

The automated PISC mapping approach presented here has both advantages and disadvantages when compared to more traditional approaches employed to produce the majority of existing glacier inventories. The primary advantage of the automated approach we present here is that it can be applied over large areas quickly, without the need for a substantial time investment from skilled analysts. This allows for generation of comprehensive PISC maps covering multiple time periods, allowing for analysis of changes in PISC extent over time. Prior to conducting this type of analysis, however, it will be necessary to develop techniques to distinguish between true changes in PISC and changes resulting in differences between the available data from different periods of comparison as well as changes in seasonal snow cover. With appropriate techniques for change analysis, we expect this type of approach could be used to map general trends in ice-covered area over time. Finally, the automated approach also ensures that results will be completely reproducible and not dependent on the level of expertise of a particular image analyst.

Perhaps the largest disadvantage of the automated approach is that it does not take into account contextual information, such as topographic position, patch size and shape, or snow or ice texture that

an expert image analyst might be able to use to distinguish between glacier ice and perennial or late lying seasonal snow cover. To minimize the inclusion of perennial snow cover and late lying seasonal snow cover patches, we eliminate all patches mapped as PISC that are <100 contiguous pixels (~9 ha). While this minimum size threshold is somewhat larger than the thresholds typically used in more traditional glacier mapping approaches, we found that it substantially reduces the incidence of false positives while only slightly increasing the incidence of false negatives. Analysis of glaciers within our study areas indicates that, according to the RGI, glaciers <9 ha in size are entirely absent (or not mapped) in several of our study areas and account for only a tiny fraction of the total ice covered area where they are present, such as in the Brooks Range, where they account for just 0.6% of the ice covered area.

Another key disadvantage of the automated approach is that the mapped PISC cannot be tied to a single year, but instead maps PISC for a five-year period. This would become more important if the automated approach is implemented for the purpose of monitoring changes in PISC over time. In addition, the automated approach requires a number of late summer cloud-free views to be effective, while more traditional approaches where an image analyst carefully selects scenes for analysis can be effective if only a single, well-timed cloud-free scene is available. Finally, an image analyst can also typically identify large debris-covered glacier tongues, although delineating the exact extent of these features can be challenging even in cases where high resolution imagery is available [29]. In our automated mapping approach, partially debris-covered portions of glaciers may be mapped as PISC, particularly if seasonal snow cover is present for many of the late summer land surface views. Fully debris-covered portions of glaciers, however, will generally not be mapped as PISC. The difficulty of mapping debris-covered glacier ice has been a consistent problem for optical remote sensing efforts, and while several approaches have shown promise for automated mapping of debris-covered glacier ice [44–46], accurate mapping of debris-covered glacier ice will likely require some combination of manual editing or incorporation of other types of remotely sensed data.

Finally, it is important to note that conventional glacier inventories (such as those available from the RGI) identify and map individual glaciers, whereas our automated approach only identifies the extent of PISC. A single contiguous patch of ice cover mapped using our automated approach may represent two or more distinct glaciers separated by a drainage divide. Therefore, even in cases where the mapped extent of PISC corresponds perfectly with the extent of glacier ice, additional processing is necessary to generate outlines corresponding to individual glaciers. While in some cases this step can be accomplished with an automated approach, in certain cases (such as when the available DEM data is of poor quality), manual editing may be required.

6.3. Importance of Revised Cloud Masking Approach

The revised cloud masking approach implemented here appears to be crucial to the success of the overall approach, as the data indicate that using the original CFmask would result in substantial regions with <5 cloud-free and shadow-free observations due to frequent false positives for cloud cover over certain types of terrain and land cover. Most notably, many of these regions of consistent cloud cover commission errors are located along the margins of glaciers, which would result in a disproportionately large effect on the accuracy of the final product. This effect is confirmed by comparison of accuracy between versions of our approach implemented using the original CFmask classification and the revised cloud masking approach.

6.4. Application of the Approach to Lower Latitude Regions

A similar approach to the one presented here may be effective for mapping PISC in lower latitude regions. As the effective implementation of this approach relies on multiple cloud-free views during a relatively short window, we expect a similar approach would be most effective for lower latitude regions where cloudy days are relatively rare during the period when seasonal snow cover is at its minimum, as well as in regions where nearly all potential Landsat scenes have been archived (such

as the conterminous U.S. and southern Canada). Application of this approach for lower latitude regions may also require adjustment of the seasonal window for Landsat scene inclusion. Finally, the relatively greater abundance of debris-covered glaciers at lower latitudes may present a problem given that the automated approach is not effective for mapping glaciers with extensive, optically thick debris cover.

6.5. Future Research

Future research should address the key disadvantages discussed above. In particular, it may be possible to compute various shape and texture metrics from the Landsat imagery as well as incorporate topographic information from a DEM and then use a machine learning approach to exploit some of the contextual information used by expert image analysts and improve classification accuracy. In addition, while we did not use any Landsat OLI data in our implementation of the automated approach because OLI data from only two late-summer periods had been acquired, Landsat OLI data offer several advantages that have the potential to improve classification accuracy. First, the higher radiometric range in the visible bands as well as the additional cirrus cloud detection band should allow for even more accurate cloud masking, resulting in fewer cloud-covered pixels being included in the analysis, as well as fewer cloud-free pixels omitted from the analysis. Second, the storage and transmission capacity of the Landsat 8 platform allows for collection of a greater number of scenes outside the conterminous United States, potentially allowing for shorter analysis windows (e.g., three years rather than five). While these improvements present the opportunity for more accurate monitoring of PISC, any efforts comparing PISC mapped with Landsat 5 (TM) or Landsat 7 (ETM+) instruments with PISC mapped with the Landsat 8 (OLI) instrument will need to carefully consider the potential impact of the differences in instrument specifications (particularly radiometric saturation in the visible bands) to ensure an unbiased analysis of change.

Unfortunately, the Landsat surface reflectance product was not optimized for atmospheric correction at higher latitudes. Because the plane parallel atmosphere assumption used in the 6S radiative transfer model is violated to some extent in our study region, the resulting surface reflectance data provided may be less accurate than similar data acquired at lower latitudes. The overall impact on mapping accuracy, however, is likely to be low, as our sensitivity analysis demonstrates that accuracy is much more impacted by the fDISC threshold than by the NDSI threshold. However, future improvements in the USGS surface reflectance CDR that improve accuracy at higher latitudes could potentially result in higher accuracy for our automated mapping approach.

7. Conclusions

We demonstrate the feasibility of accurate monitoring of debris-free PISC across the northern high latitudes using automated processing of Landsat TM and ETM+ data that does not require manual intervention from an image analyst at any point in the processing chain. This approach is made possible by the availability of a standardized Landsat surface reflectance product, the large number of scenes at high latitudes due to Landsat path overlap, and an enhancement to the standard Landsat surface reflectance cloud mask that reduces the occurrence of cloud cover false positives in mountainous, partially snow covered environments. Based on eight study areas distributed throughout the northern high latitudes, we found that results from our fully automated mapping approach are generally comparable to those obtained from the RGI at six of the eight RGI study areas. At the Trollaskagi, Iceland RGI validation site, agreement with the RGI glacier extent was very poor due to the substantial areas of debris-covered glaciers mapped by the RGI, while at the Brooks Range RGI calibration study area, agreement with the RGI database was lower than at most other sites due to the considerable amount of perennial and late lying seasonal snow cover mapped in areas indicated to be ice-free by the RGI. Our results agreed well with glacier maps derived from high resolution imagery at three of four validation sites, with lower accuracy at the Brooks Range

site resulting from false negatives for portions of glaciers frequently in shadow and for portions of glaciers with substantial debris cover.

The approach presented here has the potential to quickly map PISC across large high latitude regions and provide important updates regarding the status of PISC, which can be particularly valuable when the resources to conduct more precise, traditional glacier monitoring efforts are not available.

Acknowledgments: Funding for this research was provided by the Land Remote Sensing Program of the US Geological Survey. We also wish to thank Daniel McGrath and four anonymous reviewers who provided substantial feedback for improving the manuscript.

Author Contributions: David J. Selkowitz developed the glacier mapping, validation, and cloud masking approaches. Richard R. Forster assisted with the development of the study design and interpretation of the results.

Conflicts of Interest: The authors declare no conflict of interest.

References

1. Lemke, P.; Ren, J.; Alley, R.B.; Allison, I.; Carrasco, J.; Flato, G.; Fujii, Y.; Kaser, G.; Mote, P.; Thomas, R.H.; *et al.* Observations: Changes in snow, ice and frozen ground. In *Climate Change 2007—The Physical Science Basis: Working Group I Contribution to the Fourth Assessment Report of the IPCC*; Solomon, S., Qin, D., Manning, M., Chen, Z., Marquis, M., Averyt, K., Tignor, M., Miller, H.L., Jr., Eds.; Cambridge University Press: Cambridge, UK; New York, NY, USA, 2007; Chapter 4; pp. 337–384.
2. Stocker, T.; Qin, D.; Plattner, G.-K.; Tignor, M.; Allen, S.K.; Boschung, J.; Nauels, A.; Xia, Y.; Bex, V.; Midgley, P.M. *Climate Change 2013: The Physical Science Basis*; Cambridge University Press: Cambridge, UK; New York, NY, USA, 2014.
3. Sessa, R.; Dolman, H. *Terrestrial Essential Climate Variables for Climate Change Assessment, Mitigation and Adaptation (GTOS 52)*; Food and Agriculture Organization of the United Nations: Rome, Italy, 2008.
4. Fairbanks, R.G. A 17,000-year glacio-eustatic sea level record: Influence of glacial melting rates on the Younger Dryas event and deep-ocean circulation. *Nature* **1989**, *342*, 637–642. [CrossRef]
5. Meier, M.F.; Dyurgerov, M.B.; Rick, U.K.; O'Neel, S.; Pfeffer, W.T.; Anderson, R.S.; Anderson, S.P.; Glazovsky, A.F. Glaciers dominate eustatic sea-level rise in the 21st century. *Science* **2007**, *317*, 1064–1067. [CrossRef] [PubMed]
6. Broccoli, A.; Manabe, S. The influence of continental ice, atmospheric CO_2, and land albedo on the climate of the last glacial maximum. *Clim. Dyn.* **1987**, *1*, 87–99. [CrossRef]
7. Jacob, T.; Wahr, J.; Pfeffer, W.T.; Swenson, S. Recent contributions of glaciers and ice caps to sea level rise. *Nature* **2012**, *482*, 514–518. [CrossRef] [PubMed]
8. Barnett, T.P.; Adam, J.C.; Lettenmaier, D.P. Potential impacts of a warming climate on water availability in snow-dominated regions. *Nature* **2005**, *438*, 303–309. [CrossRef] [PubMed]
9. Kääb, A.; Reynolds, J.M.; Haeberli, W. Glacier and permafrost hazards in high mountains. In *Global Change and Mountain Regions*; Huber, U.M., Bugmann, H.K.M., Reasoner, M.A., Eds.; Springer: Dordrecht, The Netherlands, 2005; pp. 225–234.
10. Richardson, S.D.; Reynolds, J.M. An overview of glacial hazards in the Himalayas. *Quat. Int.* **2000**, *65*, 31–47. [CrossRef]
11. Zemp, M.; Hoelzle, M.; Haeberli, W. Six decades of glacier mass-balance observations: A review of the worldwide monitoring network. *Ann. Glaciol.* **2009**, *50*, 101–111. [CrossRef]
12. Haeberli, W. Glaciers and ice caps: Historical background and strategies of worldwide monitoring. In *Mass Balance of the Cryosphere*; Bamber, J.L., Payne, A.J., Eds.; Cambridge University Press: Cambridge, UK, 2004; pp. 559–578.
13. Hall, D.; Chang, A.; Foster, J.; Benson, C.; Kovalick, W. Comparison of *in situ* and Landsat derived reflectance of Alaskan glaciers. *Remote Sens. Environ.* **1989**, *28*, 23–31. [CrossRef]
14. Hall, D.; Ormsby, J.; Bindschadler, R.; Siddalingaiah, H. Characterization of snow and ice reflectance zones on glaciers using Landsat Thematic Mapper data. *Ann. Glaciol.* **1987**, *9*, 104–108.
15. Ventura, A.D.; Rampini, A.; Rabagliati, R.; Barbero, R.S. Development of a satellite remote sensing technique for the study of alpine glaciers. *Int. J. Remote Sens.* **1987**, *8*, 203–215. [CrossRef]

16. Williams, R.S., Jr.; Hall, D.K.; Benson, C.S. Analysis of glacier facies using satellite techniques. *J. Glaciol.* **1991**, *37*, 120–128.
17. Winther, J.G. Landsat TM derived and *in situ* summer reflectance of glaciers in Svalbard. *Polar Res.* **1993**, *12*, 37–55. [CrossRef]
18. Rundquist, D.; Collins, S.; Barnes, R.; Bussom, D.; Samson, S.; Peake, J. The use of Landsat digital information for assessing glacier inventory parameters. *Int. Assoc. Hydrol. Sci.* **1980**, *126*, 321–331.
19. Hall, D.K.; Benson, C.S.; Field, W.O. Changes of glaciers in Glacier Bay, Alaska, using ground and satellite measurements. *Phys. Geogr.* **1995**, *16*, 27–41.
20. Aniya, M.; Sato, H.; Naruse, R.; Skvarca, P.; Casassa, G. The use of satellite and airborne imagery to inventory outlet glaciers of the Southern Patagonia Icefield, South America. *Photogramm. Eng. Remote Sens.* **1996**, *62*, 1361–1369.
21. Jacobs, J.D.; Simms, É.L.; Simms, A. Recession of the southern part of Barnes Ice Cap, Baffin Island, Canada, between 1961 and 1993, determined from digital mapping of Landsat TM. *J. Glaciol.* **1997**, *43*, 98–102.
22. Paul, F.; Kääb, A.; Maisch, M.; Kellenberger, T.; Haeberli, W. The new remote-sensing-derived Swiss glacier inventory: I. Methods. *Ann. Glaciol.* **2002**, *34*, 355–361. [CrossRef]
23. Bolch, T.; Menounos, B.; Wheate, R. Landsat-based inventory of glaciers in western Canada, 1985–2005. *Remote Sens. Environ.* **2010**, *114*, 127–137. [CrossRef]
24. Bliss, A.; Hock, R.; Cogley, J.G. A new inventory of mountain glaciers and ice caps for the Antarctic periphery. *Ann. Glaciol.* **2013**, *54*, 191–199. [CrossRef]
25. Rastner, P.; Bolch, T.; Mölg, N.; Machguth, H.; le Bris, R.; Paul, F. The first complete inventory of the local glaciers and ice caps on Greenland. *Cryosphere* **2012**, *6*, 1483–1495. [CrossRef]
26. Guo, W.; Liu, S.; Xu, J.; Wu, L.; Shangguan, D.; Yao, X.; Wei, J.; Bao, W.; Yu, P.; Liu, Q.; *et al.* The second Chinese glacier inventory: Data, methods and results. *J. Glaciol.* **2015**, *61*, 357–372. [CrossRef]
27. Bishop, M.P.; Olsenholler, J.A.; Shroder, J.F.; Barry, R.G.; Raup, B.H.; Bush, A.B.G.; Copland, L.; Dwyer, J.L.; Fountain, A.G.; Haeberli, W.; *et al.* Global land ice measurements from space (GLIMS): Remote sensing and GIS investigations of the earth's cryosphere. *Geocarto Int.* **2004**, *19*, 57–84. [CrossRef]
28. Raup, B.; Racoviteanu, A.; Khalsa, S.J.S.; Helm, C.; Armstrong, R.; Arnaud, Y. The GLIMS geospatial glacier database: A new tool for studying glacier change. *Glob. Planet. Chang.* **2007**, *56*, 101–110. [CrossRef]
29. Pfeffer, W.T.; Arendt, A.A.; Bliss, A.; Bolch, T.; Cogley, J.G.; Gardner, A.S.; Hagen, J.-O.; Hock, R.; Kaser, G.; Kienholz, C.; *et al.* The Randolph Glacier Inventory: A globally complete inventory of glaciers. *J. Glaciol.* **2014**, *60*, 537–552. [CrossRef]
30. Paul, F.; Barrand, N.E.; Baumann, S.; Berthier, E.; Bolch, T.; Casey, K.; Frey, H.; Joshi, S.P.; Konovalov, V.; Bris, R.L.; *et al.* On the accuracy of glacier outlines derived from remote-sensing data. *Ann. Glaciol.* **2013**, *54*, 171–182. [CrossRef]
31. Paul, F.; Bolch, T.; Kääb, A.; Nagler, T.; Nuth, C.; Scharrer, K.; Shepherd, A.; Strozzi, T.; Ticconi, F.; Bhambri, R.; *et al.* The glaciers climate change initiative: Methods for creating glacier area, elevation change and velocity products. *Remote Sens. Environ.* **2015**, *162*, 408–426. [CrossRef]
32. Arvidson, T.; Gasch, J.; Goward, S.N. Landsat 7's long-term acquisition plan—An innovative approach to building a global imagery archive. *Remote Sens. Environ.* **2001**, *78*, 13–26. [CrossRef]
33. Ju, J.; Roy, D.P. The availability of cloud-free Landsat ETM+ data over the conterminous United States and globally. *Remote Sens. Environ.* **2008**, *112*, 1196–1211. [CrossRef]
34. Irish, R.R. *Landsat 7 Science Data Users Handbook*; National Aeronautics and Space Administration: Washington, DC, USA, 2000.
35. Burns, P.; Nolin, A. Using atmospherically-corrected Landsat imagery to measure glacier area change in the Cordillera Blanca, Peru from 1987 to 2010. *Remote Sens. Environ.* **2014**, *140*, 165–178. [CrossRef]
36. Paul, F.; Kääb, A. Perspectives on the production of a glacier inventory from multispectral satellite data in arctic Canada: Cumberland Peninsula, Baffin Island. *Ann. Glaciol.* **2005**, *42*, 59–66. [CrossRef]
37. Masek, J.G.; Vermote, E.F.; Saleous, N.E.; Wolfe, R.; Hall, F.G.; Huemmrich, K.F.; Gao, F.; Kutler, J.; Lim, T.-K. A Landsat surface reflectance dataset for North America, 1990–2000. *IEEE Geosci. Remote Sens. Lett.* **2006**, *3*, 68–72. [CrossRef]
38. Zhu, Z.; Woodcock, C.E. Object-based cloud and cloud shadow detection in Landsat imagery. *Remote Sens. Environ.* **2012**, *118*, 83–94. [CrossRef]

39. Dozier, J. Spectral signature of alpine snow cover from the Landsat Thematic Mapper. *Remote Sens. Environ.* **1989**, *28*, 9–22. [CrossRef]
40. Riggs, G.; Hall, D.K.; Salomonson, V.V. A snow index for the Landsat Thematic Mapper and Moderate Resolution Imaging Spectroradiometer. In Proceedings of the IEEE International Surface and Atmospheric Remote Sensing: Technologies, Data Analysis and Interpretation, Geoscience and Remote Sensing Symposium (IGARSS '94), Pasadena, CA, USA, 8–12 August 1994; pp. 1942–1944.
41. ITT Visual Information Solutions. *ENVI User's Guide. ENVI on-Line Software User's Manual*; ITT Visual Information Solutions: Boulder, CO, USA, 2008.
42. Rittger, K.; Painter, T.H.; Dozier, J. Assessment of methods for mapping snow cover from MODIS. *Adv. Water Resour.* **2013**, *51*, 367–380. [CrossRef]
43. Painter, T.H.; Brodzik, M.J.; Racoviteanu, A.; Armstrong, R. Automated mapping of earth's annual minimum exposed snow and ice with MODIS. *Geophys. Res. Lett.* **2012**. [CrossRef]
44. Bolch, T.; Buchroithner, M.F.; Kunert, A.; Kamp, U. Automated delineation of debris-covered glaciers based on ASTER data. In Proceedings of the 27th EARSeL Symposium, Geoinformation in Europe, Bolzano, Italy, 4–7 June 2007; pp. 4–6.
45. Paul, F.; Huggel, C.; Kääb, A. Combining satellite multispectral image data and a digital elevation model for mapping debris-covered glaciers. *Remote Sens. Environ.* **2004**, *89*, 510–518. [CrossRef]
46. Shukla, A.; Arora, M.; Gupta, R. Synergistic approach for mapping debris-covered glaciers using optical-thermal remote sensing data with inputs from geomorphometric parameters. *Remote Sens. Environ.* **2010**, *114*, 1378–1387. [CrossRef]

CHAPTER 4

AUTOMATED MAPPING OF PERSISTENT ICE AND SNOW COVER ACROSS THE WESTERN US WITH LANDSAT

Selkowitz, D. J., & Forster, R. R. (2016). Automated mapping of persistent ice and snow cover across the western US with Landsat. *ISPRS Journal of Photogrammetry and Remote Sensing*, *117*, 126-140. Published by Elsevier 2016.

ISPRS Journal of Photogrammetry and Remote Sensing 117 (2016) 126–140

Contents lists available at ScienceDirect

ISPRS Journal of Photogrammetry and Remote Sensing

journal homepage: www.elsevier.com/locate/isprsjprs

Automated mapping of persistent ice and snow cover across the western U.S. with Landsat

David J. Selkowitz [a,b,*], Richard R. Forster [b]

[a] US Geological Survey, Alaska Science Center, 4210 University Drive, Anchorage, AK 99508, USA
[b] Department of Geography, University of Utah, 260 S. Central Campus Dr., Rm. 270, Salt Lake City, UT 84112, USA

ARTICLE INFO

Article history:
Received 30 September 2015
Received in revised form 23 March 2016
Accepted 1 April 2016

Keywords:
Glaciers
Snow and ice
Landsat

ABSTRACT

We implemented an automated approach for mapping persistent ice and snow cover (PISC) across the conterminous western U.S. using all available Landsat TM and ETM+ scenes acquired during the late summer/early fall period between 2010 and 2014. Two separate validation approaches indicate this dataset provides a more accurate representation of glacial ice and perennial snow cover for the region than either the U.S. glacier database derived from US Geological Survey (USGS) Digital Raster Graphics (DRG) maps (based on aerial photography primarily from the 1960s–1980s) or the National Land Cover Database 2011 perennial ice and snow cover class. Our 2010–2014 Landsat-derived dataset indicates 28% less glacier and perennial snow cover than the USGS DRG dataset. There are larger differences between the datasets in some regions, such as the Rocky Mountains of Northwest Wyoming and Southwest Montana, where the Landsat dataset indicates 54% less PISC area. Analysis of Landsat scenes from 1987–1988 and 2008–2010 for three regions using a more conventional, semi-automated approach indicates substantial decreases in glaciers and perennial snow cover that correlate with differences between PISC mapped by the USGS DRG dataset and the automated Landsat-derived dataset. This suggests that most of the differences in PISC between the USGS DRG and the Landsat-derived dataset can be attributed to decreases in PISC, as opposed to differences between mapping techniques. While the dataset produced by the automated Landsat mapping approach is not designed to serve as a conventional glacier inventory that provides glacier outlines and attribute information, it allows for an updated estimate of PISC for the conterminous U.S. as well as for smaller regions. Additionally, the new dataset highlights areas where decreases in PISC have been most significant over the past 25–50 years.
Published by Elsevier B.V. on behalf of International Society for Photogrammetry and Remote Sensing, Inc. (ISPRS).

1. Introduction

Glaciers act as sensitive indicators of climate change (Lemke et al., 2007; Oerlemans, 2005), responding to both changes in temperature and precipitation (McCabe and Fountain, 2013). Along with perennial and seasonal snow cover, they often serve as an important source of freshwater runoff for people living downstream (Barnett et al., 2005; Immerzeel et al., 2010), but can also pose a risk to these populations due to glacial lake outburst floods and other hazards (Kääb et al., 2005; Moore et al., 2009; Richardson and Reynolds, 2000). Perennial snow cover is also common in regions with glaciers and is often present in regions where glaciers are absent or have recently disappeared.

Substantial evidence indicates that the majority of the world's glaciers are currently retreating (Dyurgerov and Meier, 2000; Kaser et al., 2006; Stocker et al., 2014), although rates of ice loss vary substantially across regions and over time. Extensive loss of glacier ice has been documented across the Western conterminous United States and the neighboring Canadian provinces of British Columbia and Alberta. Glacier area decreased by 7% between 1958 and 1998 in the North Cascades of Washington (Granshaw and Fountain, 2006), the region with the largest concentration of ice cover in the conterminous U.S. Several hundred kilometers to the south, glaciers have declined in area on Mount Adams by 49% between 1904 and 2006 (Sitts et al., 2010). Further south, in the Sierra Nevada of California, an average ice loss of 55% occurred between 1903 and 2004 (Basagic and Fountain, 2011). In the Rocky Mountains of Wyoming, ice cover decreased in the Wind River Range by approximately 47% between 1900 and 2006 (DeVisser and Fountain, 2015), and 39% between 1967 and 2006 (Maloof et al., 2014). In the nearby Teton Range, ice cover declined by

* Corresponding author at: US Geological Survey, Alaska Science Center, 4210 University Drive, Anchorage, AK 99508, USA.
E-mail addresses: dselkowitz@usgs.gov (D.J. Selkowitz), rick.forster@geog.utah.edu (R.R. Forster).

http://dx.doi.org/10.1016/j.isprsjprs.2016.04.001
0924-2716/Published by Elsevier B.V. on behalf of International Society for Photogrammetry and Remote Sensing, Inc. (ISPRS).

25% between 1967 and 2006 (Edmunds et al., 2012). In Glacier National Park in northwest Montana, glaciers in the Blackfoot-Jackson Basin declined in area by 66% between 1850 and 1979 (Hall and Fagre, 2003) and by 29% between 1966 and 2005 (US Geological Survey 2013). Finally, in adjacent areas of Canada, glaciers decreased in area by 11% in British Columbia and 24% in Alberta between 1985 and 2005 (Bolch et al., 2010).

Although the loss of ice has been well documented for individual glaciers and small regions and many of these efforts have produced updated glacier inventories, the best available glacier database covering the entire conterminous western U.S. remains a dataset that is based on aerial photography flown primarily between the 1960s and 1980s. This dataset, hereafter referred to as the USGS DRG dataset, is derived from 1:100,000 US Geological Survey Digital Raster Graphics (DRG) map products and is available online at http://glaciers.us/Downloads (Fountain et al., 2007). The well-documented pattern of glacier retreat across the region means that this inventory, which is generally 25–50 years old, will not reflect the current state of glaciers and perennial snow cover across many areas in the region. An updated inventory of glaciers and perennial snow covering the entire region and attributable to a well constrained period within the last few years is thus needed. A comprehensive, precise inventory of glaciers covering the entire region based on recent high spatial resolution imagery at sub-meter resolution would require a substantial amount of resources to acquire and process the necessary imagery as well as digitize and label all glacier and perennial snow cover features. While updated DRGs and associated National Hydrography Dataset layers have been produced for many areas, the majority of the updates are based on imagery 5–15 years old that cover a >10 year range in dates and have not been compiled into a single regional inventory of glaciers and perennial snow cover. More importantly, given high rates of change for glaciers and perennial snow cover, any updated dataset is likely to become outdated within just a few years.

Recently, several studies have demonstrated the feasibility of monitoring snow and ice conditions across individual glaciers or small basins using ground-based high spatial resolution time lapse photography (Farinotti et al., 2010; Bernard et al., 2013). In addition, airborne monitoring approaches have been increasingly utilized to provide regularly updated estimates of snow cover conditions including areal extent and snow depth for portions of mountain ranges (McGurk and Painter, 2013). Despite the effectiveness of these approaches and the rich information they can provide, implementing these approaches across a region as large as the Western U.S. has not been feasible due to high costs.

A potential alternative to techniques using regular ground-based or airborne monitoring approaches is to use an automated mapping approach to develop a map of persistent ice and snow covered area (PISC) from satellite imagery that can be updated automatically every few years as new imagery becomes available. Data from the Landsat series of sensors have been widely used for nearly thirty years for mapping glaciers and perennial snow cover (Aniya et al., 1996; Hall et al., 1987; Jacobs et al., 1997; Ventura et al., 1987), with recent efforts covering regions as large or larger than the western U.S. (Bolch et al., 2010; Guo et al., 2015; Rastner et al., 2012). Many recent mapping efforts have begun to incorporate semi-automated mapping approaches rather than traditional manual digitization techniques. Even semi-automated mapping approaches, however, typically still require a substantial effort to select the most appropriate scenes to minimize cloud-cover and seasonal snow cover. The effort required for scene selection becomes quite substantial if the region of interest covers more than a few Landsat scenes, as is the case in the western U.S.

In 2008, the US Geological Survey made all Landsat scenes available to the scientific community at no-cost, enabling new research that exploited the availability of numerous scenes acquired over time covering a single frame (referred to as a path/row). Since the opening of the archive, a number of recent studies covering a wide range of remote sensing applications have demonstrated the utility of processing stacks of Landsat scenes to monitor the evolution of land surface characteristics and ultimately extract information that could not be provided by individual scenes or even annual scene acquisitions. These studies have included impervious surface mapping (Zhang and Weng, 2016), surface water monitoring (Tulbure and Broich, 2013), forest mapping (Zhu and Liu, 2014), and seasonal snow cover monitoring (Macander et al., 2015). Along these lines, Selkowitz and Forster (2015) recently developed an automated PISC mapping approach that considers all available Landsat scenes for a given time period (typically 5 years) and does not require an analyst to select the most appropriate scenes. This type of fully automated approach has some disadvantages because it does not capitalize on an analyst's ability to select the best scenes or distinguish between ice and seasonal snow cover based on contextual clues. It has an important advantage, however, in that it can be implemented for a large region such as the western U.S. quickly and with far fewer resources than would be required for a conventional manual or semi-automated glacier inventory.

Here we present an updated 30 m resolution map of PISC across the conterminous western United States developed using a fully automated mapping approach that exploits all available Landsat TM and ETM+ scenes acquired between August 20 and September 30 during the 2010–2014 period. The approach can potentially be implemented in any region with sufficient Landsat scene availability. The new dataset allows for updated estimates of PISC area across the western U.S. and for individual sub-regions or mountain ranges, and, in conjunction with the existing glacier inventory derived from USGS topographic maps, can be used to construct rough estimates of changes in PISC area since the mid to late 20th century.

Before proceeding, it is important to note that while glaciers are moving bodies of ice and perennial snow cover patches are merely snowfields that persist for many years without disappearing, in practice, it is not always straightforward to differentiate between small glaciers and perennial snow cover patches. This is particularly true when mapping is conducted via remote sensing. In the United States, standard topographic maps produced by the USGS and used to construct the US Glacier inventory have not, in most cases, formally differentiated between glaciers and perennial snow cover patches, and in some cases may even include late lying seasonal snow cover patches (Fountain et al., 2007). While we recognize that an ideal dataset would effectively distinguish between glaciers, perennial snow cover, and late lying seasonal snow cover, we also recognize that this is often not possible when inventories are developed using remote sensing. Therefore, we refer to all areas mapped as perennial ice or snow features as persistent ice or snow cover (PISC) to avoid any confusion.

2. Study area and methods

2.1. Study area

The Landsat-derived PISC map covers the western half of the conterminous United States and includes all mountain ranges where PISC was mapped in the USGS DRG dataset (Fig. 1). The major mountain ranges of the western United States with perennial snow and ice features include the Cascades in Washington, Oregon, and northern California, the Olympic Mountains in Washington, the Sierra Nevada in California, and the Rocky Mountains in Colorado, Wyoming, Montana, and Idaho. Several small glaciers and perennial snow cover patches have also been identified in smaller mountain ranges located between the coastal

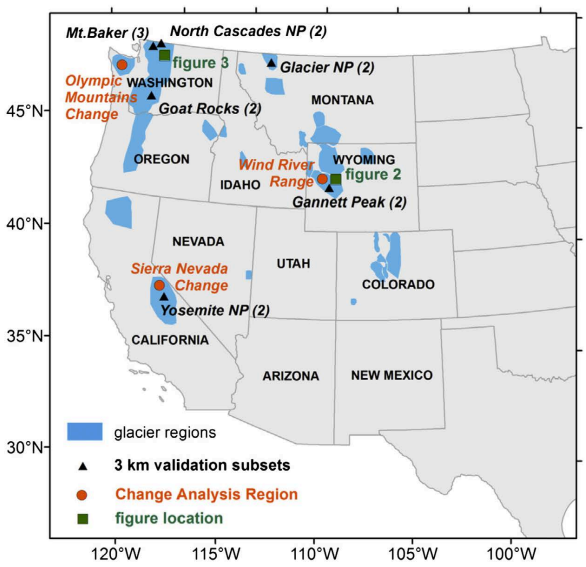

Fig. 1. Overview map of the western United States, including glacier regions defined by the USGS DRG dataset, very high resolution imagery (VHRI) validation subsets, change analysis regions, and locations for other figures.

ranges and the Rocky Mountains, but are not included in this analysis as they are generally smaller than the minimum mapping unit of 2 ha used in this analysis. While the Cascades and Sierra Nevada typically exhibit maritime snow climates with heavy precipitation and temperatures near 0 °C throughout much of the winter, the Rocky Mountains typically exhibit more continental conditions, with lower precipitation totals and winter temperatures well below 0 °C at higher elevations.

The USGS DRG dataset indicates the Cascades contained approximately 413 km^2 of PISC, with about 90% of the total PISC area mapped in the Cascades located in Washington state, 9% located in Oregon, and 1% located in northern California. With the exception of the northernmost portion of the range, PISC in the Cascades is generally confined to isolated volcanic peaks. The USGS DRG dataset indicates Washington's Olympic Mountains contain an additional 41.9 km^2 of PISC concentrated within a relatively small area of 9000 km^2. Both the Cascade and Olympic ranges include several medium-sized glaciers covering >3 km^2 that account for a substantial portion of the total area of PISC in each range. To the south of the Cascades, 11.4 km^2 of PISC, composed entirely of small glaciers and perennial snow cover patches, has been mapped in the Sierra Nevada of California. In the Rocky Mountains of Wyoming and Montana, the USGS DRG dataset maps 108 km^2 of PISC, with several glaciers in the Lewis and Clark and Wind River Ranges >1 km^2. Finally, the USGS DRG dataset maps about 2 km^2 of PISC scattered across the Rocky Mountains of Colorado.

2.2. Data

2.2.1. The USGS DRG dataset: digital glacier outlines from USGS topographic maps

The USGS DRG dataset, which has sometimes also been referred to as the US Glacier Database, is a vector dataset of glacier and perennial snow cover patch outlines developed from 1:100,000 Digital Raster Graphics (DRG) maps produced by the USGS (Fountain et al., 2007). The database includes all glaciers and perennial snow cover features mapped in the 1:100,000 series of topographic maps. Maps were produced primarily from aerial photography acquired during the 1960s through the 1980s, although a small number of maps may have used aerial photography from as early as the 1940s. The metadata for this dataset clearly states that not all features included in the database meet the qualifications to be considered active glaciers. In addition to the set of polygons indicating the extent of individual glaciers or perennial snow patches, the database also provides a set of polygons identifying 27 mountain regions where PISC has been mapped.

2.2.2. Landsat data

We obtained 30 m resolution Landsat Climate Data Record (CDR) top-of-atmosphere (TOA) and surface reflectance products (Masek et al., 2006) for Landsat Thematic Mapper (TM) and Enhanced Thematic Mapper (ETM+) scenes located within glacier regions identified by the USGS DRG dataset. We used the USGS LSDS Science Research and Development (LSRD) bulk order tool to order, subset, and reproject all Landsat TM and ETM+ scenes acquired between August 20 and September 30 for the 2010–2014 period. The August 20–September 30 period was selected because scenes acquired earlier in the season often contained substantial seasonal snow cover remaining from the previous winter, while scenes acquired after September 30 often included recently accumulated early season snow cover as well as substantial areas in deep shadow in the most northern portion of the region. Using the bulk ordering tool, we subset each scene to the extent of glaciated regions (as defined by the USGS DRG dataset) within the Landsat path/row and reprojected the data to the Albers Equal Area Conic projection used by the National Land Cover Database (NLCD) and other national-scale products. The final PISC classification was developed using data from 754 Landsat scenes from 30 different

Worldwide Reference System 2 (WRS-2) path/rows across the western U.S. The mean number of scenes acquired was 25 per path/row and ranged from 24 to 27.

2.2.3. Land cover and elevation data

We acquired the NLCD 2011 (Jin et al., 2013) land cover classification for the conterminous U.S. in order to assess the extent of PISC mapped by the NLCD as well as for identification of water features that are occasionally mapped as PISC by the automated Landsat approach. While the NLCD 2011 land cover dataset included 25 land cover classes for the conterminous U.S., our analysis focused exclusively on class 11 (open water) and class 12 (perennial ice/snow). We also acquired a seamless 30 m digital elevation model (DEM) covering the conterminous western U.S. from the National Elevation Dataset (NED) (Gesch et al., 2002).

2.2.4. Very high resolution imagery used for validation

We acquired 0.5 m resolution pan-sharpened natural color imagery from the Digital Globe Enhanced View archive for August or September covering 13 separate 3×3 km subsets that each included one or more glacier (Fig. 1). Imagery for each high resolution subset was acquired by the WorldView 2 or WorldView 3 satellites (mention of a specific product does not constitute endorsement by the U.S. government). The selection of very high resolution imagery (VHRI) validation subsets was constrained to 3×3 km blocks containing at least one previously identified glacier where cloud-free August or September imagery from 2010 to 2014 was available and seasonal snow cover was absent or minimal. Allowing for these constraints, we selected subsets intended to represent a range of glacier sizes, topography, and climate conditions.

2.3. Methods

Our approach to mapping PISC uses all available Landsat Thematic Mapper TM and ETM + scenes acquired between August 20 and September 30 during the 2010–2014 period. Cloud-covered and shadowed pixels for each date are identified first and excluded from further analysis. Cloud-free, shadow-free pixels are classified as snow/ice or snow/ice-free for each available cloud-free, shadow-free view. Pixels classified as snow/ice-covered in >80% of available views are initially classified as PISC. We then apply several post-processing routines designed to reduce the occurrence of errors of commission (false positives for PISC), including removing patches of PISC of <25 contiguous pixels, eliminating PISC mapped below a minimum elevation threshold that varies by region, eliminating PISC mapped where the NLCD classification indicates water, and applying a stricter standard to mapping PISC pixels in areas not previously mapped as PISC by the USGS DRG dataset. Fig. 2 provides a visual representation of the approach we used to classify PISC across the study region.

2.3.1. Cloud and shadow masking

Automated approaches to mapping PISC require a fully automated cloud-masking approach that performs well in mountainous environments with mixtures of ice, snow, rock, and other land cover. The CFmask cloud classification (Zhu and Woodcock, 2012) provided with the USGS CDR Landsat surface reflectance products employs a series of rules based on the physical properties of clouds to develop an initial cloud cover classification using Landsat bands 1–5 and 7 as well as brightness temperature from band 6. The initial cloud cover classification is then segmented into cloud objects used to produce the final cloud mask, as well as a cloud shadow mask based on the cloud objects and solar illumination geometry at the time of scene acquisition. While the CFMask represents a substantial improvement over previous cloud classification approaches and accuracy for the CFmask has been reported as 96.4% (Zhu and Woodcock, 2012), previous work has demonstrated that it is prone to mapping false cloud cover in mountainous areas dominated by rock, snow and ice (Selkowitz and Forster, 2015). Examination of several scenes from mountainous areas of the western U.S. indicated that CFmask cloud masks provided with the surface reflectance CDR product frequently identify cloud cover in cloud-free regions where rock, snow, and ice are the dominant land cover types (an example is shown in Fig. 3). Although occasional errors of commission in cloud cover masks are to be expected and would most likely not pose a substantial problem for an automated PISC mapping approach, the errors of commission in the CFmask cloud cover masks present a more serious problem because they tend to occur consistently at certain locations. This can result in clusters of pixels where very few cloud-free, shadow-free views are available (as shown in Fig. 3) and ultimately result in patches of incorrectly mapped PISC.

In order to address this problem and fully exploit all available cloud-free, shadow-free views acquired between August 20 and September 30 each year, we employed a cloud masking approach developed by Selkowitz and Forster (2015) that accepts pixels mapped as cloud-free by the CFmask approach but re-examines any pixels mapped as cloud-covered. Under this approach, pixels identified as cloud-covered by the CFmask are evaluated by a series of classification trees that provide a final, revised cloud mask value. While the classification tree approach relies on much of the same input data as the original CFmask algorithm (with the exception of band 6 brightness temperature, which is not used), the classification trees were developed using a training dataset that included thousands of pixels from mountainous regions dominated by rock, ice and snow cover that were incorrectly classified by the CFmask approach. Selkowitz and Forster (2015) demonstrate that this approach results in a substantial reduction in errors of commission and an increase in accuracy in mountainous regions from 66% to 88% (see Fig. 4).

Both cloud shadows and terrain shadows can also impact surface reflectance values, and in some cases, the impact can be severe enough that band ratios like the NDSI can no longer reliably discriminate between snow or ice and snow or ice free land. Therefore, it is necessary to identify deeply shadowed pixels and exclude them from further analysis in the same manner as cloud-covered pixels. In our approach, we identified and excluded from further analysis all instances where pixels exhibited an apparent surface reflectance of <7% in both bands 2 and 4. With the exception of some water bodies, surface reflectance for all land surface types in the region would be expected to exceed 7% in one or both of these bands. Although our shadow masking approach did not distinguish between cloud shadows and terrain shadows, it was well-suited for our approach because it did not require accurate cloud heights for identification of cloud shadows or a DEM for identification of terrain shadows. It is important to note that there was an additional advantage in using a reflectance threshold rather than a DEM to identify unusable terrain-shadowed pixels. Many pixels a terrain-based shadow masking approach would have identified as unusable due to the absence of modeled direct solar radiation were actually sufficiently illuminated by diffuse solar radiation or radiation reflected from nearby terrain surfaces and were retained for analysis. In total, the combined cloud masking and shadow masking efforts resulted in no cloud-free, shadow-free views of the land surface in about 2.2% of total pixels. These pixels were typically concentrated in small consistently shadowed patches associated with terrain features such as cirque basins.

Missing data, including pixels outside of each Landsat scene as well as pixels not imaged due to the Landsat 7 scan line corrector failure, were also identified and excluded from further analysis.

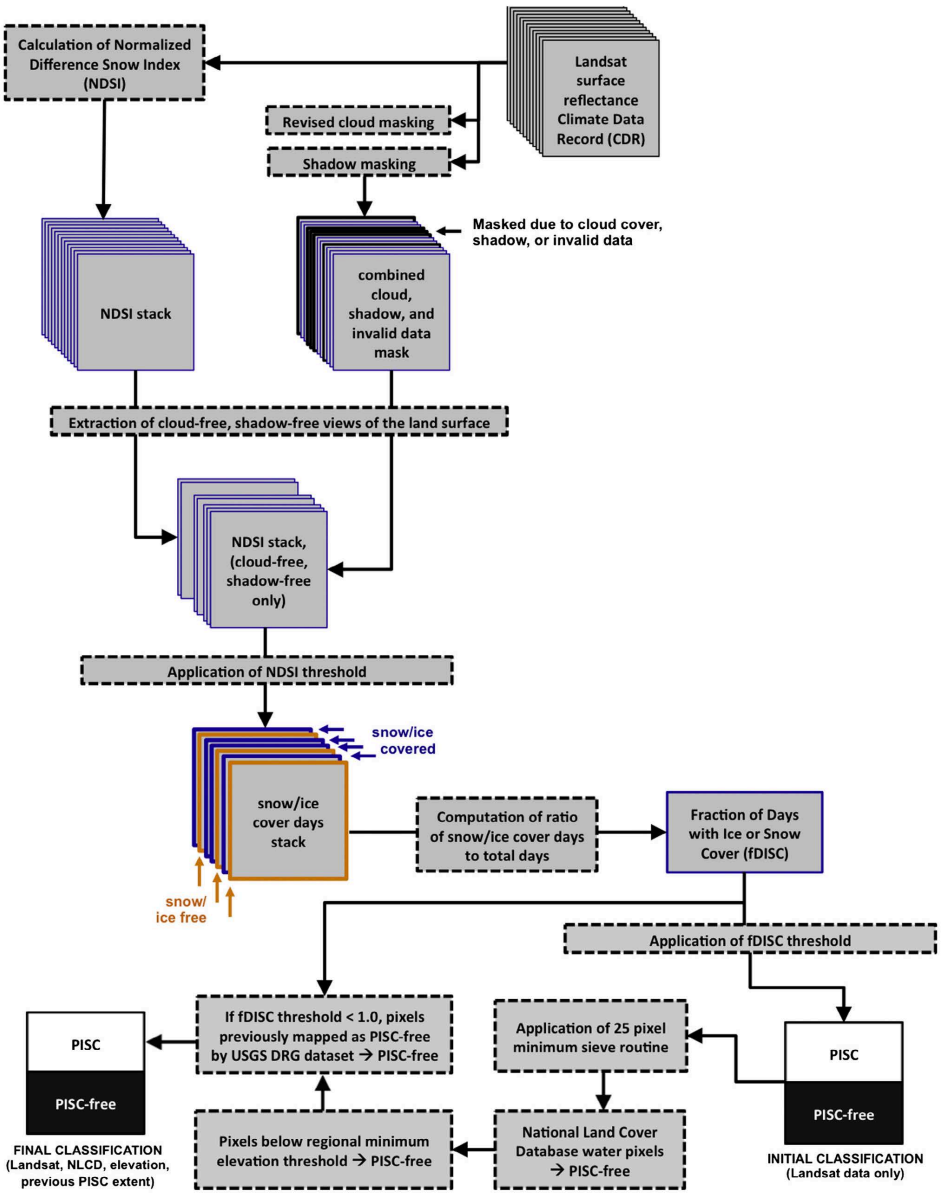

Fig. 2. Diagram of processing flow for classification of Persistent Ice and Snow Cover (PISC).

2.3.2. Ice and snow mapping for individual Landsat scenes

We used the Normalized Difference Snow Index (NDSI) (Dozier, 1989; Riggs et al., 1994) to identify snow or ice cover in each cloud-free, shadow-free view. For Landsat TM and ETM+, NDSI is defined by the following equation:

$$NDSI = (TM_2 - TM_5)/(TM_2 + TM_5) \quad (1)$$

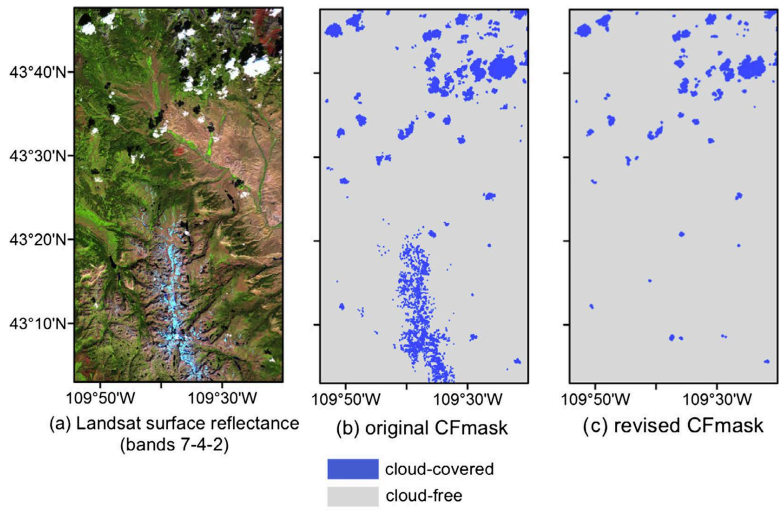

Fig. 3. An example of differences between cloud cover mapped by the CFmask algorithm and the revised cloud masking approach for the Wind River Range of Wyoming. (a) False color Landsat surface reflectance, with clouds appearing white and areas of snow and ice appearing cyan, (b) cloud cover mapped by the original CFmask, and (c) cloud cover mapped by the revised cloud mapping approach. (For interpretation of the references to color in this figure legend, the reader is referred to the web version of this article.)

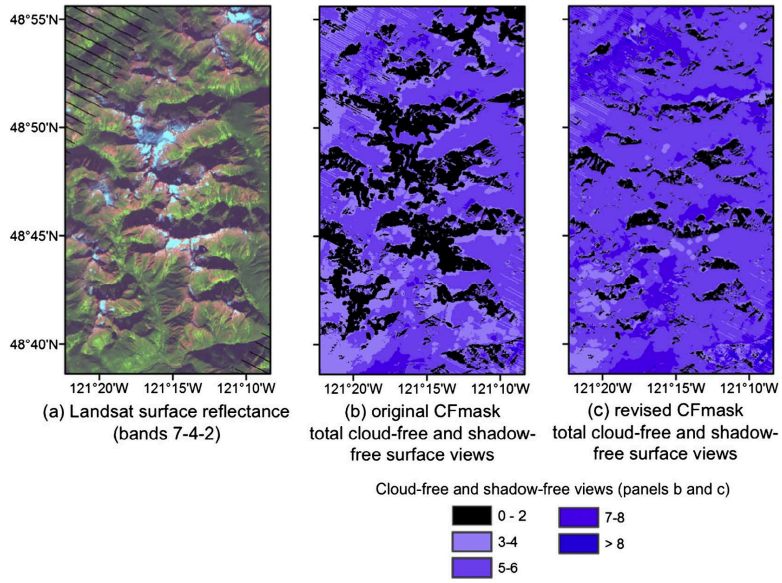

Fig. 4. An example of differences between the number of available cloud-free, shadow-free views resulting from use of the original CFmask algorithm and the revised cloud masking approach for the North Cascades of Washington. (a) Landsat surface reflectance, (b) total cloud-free, shadow-free views available calculated using the original CFmask, and (c) total cloud-free, shadow-free views calculated using the revised cloud mapping approach.

where TM_2 is surface reflectance in Landsat TM or ETM+ band 2 (0.52–0.60 μm), and TM_5 is surface reflectance in Landsat TM or ETM+ band 5 (1.55–1.75 μm). Pixels with NDSI values ⩾0.4 were classified as snow or ice covered while pixels with NDSI values <0.4 were classified as free of snow and ice.

2.3.3. Identification of persistent ice and snow cover pixels

For each pixel, we considered all cloud-free, shadow-free views acquired between August 20 and September 30 for the years 2010–2014 to determine whether the pixel should be classified as PISC. For the initial classification, pixels identified as snow or ice covered in ⩾80% of the available cloud-free, shadow-free views were identified as PISC. While this approach is less intuitive than classifying only pixels with snow or ice mapped in every available cloud-free, shadow-free view as PISC, Selkowitz and Forster (2015) demonstrated that using a threshold value of 80% resulted in higher accuracy for identifying PISC pixels.

2.3.4. Post processing and incorporation of ancillary data

We implemented several post-processing steps primarily designed to reduce the prevalence of errors of commission for PISC. First, we applied a 5 × 5 median filter to reduce spatial noise in the resulting classification. Second, we applied a sieve routine (ITT Visual Information Solutions, 2008) to remove patches of PISC of <25 contiguous pixels. Analysis of our initial PISC maps suggested that, while some small glaciers and true perennial snow cover patches <25 contiguous pixels did exist, the majority of PISC patches of <25 contiguous pixels were actually late lying seasonal snow cover that generally disappeared completely by the end of the summer, which we did not wish to include in our PISC inventory. Third, we used a minimum elevation filter to remove PISC mapped below the minimum elevation at which we would expect to find PISC in each region. A separate minimum elevation was calculated for each glacier region identified by the USGS DRG dataset based on the minimum elevation (extracted from the NED DEM) of glacier polygons mapped by the USGS DRG dataset in that region. For each region, we eliminated any PISC pixels where the NED DEM indicated an elevation value >200 m below the minimum elevation of previously mapped PISC within that region. Fourth, in cases where <100% of cloud-free and shadow-free views of the land surface at a pixel location indicated snow or ice cover, as well as in cases where <3 cloud-free, shadow-free views of the land surface were available at a pixel, we reclassified pixels initially mapped as PISC if they had not previously been mapped as PISC in the USGS DRG dataset. Pixels with >3 cloud-free, shadow-free views of the land surface mapped as snow or ice cover in all available cloud-free and shadow-free views of the land surface were retained as PISC pixels even if they were not mapped as PISC in the USGS DRG dataset. Finally, pixels mapped as PISC where the NLCD classification indicated water (NLCD class 11) were reclassified as free of PISC.

2.3.5. Accuracy assessment

We conducted two separate accuracy assessments of our Landsat-derived PISC map. First, we compared our results to PISC manually identified in the 13 VHRI subsets (locations shown in Fig. 1). Second, we applied a 500 m buffer to the USGS DRG dataset polygons and then randomly selected 1000 points across the western U.S. from within the buffered area (inclusive of previously mapped PISC) to assess the accuracy of our PISC map. For each validation point, we examined all available high resolution imagery in GoogleEarth acquired in 2000 or later to identify the presence or absence of PISC. Google Earth imagery originated from a variety of aerial and satellite imagery programs but typically consisted of natural color imagery at spatial resolutions between 0.2 and 1 m. Points which appeared to be within 30 m of the edge of a glacier or perennial snow cover patch were classified in the same manner as other points, but were also flagged as edge points. Points with debris-covered glacier ice were classified as PISC but also flagged as debris-covered. All points had Google Earth imagery available from at least two dates from the mid summer to early fall period, and many points had five or more dates of Google Earth imagery available. At the vast majority of points, we were able to identify the presence or absence of PISC with high confidence due to either the appearance of bare ground or exposed ice on one or more of the image dates. At the remaining points, we used contextual clues such as patch size, patch shape, topographic position, and imagery date to make a final determination of PISC presence or absence.

For both the randomly selected validation points and the VHRI validation subsets, we calculated accuracy assessment metrics for our Landsat-derived PISC maps, the USGS DRG dataset, and the NLCD dataset by considering the manually interpreted PISC classification from Google Earth imagery or WorldView 2 imagery to be "truth". Comparison between each dataset and the validation datasets resulted in each pixel or point being placed into one of four categories: (1) true positive: PISC mapped in the evaluation dataset and by manual interpretation of high resolution imagery, (2) false positive: PISC mapped in the evaluation dataset, but PISC-free land mapped by manual interpretation of high resolution imagery, (3) true negative: PISC-free land mapped in the evaluation dataset and by manual interpretation of high resolution imagery, and (4) false negative: PISC-free land mapped in the evaluation dataset, but PISC mapped by manual interpretation of high resolution imagery. It is important to note that because the USGS DRG PISC maps and the WorldView 2 PISC maps were based on imagery acquired several decades apart, differences in PISC mapped by the USGS DRG dataset and the WorldView 2 dataset may not reflect mapping errors, but instead indicate potential changes in PISC over time.

Placing each point or pixel into one of these four categories allowed us to calculate several metrics commonly used for assessment of binary snow and ice cover maps (Painter et al., 2012; Rittger et al., 2013): accuracy, precision (the user's accuracy for the PISC class), recall (the producer's accuracy for the PISC class), and F (an accuracy assessment metric designed to balance the importance of precision and recall). The four metrics were calculated using the following equations:

$$\text{Accuracy} = (TP + TN)/(TP + TN + FP + FN) \quad (2)$$

$$\text{Precision} = TP/(TP + FP) \quad (3)$$

$$\text{Recall} = TP/(TP + FN) \quad (4)$$

$$F = 2\,TP/(2\,TP + FP + FN) \quad (5)$$

where TP is the count of true positive pixels, TN is the count of true negative pixels, FP is the count of false positive pixels, and FN is the count of false negative pixels.

We calculated each of the four metrics for each dataset to be evaluated for each 3 × 3 km validation subset as well as for all the 3 × 3 km validation subsets combined. We also calculated the four metrics for each subset of pixels with the same number of cloud-free, shadow-free views of the land surface in order to assess the impact of the number of available views of the land surface on mapping accuracy. Each metric was also calculated for the full set of 1000 randomly selected validation points as well as for a subset of 834 validation points located >30 m from the edge of a glacier or perennial snow cover patch.

2.3.6. Calculation of glacier area by region

We calculated the total area of PISC mapped by our automated Landsat approach, the USGS DRG dataset, and the NLCD for the entire conterminous western U.S., as well as for 8 regions aggregated from the original 27 regions identified in the USGS DRG dataset.

2.3.7. Comparison to conventional Landsat inventories for selected regions

Our initial comparison between PISC area mapped by the USGS DRG dataset and PISC mapped by our automated Landsat approach showed that in some regions, the automated Landsat approach mapped <50% of PISC mapped by the USGS DRG dataset. In order to determine whether differences in PISC area mapped by the USGS DRG dataset and PISC mapped by our automated Landsat approach were due to changes in PISC area over time or differences between the mapping approaches, we selected three subset areas for additional analysis of changes in PISC between 1987–1988 and 2008–2010. We wanted to ensure that our assessment of change for these regions was conservative and did not overestimate decreases in PISC area due to differences in seasonal snow cover conditions. In order to accomplish this, we compared Landsat scenes from years where data from local SNOTEL sites indicated more seasonal snow accumulation and later snow-free dates for the recent (2008–2010) Landsat scenes relative to the older (1987–1988) Landsat scenes, although we still tried to ensure that scenes used for comparison contained minimal seasonal snow cover. For each region, we selected Landsat TM images from 1987 or 1988 and from 2008, 2009, or 2010 and used a more conventional, semi-automated approach to map the extent of PISC for each period.

Each scene selected for analysis of changes in PISC over time was acquired between September 1 and October 1. PISC for each scene was initially mapped by classifying pixels with NDSI >0.4 as PISC, applying a 5×5 median filter to reduce spatial noise and eliminate areas of patchy seasonal snow cover, and then applying a sieve to eliminate PISC patches of <25 contiguous pixels. We then edited the resulting PISC layer by adding areas of PISC in shadow not initially mapped as PISC and eliminating misclassified patches of PISC. In cases where a patch of ice or perennial snow cover appeared in one date of imagery but did not exceed the 25 contiguous pixel size threshold in the other (usually more recent) date of imagery, we digitized the outline of the remaining snow patch. This was done to ensure that small decreases in the size of a perennial snow or ice patch would not translate into overestimates of change when small patches of ice or perennial snow cover did not actually disappear but were not mapped due to the 25 contiguous pixels requirement.

We calculated total PISC area for 1987–1988 and for 2008–2010 for each of the three change assessment regions and then compared PISC area for both periods to PISC area calculated from the USGS DRG dataset and from the 2010–2014 Landsat-derived dataset.

3. Results

3.1. Accuracy assessment

For all 13 3×3 km VHRI validation subsets, accuracy and F were higher for the Landsat-derived PISC dataset than for the USGS DRG dataset or the NLCD land cover classification (Table 1). Mean F for the Landsat-derived PISC dataset that incorporated ancillary data was 0.848, a major improvement over both the USGS DRG and the NLCD 2011 datasets, with F scores of 0.676 and 0.758 respectively (see Fig. 6).

PISC maps from the USGS DRG, the NLCD, the automated Landsat, and the revised automated Landsat approach incorporating ancillary data are shown for the Mammoth Glacier subset in Wyoming in Fig. 5.

We observed a weak negative relationship between the fraction of a validation subset containing PISC and overall accuracy as well as a much more pronounced positive relationship between the fraction of a subset containing PISC and F (Fig. 7).

Accuracy assessment metrics for the set of 1000 randomly selected validation points also indicate the automated Landsat approach incorporating ancillary data provides a more accurate depiction of PISC across the western U.S. than the USGS DRG dataset or the NLCD dataset. Accuracy, precision, recall, and F metrics for both the full set of 1000 points and the subset of 834 non-edge points are shown in Fig. 8. The difference in accuracy between the Landsat PISC dataset and the USGS DRG PISC dataset is primarily due to the higher precision (user's accuracy for the PISC class) achieved by the automated Landsat mapping approach. This is not surprising, given that PISC has been demonstrated to have declined in area across much of the western U.S. between the time of acquisition for the aerial photographs used for the original USGS maps and the 2010–2014 period. Pixels covered by PISC at the time of acquisition for the aerial photographs (generally between 1960 and 1987) but free of PISC during the 2010–2014 period will often be labeled as true negatives for the automated Landsat datasets but labeled as false positives for the USGS DRG dataset, even if they were mapped correctly at the time. On the other hand, recall (producer's accuracy for PISC class) metrics are nearly the same for the USGS DRG dataset and the automated Landsat datasets. This is also not surprising, as we would expect little difference in recall metrics between the datasets if both mapping approaches have similar accuracy, assuming that the majority of pixels with PISC cover in 2010–2014 were also covered by PISC several decades earlier when the aerial photographs were acquired (see Table 2).

Table 1
F metric for USGS Topographic Maps glacier layer, NLCD 2011 perennial snow and ice cover, initial Landsat-derived PISC, and revised Landsat-derived PISC. Revised Landsat-derived PISC includes revisions based on ancillary data.

Subset name	USGS topo maps	NLCD 2011	Initial landsat-derived PISC	Revised landsat-derived PISC
Mt. Baker Summit	0.951	0.939	0.957	0.963
Mount Baker SW	0.910	0.837	0.931	0.940
Mount Baker NE	0.894	0.830	0.889	0.909
Redoubt Glacier West	0.840	0.747	0.862	0.880
Redoubt Glacier East	0.783	0.636	0.831	0.824
Goat Rocks West	0.611	0.384	0.770	0.768
Goat Rocks East	0.680	0.515	0.768	0.782
Harrison Glacier	0.813	0.762	0.835	0.857
Blackfoot Pumpelly Glaciers	0.826	0.770	0.891	0.892
Gannett Glacier	0.816	0.675	0.864	0.879
Mammoth Glacier	0.799	0.694	0.868	0.888
Lyell Glacier	0.503	0.491	0.701	0.700
Mount Ritter	0.430	0.502	0.701	0.736
All Subsets	0.758	0.676	0.836	0.848

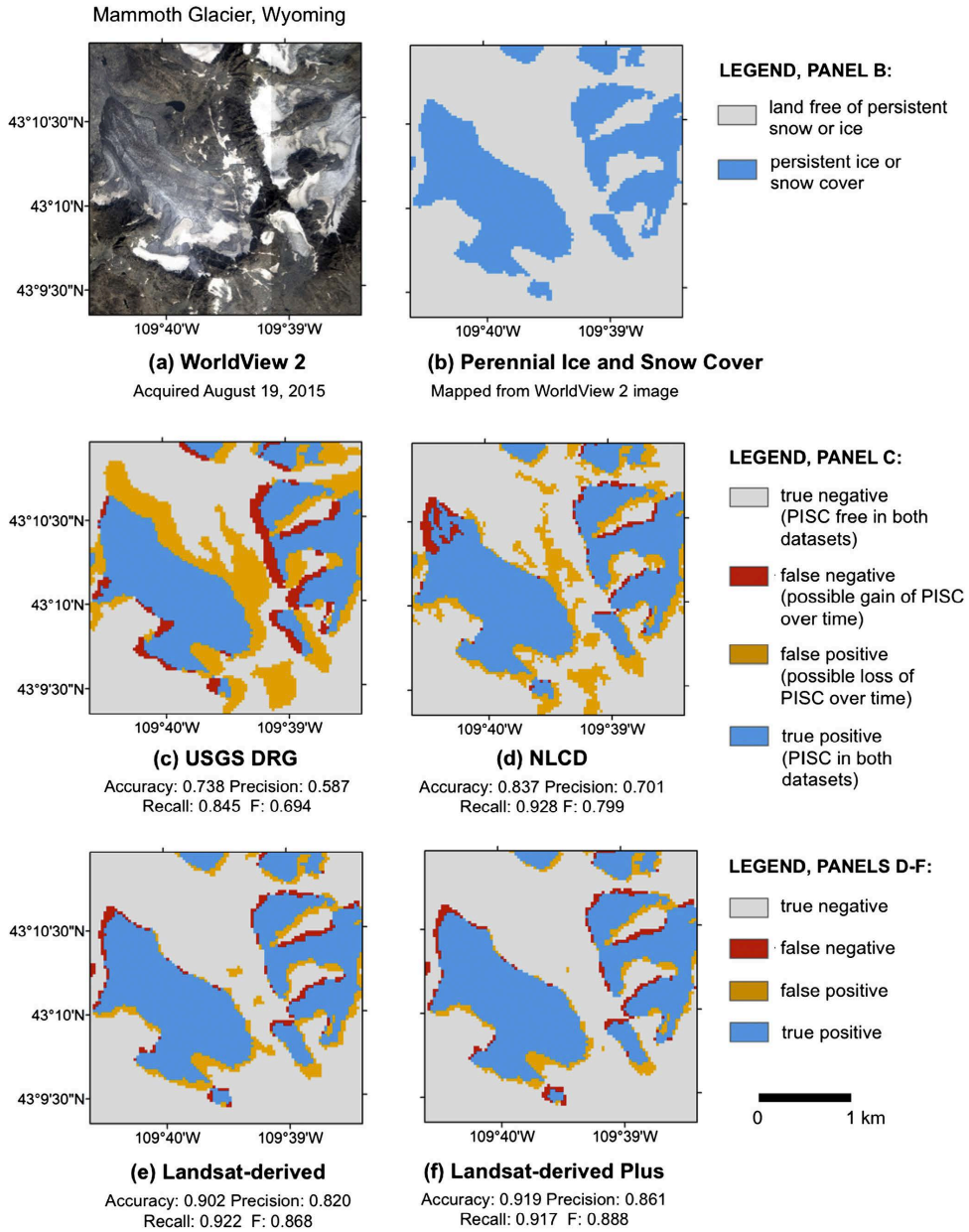

Fig. 5. Agreement between PISC mapped using late summer WorldView 2 imagery and PISC datasets for the Mammoth Glacier (Wyoming) VHRI subset. (a) WorldView 2 imagery, (b) PISC mapped from WorldView 2 imagery, (c) agreement between WorldView 2 PISC and USGS DRG PISC, (d) agreement between NLCD PISC and WorldView 2 PISC, (e) agreement between Landsat-derived PISC and WorldView 2 PISC, and (f) agreement between Landsat-derived plus ancillary data PISC and WorldView 2 PISC.

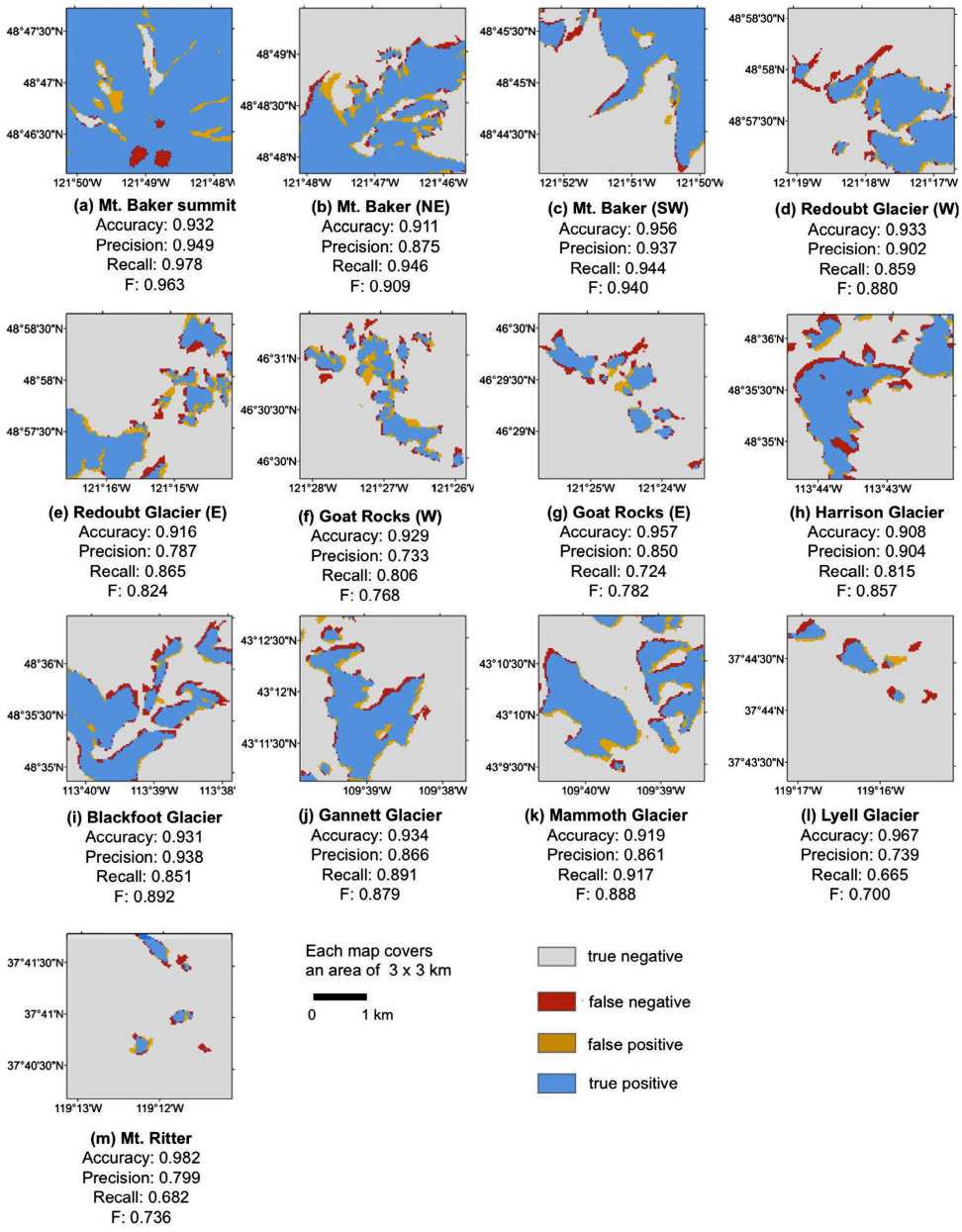

Fig. 6. Agreement between PISC mapped using late summer WorldView 2 imagery and PISC mapped by the automated Landsat approach plus ancillary data for all 13 VHRI subsets. (a) Mt. Baker (summit), (b) Mt. Baker (northeast), (c) Mt. Baker (southwest), (d) Redoubt Glacier (west), (e) Redoubt Glacier (east), (f) Goat Rocks (west), (g) Goat Rocks (east), (h) Harrison Glacier, (i) Blackfoot Glacier, (j) Gannet Glacier, (k) Mammoth Glacier, (l) Lyell Glacier, and (m) Mt. Ritter.

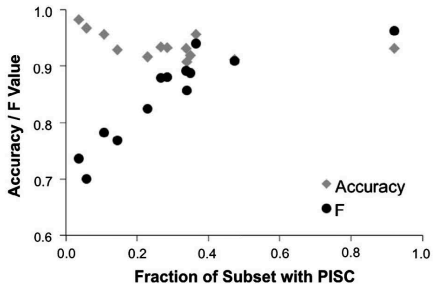

Fig. 7. Relationship between fraction of validation subset with PISC and Accuracy and F metrics.

3.1.1. Effect of number of cloud-free, shadow-free views on mapping accuracy

The relationship between the number of available cloud-free, shadow-free views of the land surface and the F metric is shown in Fig. 9. The data indicate that while accuracy is typically poor when <3 cloud-free, shadow-free views are available, 3 views appears to be sufficient for accurate mapping, as no increase in F is associated with increased cloud-free, shadow-free views beyond this point. The small decrease in F that occurs as the number of cloud-free views exceeds 8 is likely due to the geographic distribution of pixels in the dataset with >8 cloud free views. The vast majority of these pixels are from the two subsets in the Sierra Nevada, where more cloud-free views were available than in other regions, and where the automated Landsat approach performed relatively poorly compared to its performance in other regions.

3.2. Glacier area mapped by different datasets

The USGS DRG dataset maps a total of 575.9 km^2 of PISC, while the automated Landsat approach maps 28% less PISC for a total of 412.3 km^2. The NLCD 2011 dataset maps a total of 1243.4 km^2. Fig. 10 and Table 3 report the total area of PISC mapped by each dataset within each region. In most regions, the automated Landsat approach indicated a much smaller total area of PISC than either the USGS DRG dataset or the NLCD dataset. The largest difference between the DRG dataset and the automated Landsat dataset is in the northern Cascades of Washington, where the automated Landsat approach mapped 51.9 km^2 less PISC than the USGS DRG dataset, which equates to a 21% difference between the two datasets. The largest differences by percentage are observed in the Colorado Rocky Mountains, where 82% less PISC was mapped by the automated Landsat approach, and in the Sierra Nevada, where 74% less PISC was mapped by the automated Landsat approach. While the relative differences for these regions are large, the actual difference in PISC area mapped is relatively small, as both the Colorado Rocky Mountains and the Sierra Nevada never had substantial PISC area to begin with. For regions with more substantial PISC, the largest differences by percentage are found in the Southwest Montana/Northwest Wyoming region, where 54% less PISC was mapped by the automated Landsat approach, and in the Northwest Montana region, where 37% less PISC was mapped by the automated Landsat approach.

3.3. Comparison to traditional mapping approaches for selected study areas

Results from the conventional change detection using the semi-automated Landsat mapping approach demonstrate substantial decreases in PISC between 1987–1988 and 2008–2010 (Table 4). The decrease in PISC between 1987–1988 and 2008–2010 for the three test regions correlates closely with the difference between PISC mapped by the USGS DRG dataset and PISC mapped by the automated Landsat approach. This strongly suggests that much of the difference between the PISC area mapped in the USGS DRG dataset and the PISC area mapped by the automated Landsat approach can be attributed to decreases in PISC area over time rather than differences in mapping methods.

4. Discussion

Results from two independent validation approaches indicate that the automated Landsat dataset provides the most accurate representation of contemporary PISC for the entire conterminous Western U.S.

The positive relationship between the fraction of a subset with PISC and F (perhaps the most useful validation metric) indicates that the automated approach presented here should work well for the region's medium and larger glaciers. We anticipate the approach will not be as effective, however, for mapping the region's smallest glaciers and perennial snow cover patches. Many of these cover <25 contiguous Landsat pixels and would be eliminated by the minimum size threshold in our approach. In addition, the smallest glaciers are often remnants of larger glaciers that have retreated into protected north-facing cirques where consistent shadowing may reduce the odds of PISC detection.

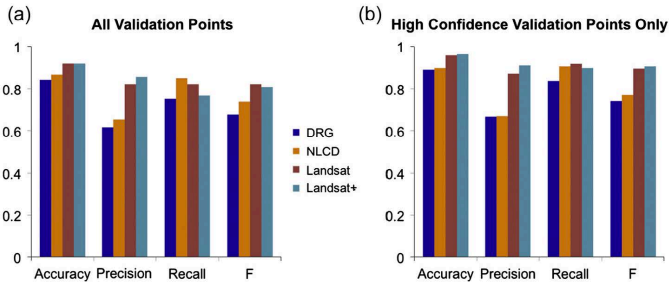

Fig. 8. Accuracy, precision, recall, and F metrics for 1000 points randomly selected from areas on or near (within 500 m) of previously mapped glaciers and perennial snow cover patches. (a) all 1000 points, and (b) High confidence validation points (the subset of 834 points located >30 m from the edge (either on or off) of glacier or perennial snow cover).

Table 2
Accuracy, precision, recall and F metrics for 1000 randomly selected validation points.

Dataset	Full dataset				Non-edge points subset			
	Accuracy	Precision	Recall	F	Accuracy	Precision	Recall	F
USGS DRG	0.843	0.615	0.753	0.677	0.891	0.668	0.836	0.743
NLCD								
Landsat	0.922	0.822	0.822	0.822	0.960	0.874	0.918	0.895
Landsat + ancillary data	0.921	0.857	0.767	0.810	0.964	0.911	0.899	0.905

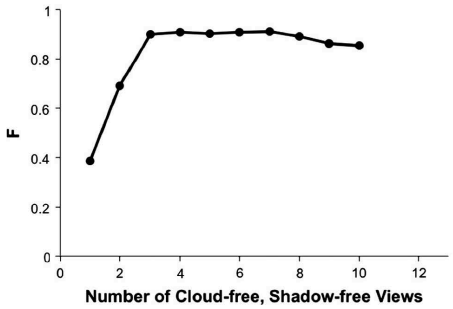

Fig. 9. Relationship between the number of cloud-free, shadow-free views and F metric for all pixels from VHRI validation subsets.

Accurate mapping of PISC extent in consistently terrain-shadowed locations remains a challenge for optical remote sensing efforts. At the latitude of the western conterminous U.S. (~30°–49°N) consistently terrain-shadowed pixels covered only a small fraction of the landscape (2.2% for pixels with no cloud-free, shadow-free views, and an additional 2.5% for pixels with only one cloud-free, shadow-free land surface view). Nevertheless, for these pixels, accuracy can be lower, with both false positive and false negatives relatively common. False positives can sometimes occur in terrain-shadowed areas where seasonal snow cover remains into the late summer. This is because terrain shadowing at these locations does not occur during the earlier part of the August 20–September 30 period (when snow is still present), but does occur (due to increasing solar zenith angles) at the end of the period (e.g. September 15–30), when the seasonal snow has finally melted. As a result, all shadow-free land surface views at these locations indicate snow, with no usable land surface views available during the very brief snow-free period. Conversely, false

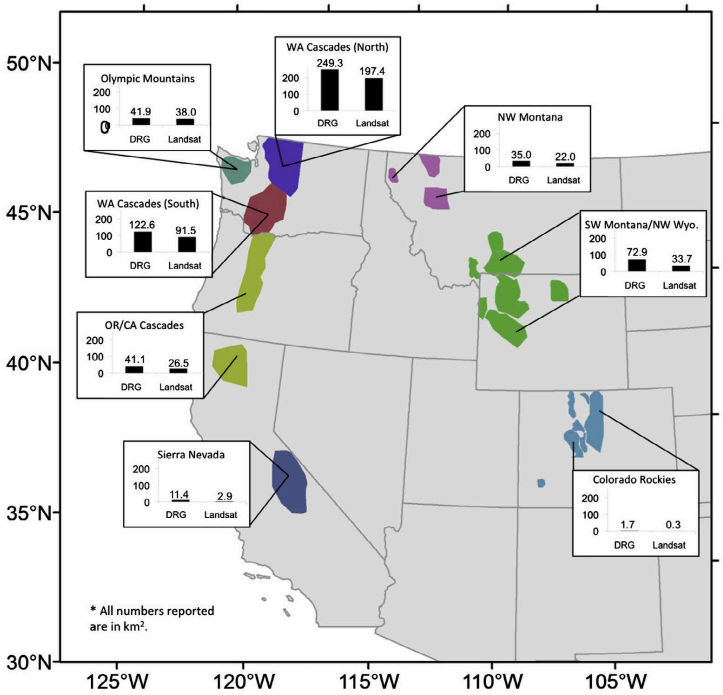

Fig. 10. Area of PISC mapped by the USGS DRG dataset and by the automated Landsat-derived dataset for 8 regions in the western U.S.

Table 3
Area of PISC mapped by the USGS DRG dataset, the automated Landsat dataset, and the NLCD 2011 dataset by region.

Region	USGS DRG PISC area	Automated landsat PISC area	NLCD 2011	Percent difference (DRG vs landsat) (%)
N Washington Cascades	249.3	197.4	243.2	21
Olympic Mountains	41.9	38.0	142.3	9
S Washington Cascades	122.6	91.5	143.8	25
Oregon/California Cascades	41.1	26.5	37.4	36
Sierra Nevada	11.4	2.9	15.2	74
NW Montana	35.0	22.0	47.4	37
SW Montana/NW Wyoming	72.9	33.7	83.0	54
Colorado Rocky Mountains	1.7	0.3	531.1	82
Western US Total	575.9	412.3	1243.4	28

Table 4
PISC area mapped by semi-automated Landsat approach for 1987–1988 and 2008–2010 for three test regions.

Region	USGS DRG 1960s–1980s	Automated landsat 2010–2014	Difference (relative to DRG area) (%)	Semi-automated landsat 1987–1988	Semi-automated landsat 2008–2010	Difference (relative to DRG area) (%)
Olympic Mountains	35.8	33.8	−5.6	34.2	32.0	−6.6
Sierra Nevada	2.2	1.1	−50.0	3.0	1.6	−46.7
Wind River Mountains	44.9	26.8	−40.3	45.7	29.8	−34.8

negatives can occur at locations that are perpetually shadowed from August 20–September 30 at the time of Landsat scene acquisition, as pixels with no cloud-free, shadow-free land surface views are automatically flagged as PISC-free in our approach.

The automated Landsat approach using scenes from the 2010–2014 period maps 28% less PISC area than the USGS DRG dataset, which is based on aerial photography acquired during the 1960s, 1970s, and 1980s. The difference between PISC mapped by the two datasets, however, varies substantially between regions, from as little as 9% difference in the Olympic Mountains to as much as 82% difference in the Colorado Rocky Mountains.

Results from the more conventional change detection approach employed for test areas in the Olympic Mountains, Sierra Nevada, and Wind River Mountains indicate that a substantial fraction of PISC present in the 1987–1988 period had disappeared by the 2008–2010 period in the Wind River Mountains (loss of 15.9 km^2 or 34.8%) and in the Sierra Nevada (loss of 1.4 km^2 or 46.7%). In the Olympic Mountains, only 6.6% of total PISC disappeared during this period. Both the absolute and relative amounts of PISC lost at each of these three study areas correlate closely with the differences between the USGS DRG dataset and the automated Landsat dataset. This strongly suggests that a large fraction of the difference in PISC mapped by the USGS DRG dataset and the automated Landsat dataset can be attributed to decreases in PISC over time, rather than differences in methods between the mapping approaches.

Results from several other studies monitoring changes in glacier area over time in the western U.S. also indicate substantial reductions in glacier area, providing further evidence that much of the difference between PISC mapped by the USGS DRG dataset and PISC mapped by the automated Landsat approach can be attributed to changes in PISC area rather than differences between mapping approaches. The 54% difference in PISC area in the Wind River Range is similar to the 39% reduction in ice area observed by Maloof et al. (2014) between 1967 and 2006, and it is not unreasonable to expect that substantial additional ice loss may have occurred after 2006. While the 21% difference in PISC mapped in the North Cascades is substantially more than the 7% reduction observed by Granshaw and Fountain (2006) between 1958 and 1998 in this region, ice loss has continued at a rapid rate since 1998 in the North Cascades (Pelto and Brown, 2012). Finally, the 37% difference in PISC area in Northwest Montana between the two datasets is only slightly greater than the 29% loss of ice between 1966 and 2005 reported by the USGS (2013).

It is important to note that, aside from the inclusion of perennial snow cover and most likely some seasonal snow cover (Fountain et al., 2007), the USGS DRG dataset is essentially a conventional glacier inventory and has been included in the Randolph Glacier Inventory (Pfeffer et al., 2014) and the Global Land Ice Measurements from Space (GLIMS) datasets (Bishop et al., 2004), along with other similar inventories from locations around the world. The automated Landsat-derived dataset, on the other hand, is a binary raster dataset that maps the presence or absence of PISC at 30 m resolution and does not provide any of the attribute information often included in glacier inventories for each individual glacier or perennial snow cover patch, such as size, mean elevation, or aspect. However, an object-based image segmentation approach where snow and ice cover persistence forms the basis for object delineation such as the approach introduced by Thompson and Lees (2014) could facilitate the conversion of a binary raster PISC dataset into a vector dataset of probable glacier outlines. This would allow for the calculation of attribute information for each polygon. It is likely, however, that a substantial amount of editing would be required to bring the resulting vector dataset up to the standards of a conventional glacier inventory.

Despite the limitations described above, the 2010–2014 Landsat-derived PISC dataset for the conterminous western U.S. provides a valuable update to the original USGS DRG dataset and also provides a more accurate representation of PISC than the NLCD 2011 classification. We caution against interpreting differences in area mapped by the Landsat-derived dataset and the USGS DRG dataset as precise estimates of change in PISC area because the original DRG dataset is based on a wide range of years and was created using a different approach. Nevertheless, differences between the USGS DRG dataset and the 2010–2014 Landsat-derived dataset do highlight areas in the region that have experienced the greatest and least amount of changes in PISC over the past 30–50 years. The greatest strength of the dataset and automated mapping approach presented here is that it can be updated with relative ease as new imagery, including imagery from Landsat 8's OLI sensor, becomes available and as additional changes in PISC continue to occur across the region.

5. Conclusions

We implemented a fully automated approach for mapping perennial ice and snow cover across the western conterminous U.S. using Landsat TM and ETM+ imagery acquired between August 20 and September 30 for the years 2010–2014. Accuracy assessment of this dataset using two different validation approaches indicates that the 2010–2014 Landsat-derived dataset is substantially more accurate than both the USGS DRG glacier dataset (based on aerial photography from the 1960s, 1970s, and 1980s) and the National Land Cover Database land cover classification perennial snow and ice class. Analysis of change in PISC area between 1987–1988 and 2008–2010 using a more traditional semi-automated Landsat-derived mapping approach for each period indicates substantial loss of PISC and suggests that differences between PISC mapped by the USGS DRG dataset and PISC mapped by the automated Landsat approach are due primarily to decreases in PISC area, rather than differences between mapping approaches. Our 2010–2014 Landsat-derived PISC dataset indicates that as much as 28% of PISC has been lost across the western U.S. since the original USGS maps were developed. In some regions with substantial PISC, loss of PISC may be as much as 54%, and in regions with smaller total PISC area, loss of PISC may be as high as 82%. While our updated Landsat-derived PISC dataset is not designed to serve as a standard glacier inventory, it identifies areas where major changes in PISC have occurred since the original USGS maps were developed, highlighting the need for a regularly updated PISC inventory across the region.

Acknowledgements

Mention of a particular product does not constitute endorsement by the U.S. federal government. The feedback we received from Dennis Dye of the USGS as well as two anonymous reviewers resulted in substantial improvements to the manuscript. Funding for this research was provided by the Land Remote Sensing Program of the Climate and Land Use Change Mission Area of the US Geological Survey.

References

Aniya, M., Sato, H., Naruse, R., Skvarca, P., Casassa, G., 1996. The use of satellite and airborne imagery to inventory outlet glaciers of the Southern Patagonia Icefield, South America. Photogram. Eng. Remote Sens. 62, 1361–1369.
Barnett, T.P., Adam, J.C., Lettenmaier, D.P., 2005. Potential impacts of a warming climate on water availability in snow-dominated regions. Nature 438, 303–309.
Basagic, H.J., Fountain, A., 2011. Quantifying 20th century glacier change in the Sierra Nevada, California. Arct. Antarct. Alp. Res. 43, 317–330.
Bernard, É., Friedt, J.M., Tolle, F., Griselin, M., Martin, G., Laffly, D., Marlin, C., 2013. Monitoring seasonal snow dynamics using ground based high resolution photography (Austre Lovénbreen, Svalbard, 79° N). ISPRS J. Photogram. Remote Sens. 75, 92–100.
Bishop, M.P., Olsenholler, J.A., Shroder, J.F., Barry, R.G., Raup, B.H., Bush, A.B.G., Copland, L., Dwyer, J.L., Fountain, A.G., Haeberli, W., Kääb, A., Paul, F., Hall, D.K., Kargel, J.S., Molnia, B.F., Trabant, D.C., Wessels, R., 2004. Global land ice measurements from space (GLIMS): REMOTE SENSING AND GIS INVESTIGATIONS OF THE EARTH'S CRYOSPHERE. Geocarto Int. 19, 57–84.
Bolch, T., Menounos, B., Wheate, R., 2010. Landsat-based inventory of glaciers in western Canada, 1985–2005. Remote Sens. Environ. 114, 127–137.
DeVisser, M.H., Fountain, A.G., 2015. A century of glacier change in the Wind River Range, WY. Geomorphology 232, 103–116.
Dozier, J., 1989. Spectral signature of alpine snow cover from the Landsat Thematic Mapper. Remote Sens. Environ. 28, 9–22.
Dyurgerov, M.B., Meier, M.F., 2000. Twentieth century climate change: evidence from small glaciers. Proc. Natl. Acad. Sci. 97, 1406–1411.
Edmunds, J., Tootle, G., Kerr, G., Sivanpillai, R., Pochop, L., 2012. Glacier variability (1967–2006) in the Teton range, Wyoming, United States1. JAWRA J. Am. Water Resources Assoc. 48, 187–196.
Farinotti, D., Magnusson, J., Huss, M., Bauder, A., 2010. Snow accumulation distribution inferred from time-lapse photography and simple modelling. J. Geophys. Res., F010114
Fountain, A.G., Hoffman, M., Jackson, K., Basagic, H., Nylen, T., Percy, D., 2007. Digital Outlines and Topography of the Glaciers of the American West. US Geological Survey Open File Report 2006-1340.
Gesch, D., Oimoen, M., Greenlee, S., Nelson, C., Steuck, M., Tyler, D., 2002. The national elevation dataset. Photogram. Eng. Remote Sens. 68, 5–32.
Granshaw, F.D., Fountain, A.G., 2006. Glacier change (1958–1998) in the north Cascades national park complex, Washington, USA. J. Glaciol. 52, 251–256.
Guo, W., Liu, S., Xu, J., Wu, L., Shangguan, D., Yao, X., Wei, J., Bao, W., Yu, P., Liu, Q., Jiang, Z., 2015. The second Chinese glacier inventory: data, methods and results. J. Glaciol. 61, 357.
Hall, D., Ormsby, J., Bindschadler, R., Siddalingaiah, H., 1987. Characterization of snow and ice reflectance zones on glaciers using Landsat Thematic Mapper data. Ann. Glaciol. 9, 104–108.
Hall, M.H., Fagre, D.B., 2003. Modeled climate-induced glacier change in Glacier National Park, 1850–2100. Bioscience 53, 131–140.
Immerzeel, W.W., Van Beek, L.P., Bierkens, M.F., 2010. Climate change will affect the Asian water towers. Science 328, 1382–1385.
ITT Visual Information Solutions, 2008. ENVI On-line Software User's Manual.
Jacobs, J.D., Simms, É.L., Simms, A., 1997. Recession of the southern part of Barnes Ice Cap, Baffin Island, Canada, between 1961 and 1993, determined from digital mapping of Landsat TM. J. Glaciol. 43, 98–102.
Jin, S., Yang, L., Danielson, P., Homer, C., Fry, J., Xian, G., 2013. A comprehensive change detection method for updating the National Land Cover Database to circa 2011. Remote Sens. Environ. 132, 159–175.
Kääb, A., Reynolds, J.M., Haeberli, W., 2005. Glacier and permafrost hazards in high mountains. Global Change and Mountain Regions. Springer, pp. 225–234.
Kaser, G., Cogley, J.G., Dyurgerov, M.B., Meier, M.F., Ohmura, A., 2006. Mass balance of glaciers and ice caps: consensus estimates for 1961–2004. Geophys. Res. Lett. 33.
Lemke, P., Ren, J., Alley, R.B., Allison, I., Carrasco, J., Flato, G., Fujii, Y., Kaser, G., Mote, P., Thomas, R.H., 2007. Observations: changes in snow, ice and frozen ground. In: Climate Change 2007: The Physical Science Basis. Cambridge University Press, Cambridge, UK, and New York.
Macander, M.J., Swingley, C.S., Joly, K., Raynolds, M.K., 2015. Landsat-based snow persistence map for northwest Alaska. Remote Sens. Environ. 163, 23–31.
Maloof, A., Piburn, J., Tootle, G., Kerr, G., 2014. Recent alpine glacier variability: wind river range, wyoming, USA. Geosciences 4, 191–201.
Masek, J.G., Vermote, E.F., Saleous, N.E., Wolfe, R., Hall, F.G., Huemmrich, K.F., Gao, F., Kutler, J., Lim, T.-K., 2006. A Landsat surface reflectance dataset for North America, 1990–2000. Geosci. Remote Sens. Lett. IEEE 3, 68–72.
McCabe, G.J., Fountain, A.G., 2013. Glacier variability in the conterminous United States during the twentieth century. Climatic Change 116, 565–577.
McGurk, B.J., Painter, T.H., 2013. Airborne snow observatory: measuring basin-wide seasonal snowpack with LiDAR and an imaging spectrometer to improve runoff forecasting and reservoir operation. AGU Fall Meet. Abstracts, vol. 1, p. 01.
Moore, R., Fleming, S., Menounos, B., Wheate, R., Fountain, A., Stahl, K., Holm, K., Jakob, M., 2009. Glacier change in western North America: influences on hydrology, geomorphic hazards and water quality. Hydrol. Process. 23, 42.
Oerlemans, J., 2005. Extracting a climate signal from 169 glacier records. Science 308, 675–677.
Painter, T.H., Brodzik, M.J., Racoviteanu, A., Armstrong, R., 2012. Automated mapping of Earth's annual minimum exposed snow and ice with MODIS. Geophys. Res. Lett. 39.
Pelto, M., Brown, C., 2012. Mass balance loss of Mount Baker, Washington glaciers 1990–2010. Hydrol. Process. 26, 2601–2607.
Pfeffer, W.T., Arendt, A.A., Bliss, A., Bolch, T., Cogley, J.G., Gardner, A.S., Hagen, J.-O., Hock, R., Kaser, G., Kienholz, C., Miles, E.S., Moholdt, G., Mölg, N., Paul, F., Radić, V., Rastner, P., Raup, B.H., Rich, J., Sharp, M.J., 2014. The Randolph Glacier Inventory: a globally complete inventory of glaciers. J. Glaciol. 60, 537–552.
Rastner, P., Bolch, T., Mölg, N., Machguth, H., Le Bris, R., Paul, F., 2012. The first complete inventory of the local glaciers and ice caps on Greenland. Cryosphere 6, 1483–1495.
Richardson, S.D., Reynolds, J.M., 2000. An overview of glacial hazards in the Himalayas. Quatern. Int. 65, 31–47.
Riggs, G., Hall, D.K., Salomonson, V.V., 1994. A snow index for the Landsat thematic mapper and moderate resolution imaging spectroradiometer. In: Geoscience and Remote Sensing Symposium, 1994. IGARSS'94. Surface and Atmospheric Remote Sensing: Technologies, Data Analysis and Interpretation., International. IEEE, pp. 1942–1944.
Rittger, K., Painter, T.H., Dozier, J., 2013. Assessment of methods for mapping snow cover from MODIS. Adv. Water Resour. 51, 367–380.
Selkowitz, D.J., Forster, R.R., 2015. An automated approach for mapping persistent ice and snow cover over high latitude regions. Remote Sens. 8, 16.
Sitts, D.J., Fountain, A.G., Hoffman, M.J., 2010. Twentieth century glacier change on Mount Adams, Washington, USA. Northwest Sci. 84, 378–385.
Stocker, T., Qin, D., Plattner, G.-K., Tignor, M., Allen, S.K., Boschung, J., Nauels, A., Xia, Y., Bex, V., Midgley, P.M., 2014. Climate Change 2013: The Physical Science Basis. Cambridge University Press, Cambridge, UK, and New York.
Thompson, J.A., Lees, B.G., 2014. Applying object-based segmentation in the temporal domain to characterise snow seasonality. ISPRS J. Photogram. Remote Sens. 97, 98–110.
Tulbure, M.G., Broich, M., 2013. Spatiotemporal dynamic of surface water bodies using Landsat time-series data from 1999 to 2011. ISPRS J. Photogram. Remote Sens. 79, 44–52.

Ventura, A.D., Rampini, A., Rabagliati, R., Barbero, R.S., 1987. Development of a satellite remote sensing technique for the study of alpine glaciers. Int. J. Remote Sens. 8, 203–215.
Zhang, L., Weng, Q., 2016. Annual dynamics of impervious surface in the Pearl River Delta, China, from 1988 to 2013, using time series Landsat imagery. ISPRS J. Photogram. Remote Sens. 113, 86–96.
Zhu, X., Liu, D., 2014. Accurate mapping of forest types using dense seasonal Landsat time-series. ISPRS J. Photogram. Remote Sens. 96, 1–11.
Zhu, Z., Woodcock, C.E., 2012. Object-based cloud and cloud shadow detection in Landsat imagery. Remote Sens. Environ. 118, 83–94.

CHAPTER 5

THE USGS LANDSAT SNOW COVERED AREA PRODUCTS: METHODS AND PRELIMINARY VALIDATION

David J. Selkowitz [1,2]

Thomas H. Painter[3]

Karl Rittger[4]

Gail Schmidt[5]

Richard Forster[2]

1 U.S. Geological Survey, Alaska Science Center

2 University of Utah, Department of Geography

3 NASA/Jet Propulsion Laboratory

4 National Snow and Ice Data Center, University of Colorado

5 Stinger Ghaffarian Technologies (SGT), Contractor to the U.S. Geological Survey (USGS)

5.1 Introduction

Seasonal snow cover is vitally important to Earth's climate, ecology, and hydrology. Streamflow is generated primarily by snow cover runoff in many regions, and approximately one sixth of the world's population depends on snow cover for their water supply (Barnett et al., 2005). The timing and duration of seasonal snow cover is one of the key drivers for both short term fluctuations and long term changes in Earth's albedo, and therefore impacts climate dynamics at the global scale (Cohen & Entekhabi, 1999; Groisman et al., 1994). Snow cover insulates soil from cold winter temperatures (Groffman et al., 2001; Zhang, 2005) but can also inhibit thawing when air temperatures rise above the freezing point in the spring, thus altering drainage characteristics (Quinton et al., 2009). The duration of seasonal snow cover is often the dominant factor controlling the distribution of arctic and alpine plant species (Billings & Bliss, 1959; Walker et al., 1993) and can also impact the configuration of forests and meadows at the alpine treeline and below (Bekker, 2005; Hessl & Baker, 1997; Magee & Antos, 1992). Snow cover also impacts animal movement and habitat distribution (Aubry et al., 2007; Stenseth et al., 2004; Sweeney & Sweeney, 1984). The influence of snow cover on all of these crucial hydrological, climatological, and ecological processes underscores the importance of monitoring the spatial and temporal variability of snow cover across the Earth's surface at a variety of scales.

Remote sensing is one of the most effective approaches for regular, spatially comprehensive snow cover monitoring. For many applications, the fine to moderate scale (10 m to 1 km) spatial distribution of snow cover is important for

understanding scales of controls and spatial variability (Deems et al., 2006; Tinkham et al., 2014). Several studies (Anderton et al., 2002; Luce & Tarboton, 1998) have demonstrated that in areas where heterogeneous seasonal snow covers develop, explicit representation of the spatial variability of snow cover is essential for accurate simulation of snowmelt runoff unless these parameters can be effectively accounted for in subgrid parameterization schemes. For snow simulation models, fine to moderate resolution snow cover patterns retrieved from remote sensing also provide an additional source of validation data besides runoff. Unlike runoff, however, remotely sensed snow covered area (SCA) at fine to moderate spatial resolutions can be used to assess the representation of individual processes in the model (e.g., wind redistribution of snow cover) (Bloschl et al., 1991). Lundquist and Dettinger (2005) demonstrate that the spatial heterogeneity of snow cover plays a key role in determining diurnal streamflow variations in larger basins. In colder climates, hillslope drainage is largely controlled by fine scale patterns of snow covered area because high latitude soils overlain by snow cover typically remain frozen and inhibit subsurface flow (Quinton et al., 2009). Finally, fine to moderate scale heterogeneity of snow cover controls the distribution and abundance of many plant species in arctic and alpine environments (Beck et al., 2005; Billings & Bliss, 1959; Walker et al., 1993), influences animal habitat selection (Eastland et al., 1989; LaPerriere & Lent, 1977), and impacts predator prey interactions (Huggard, 1993).

The availability of standardized, freely distributed SCA products derived from the Moderate Resolution Imaging Spectroradiometer (MODIS) has vastly

improved our ability to monitor and understand regional to global scale SCA patterns and variability. Remotely sensed SCA from the Landsat TM, ETM+, and OLI sensors, however, offers tremendous potential for extending this monitoring to a finer spatial scale. Landsat sensors are well suited for mapping SCA at 30 m spatial resolution. This has been demonstrated in numerous studies where Landsat data were used for snow cover mapping prior to the availability of MODIS data (Bronge† & Bronge†*, 1999; Dozier, 1984; Fily et al., 1997; Hall et al., 1989; Klein & Isacks, 1999; Rosenthal & Dozier, 1996; Winther & Hall, 1999), to assist with development and validation of MODIS snow algorithms (Hall et al., 1995; Klein et al., 1998; Painter et al., 2009; Rittger et al., 2013; Salomonson & Appel, 2004), for validation of spatially explicit snow cover models (Bernhardt et al., 2010; Bernhardt & Schulz, 2010; Fily et al., 1999; Letsinger & Olyphant, 2007), and for reconstruction of peak snow water equivalent (Cline et al., 1998; Durand et al., 2008; Margulis et al., 2016; Martinec & Rango, 1981; Molotch, 2009).

Effective, snow cover remote sensing across most regions requires an approach that can reliably detect snow cover beneath forest canopies. Optical remote sensing approaches, however, typically map the viewable fraction of snow cover not obscured by forest canopy, rather than the true fraction of snow covering the ground. Although a number of algorithms have been developed with the aim of monitoring ground snow cover fraction via optical remote sensing (Klein, Hall & Riggs, 1998; Moloch & Margulis, 2008; Vikhamar & Solberg, 2003), this problem remains an active area of research.

The most commonly used approach for adjusting sensor-viewable fSCA to reflect the true in situ fSCA in areas with forest canopy is to assume that the viewable snow cover fraction for a given pixel will be identical (or at least similar) to the hidden (canopy-obscured) snow cover fraction for the same pixel (Coons et al., 2014; Durand & Molotch, 2008; Molotch & Margulis, 2008; Raleigh et al., 2013). Approaches assuming similar snow cover fractions for the canopy-obscured and canopy-free portions of a pixel are usually reasonably accurate as long as a snow cover fraction > 0 is retrieved at each snow covered pixel. They are, however, ineffective for identifying snow-covered pixels where the viewable snow cover fraction is less than the snow cover detection limit for the snow mapping algorithm.. There is therefore a need for a canopy adjustment approach that can identify snow cover that is frequently missed by optical remote sensing approaches.

Snow covered area is the most basic measurement that can be made from optical remote sensing and serves as a key input for remote sensing or combined remote sensing/modeling approaches that endeavor to provide more complex snow metrics such as SWE. Fractional snow covered area (fSCA) provides more information per-pixel than binary SCA and is particularly useful in mountainous environments where 25-93% of all pixels at the Landsat spatial resolution are mixed pixels composed of two or more land surface types (Selkowitz et al., 2014). In order to meet the need for a standardized, analysis-ready Landsat snow cover dataset, the US Geological Survey is now producing a Landsat scene-based snow cover product based on Painter et al. (2009) that provides 30 m resolution fSCA, canopy-adjusted fSCA, and a cloud mask optimized for use in mountainous

environments. The first iteration of the scene-based Landsat snow cover product is available on demand for nearly any Landsat TM or ETM+ scene available in the archives stretching back to 1984.

For users more interested in characterizing patterns of snow cover duration and potential changes in snow and ice cover over decades, the Landsat snow cover duration product will provide the mean annual snow cover duration days at 30 m resolution for periods as short as 5 years and as long as the full Landsat 5/Landsat 7 period of record (1984 to the present). The snow cover duration product will incorporate canopy-adjusted fSCA and cloud mask data from the Landsat scene-based snow products covering the period of interest. Initial production of the snow cover duration product will focus on 30-year mean annual snow cover duration across key mountain ranges in the western U.S., with areas outside of the region available upon request.

The goals of this publication are: (1) to provide a detailed description of the methods used for production of both the scene-based fSCA and mean annual snow cover duration products, and (2) provide limited validation for each of the two products.

5.2. Study Area and Methods

5.2.1 Study Area Locations

Validation of fSCA from individual Landsat scenes was conducted using in situ sensor arrays in the Sierra Nevada at sites covered by Landsat path rows 43/33, 43/34, 42/34, 42/35, and 41/35, while validation of mean annual snow cover

duration was conducted using SNOTEL sites in the Cascades of Washington and Oregon (path rows 45/27 and 45/28), the Sierra Nevada of California (path row 43/33), and the Rocky Mountains of Wyoming, Montana, and Idaho (path rows 38/29 and 38/30) (Figure 5.1, Table 5.1). Detailed analysis of the mean annual snow cover duration products was also conducted at one 30 x 30 km subset from each of the three regions (Figure 5.1, Table 5.2). The three regions were selected to represent the variation in snow climate regimes (Mock & Birkeland, 2000; Trujillo & Molotch, 2014) and vegetation types present across the western U.S.

5.2.2 Overview of Methods

We retrieved the visible snow cover fraction for each 30 m Landsat pixel using the TMSCAG (Thematic Mapper Snow Covered Area and Grain Size) model (Painter et al., 2003; Painter et al., in review), a spectral unmixing approach. We then applied a series of adjustments (Figure 5.2) designed to produce fSCA values that more closely matched the fraction of snow covered ground (including rock, soil, low-growing vegetation, and woody debris) in areas with forest canopy. The first adjustment handled pixels where retrieved fSCA was > 0 but likely underrepresented the fraction of snow covered ground. The second adjustment handled pixels where retrieved fSCA was 0 but a combination of ancillary data and retrieved viewable fSCA from nearby pixels suggested snow cover was likely present. Finally, cloud cover was identified and masked using the revised CFMask approach described in Selkowitz and Forster (2015). These steps resulted in three layers: (1) viewable fSCA (computed directly from TMSCAG), (2) canopy-adjusted

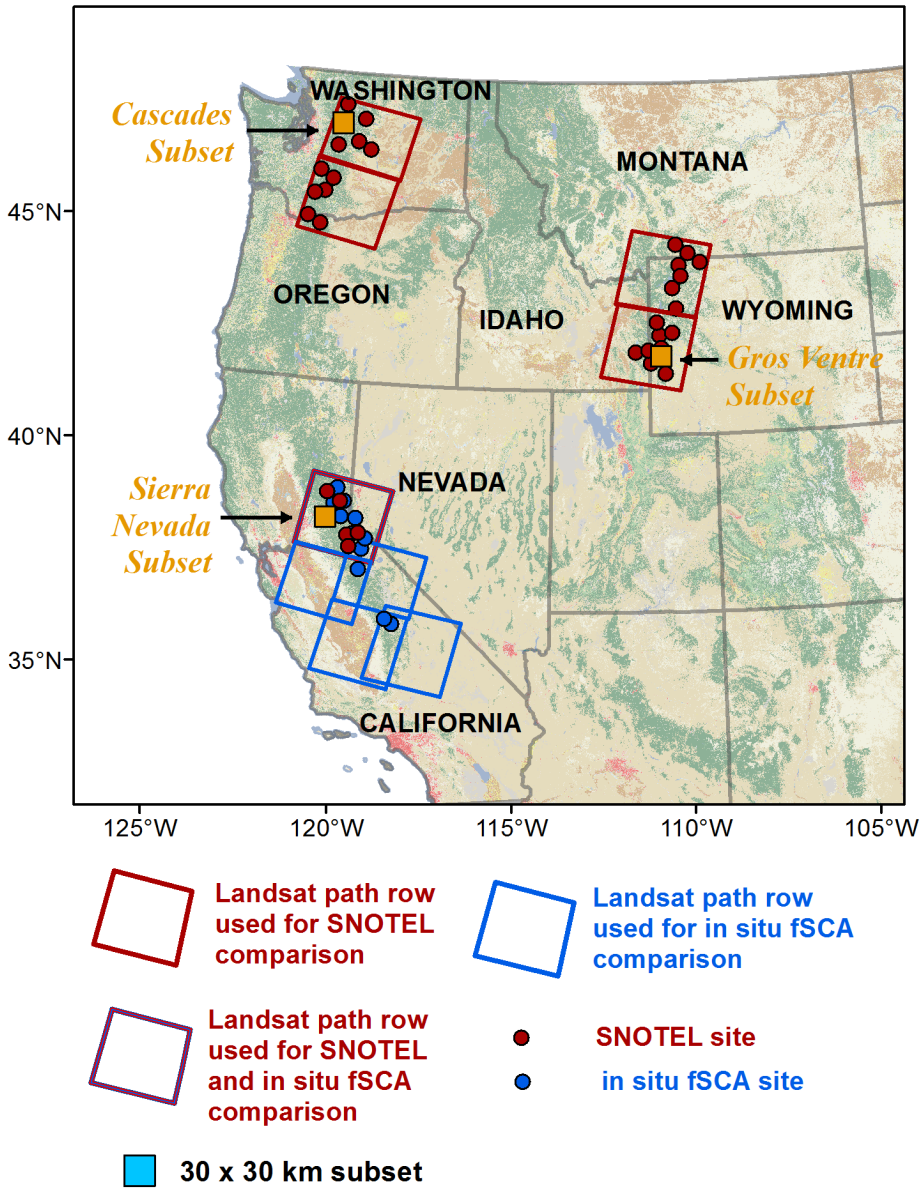

Figure 5.1. Study area locations in the western U.S, including Landsat path/rows used, 30 x 30 km analysis subsets, locations of SNOTEL sites used, and locations of in situ fSCA sites.

Table 5.1. Landsat scenes used by path row.

Landsat Path/Row	Type(s) of Analysis	Scenes		
		TM	ETM+	Total
45/27	SNOTEL comparison, Cascades subset analysis	370	494	864
45/28	SNOTEL comparison	369	502	871
43/33	In situ sensor array comparison, SNOTEL comparison, Sierra subset analysis	370	511	881
43/34	In situ sensor array comparison	5		5
42/34	In situ sensor array comparison	8		8
42/35	In situ sensor array comparison	7		7
41/35	In situ sensor array	7		7
38/29	SNOTEL comparison	369	510	879
38/30	SNOTEL comparison, Gros Ventre subset analysis	365	499	864
All Path Rows		877	2516	4393

Table 5.2. 30 x 30 km subsets used for detailed analysis of the Landsat mean annual snow cover duration product. Forest cover indicates the percentage of pixels from the subset where the National Land Cover Database (NLCD) forest canopy layer indicates > 15% canopy cover. Mean canopy indicates the mean NLCD forest canopy for all pixels from the subset.

Subset	Landsat PR	Elev. Range (m)	Forest Cover	Mean Canopy
Cascades	Path 45 Row 27	410-2459	84%	52.6%
Sierra Nevada	Path 43 Row 33	1332-3162	33%	34.6%
Gros Ventre	Path 38 Row 30	1751-3233	55%	26.7%

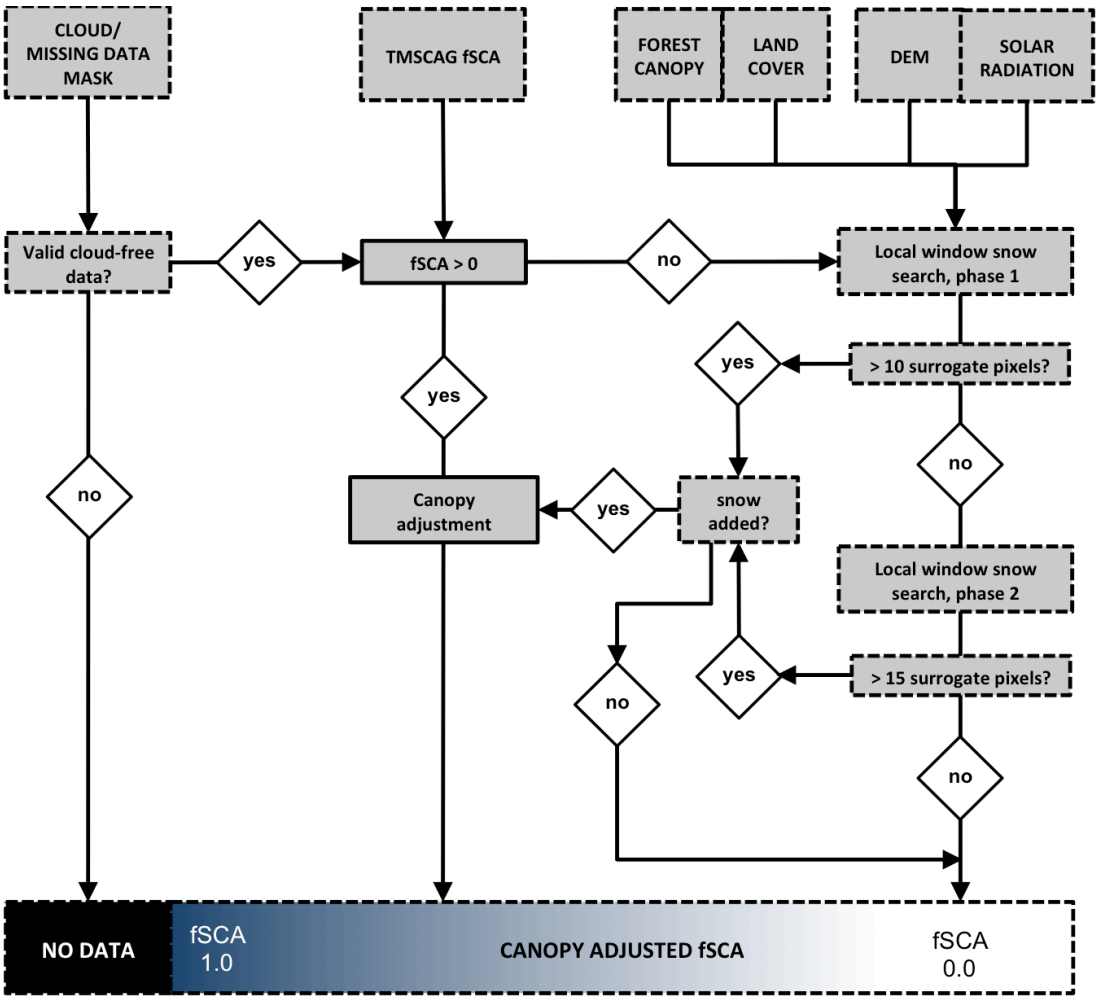

Figure 5.2. Flow chart for canopy adjustment processes used for adjustment of scene-based Landsat fSCA.

fSCA, and (3) a cloud mask.

Mean annual snow cover duration was calculated using all available Landsat-derived fSCA layers available for the period of record. For each pixel, we determined the fraction of cloud-free, valid pixels with snow cover for each month (e.g., the fraction of cloud free, valid pixels imaged during the month of June over the period 1986-2015). The monthly fractions were then averaged and multiplied by 365 to calculate mean annual snow cover duration.

5.2.3 Production of Scene-based Landsat fSCA Product

5.2.3.1 Datasets

We obtained 30 m resolution Landsat Climate Data Record (CDR) top-of-atmosphere (TOA) and surface reflectance (SR) products (Masek et al., 2006, available at http://earthexplorer.usgs.gov) for a total of 4383 Landsat scenes acquired between 1986 and 2016 in mountainous regions of the conterminous western United States (Table 5.2).

We acquired the 30 m resolution National Land Cover Database (NLCD) 2011 land cover and percent forest canopy datasets for the conterminous U.S. (available from http://www.mrlc.gov) and then extracted subsets covering our study areas. Each subset was reprojected to the UTM projection associated with Landsat scenes within the study area.

We obtained 1/3 arc second (approximately 10 m resolution) digital elevation models (DEMs) covering each of our study areas from the U.S. 3D Digital Elevation (3DEP) program (available from https://viewer.nationalmap.gov/basic/). Individual 1° tiles were mosaicked together, reprojected to the UTM projection associated with Landsat scenes within the study area, and then aggregated from 10 m to 30 m spatial resolution to correspond with the resolution of the Landsat scenes and ancillary data.

5.2.4.1 Image Processing

We retrieved fSCA for each pixel from each Landsat scene using TMSCAG, a spectral mixture analysis model that evolved from the original MEMSCAG algorithm

that calculated fSCA and snow grain size from optical imaging spectrometer data (Painter et al., 1998; Painter et al., 2003). The TMSCAG model is similar to the MODSCAG model (Painter et al., 2009), which works with multispectral MODIS data and has been widely used for retrieval of fSCA; the key difference is that the TMSCAG model is configured to handle radiometric saturation in spectral bands 1-4. A more detailed description of the TMSCAG model as well as validation of model performance is provided in Painter et al. (in review).

Potential solar radiation grids were calculated at 30 m spatial resolution using the r.sun algorithm available in GRASS GIS and the resampled 30 m DEM covering the study area. For each study area, we calculated potential solar radiation for every 10th day starting with day of year 274 (October 1 for regular years, September 30 for leap years). Potential solar radiation was interpolated for days in between, resulting in a daily time series of potential solar radiation. We then calculated cumulative potential solar radiation since October 1 for each day of the year.

We used a modification of the CFmask cloud masking approach (Zhu & Woodcock, 2012) described in Selkowitz and Forster (2015) to identify cloud-covered pixels in each Landsat scene. While the original CFmask has been demonstrated to consistently classify certain landscape patches containing snow and ice or a mixture of snow/ice and rock as cloud cover, this problem is minimized in the revised version. In high mountain areas, accuracy for the original CFmask algorithm is 66%, while accuracy for the revised CFmask approach is 88% (Selkowitz & Forster, 2015).

Figure 5.2 provides a flow chart that describes the full canopy adjustment process. In cases where retrieved fSCA is > 0 and < 1, we incorporate the retrieved fSCA value as well as the forest canopy fraction value from the National Land Cover Database (NLCD) to calculate an adjusted fSCA value. In previous work, several authors (Coons et al., 2014; Durand & Molotch, 2008; Molotch & Margulis, 2008; Raleigh et al., 2013) have used a similar approach that normalizes retrieved $fSCA_v$ by the noncanopy fraction of the pixel ($1\text{-}F_c$) to calculate an adjusted $fSCA_{adj}$ value. This approach is defined in Equation 1:

$$\mathrm{fSCA_{adj}} = min\left(\frac{\mathrm{fSCA_v}}{1-F_c}, 1.0\right) \quad (1)$$

In our approach, we use the NLCD canopy percent value as F_c. In addition, we add 0.35 F_c to the result calculated using equation 1. We added this term to equation 1 because the NLCD canopy dataset tends to underestimate forest canopy by an average of 9.7% (and by as much as 23.4% in the Sierra Nevada) (Nowak & Greenfield, 2010), and because the viewable snow fraction in areas with forest cover tends to be poorly illuminated due to shading from the canopy, often leading to underestimation of viewable fSCA. Our canopy adjustment approach is defined in Equation 2:

$$\mathrm{fSCA_{adj}} = min\left(\frac{\mathrm{fSCA_v}}{1-F_c} + 0.35\ Fc, 1.0\right) \quad (2)$$

In cases where retrieved fSCA is 0, we implement an additional approach designed to detect snow-covered pixels where forest canopy or a combination of forest canopy and shading would make snow cover detection otherwise impossible using optical remote sensing. We refer to this approach as the neighborhood canopy adjustment approach. In many cases where snow cover is present but not initially detected by TMSCAG, the viewable snow cover fraction is below the TMSCAG detection threshold of approximately 0.15.

The neighborhood canopy adjustment approach (defined below) relies on the examination of at least 10 surrogate pixels located near the target pixel. The ratio of surrogate pixels with snow cover to total surrogate pixels determines whether snow is classified at the target pixel. This process is conducted in two separate phases, with the second phase only implemented if necessary. In the first phase, surrogate pixels are identified within a 11 x 11 pixel neighborhood centered on the target pixel. To qualify as a surrogate pixel, NLCD forest canopy percent must be lower than at the target pixel, potential solar radiation must be greater than at the target pixel, and elevation must be no more than 75 m greater than at the target pixel (Table 5.3, Figure 5.3). In addition, to qualify as a surrogate pixel a pixel must also contain valid data (i.e., not be within a Landsat 7 scan line gap) and be cloud-free, according to the revised cloud cover mask described above.

If at least 10 surrogate pixels can be identified in the 11 x 11 local window, we compute the ratio of surrogate pixels with snow cover (fSCA > 0) to the total number of surrogate pixels. If this ratio exceeds 0.3, the target pixel is labeled as snow covered and given an fSCA value of 0.15. In some cases, however, less than 10

Table 5.3. Criteria for identification of surrogate pixels in the surrounding 11 x 11 or 31 x 31 pixel neighborhoods.

Criteria	**Rule for surrogate eligibility**
NLCD canopy	< target pixel AND < 60%
Potential solar radiation	>= target pixel
Elevation	< target pixel + 75
Cloud cover	Must be cloud-free, and valid (not in SLC gap)

surrogate pixels can be identified within the 11 x 11 pixel window. This can occur when the target pixel has unique canopy or topographic aspects when compared to nearby pixels, when all nearby pixels are covered by dense forest, or when the number of available surrogate pixels is reduced due to the presence of scan line corrector gaps or cloud cover.

In cases where < 10 surrogate pixels can be identified within the 11 x 11 local window, we initiate a second phase that examines a larger 31 x 31 pixel window with a larger pool of potential surrogate pixels. The criteria for identification of surrogate pixels in the second phase are the same as the criteria used in the first phase (Table 5.3). If at least 15 surrogate pixels can be identified in the 31 x 31 pixel window, we compute the ratio of snow covered surrogate pixels to total surrogate pixels in the same manner as the first phase. For the larger 31 x 31 pixel window, if the ratio of snow covered pixels to total surrogate pixels exceeds 0.45, the target pixel is labeled as snow covered and given an fSCA value of 0.15.

The size of neighborhoods used for identification of potential surrogate pixels was chosen to balance the need for a sufficient sample of surrogate pixels for decision making with the need to constrain potential surrogate pixels to those pixels

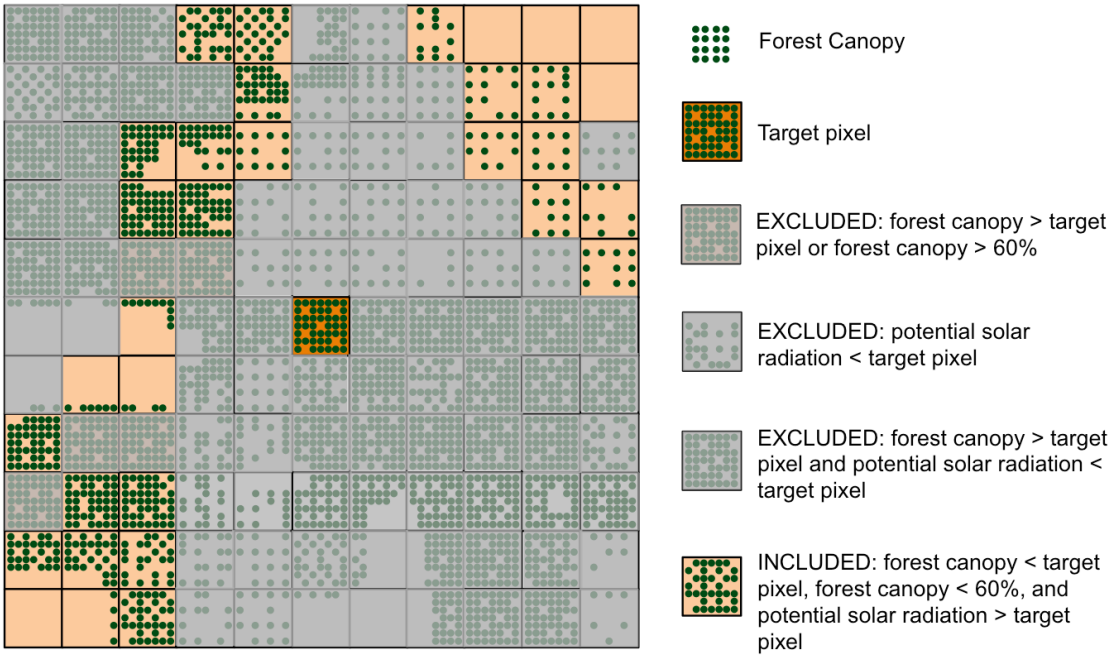

Figure 5.3. Identification of surrogate pixels meeting criteria listed in Table 5.2 in the 11 x 11 pixel neighborhood surrounding target pixel. The same process for identification of surrogate pixels is used for the larger 31 x 31 pixel window used in phase 2 (if necessary).

with similar climatic characteristics to the target pixel. This excludes solar radiation, which can vary substantially within the 11 x 11 or 31 x 31 pixel neighborhoods, but is explicitly accounted for. Initially, we attempt to identify at least 10 surrogate pixels within 150 m of the target pixel because, given the solar radiation and elevation constraints, the closest pixels are likely to exhibit snow cover conditions most similar to the target pixel. When insufficient surrogate pixels are available within the smaller neighborhood, we examine the larger neighborhood for surrogate pixels. The algorithm is designed to be conservative when identifying missed snow cover, and to be especially conservative when missed snow cover is identified using the larger 31 x 31 pixel neighborhood. For this reason, we require a

higher ratio of snow-covered to total surrogate pixels to identify additional snow covered pixels in the larger 31 x 31 pixel neighborhood.

Once the first, and, if necessary, second phases of neighborhood canopy adjustment have been implemented, standard canopy adjustment described in Equation 2 is applied to the resulting fSCA value of 0.15 (if snow cover is determined to be present) at the target pixel.

5.2.5 Calculation of Mean Annual Snow Cover Duration

For the Landsat snow cover duration product, we exploit the historical Landsat archive by incorporating fSCA and cloud cover calculated for all scenes acquired during the period of interest. Using these data, we compute the ratio of snow covered days for all cloud-free surface views to the total number of cloud-free surface views for each calendar month (e.g., all cloud-free surface views acquired during the month of June over the period 1986-2015) for each 30 m pixel (Figure 5.4). For this calculation, all fSCA values > 0 are counted as snow cover. The monthly ratio of snow covered days to total cloud-free days is then weighted by number of days in the month to compute the fraction of days with snow cover for the entire year, which is then multiplied by 365 to convert to mean annual snow cover duration in units of days.

Calculation of individual monthly ratios which are then converted to annual snow cover days is preferable to simply computing the ratio of snow-covered days to total cloud-free days for the entire period because at many locations, more cloud-

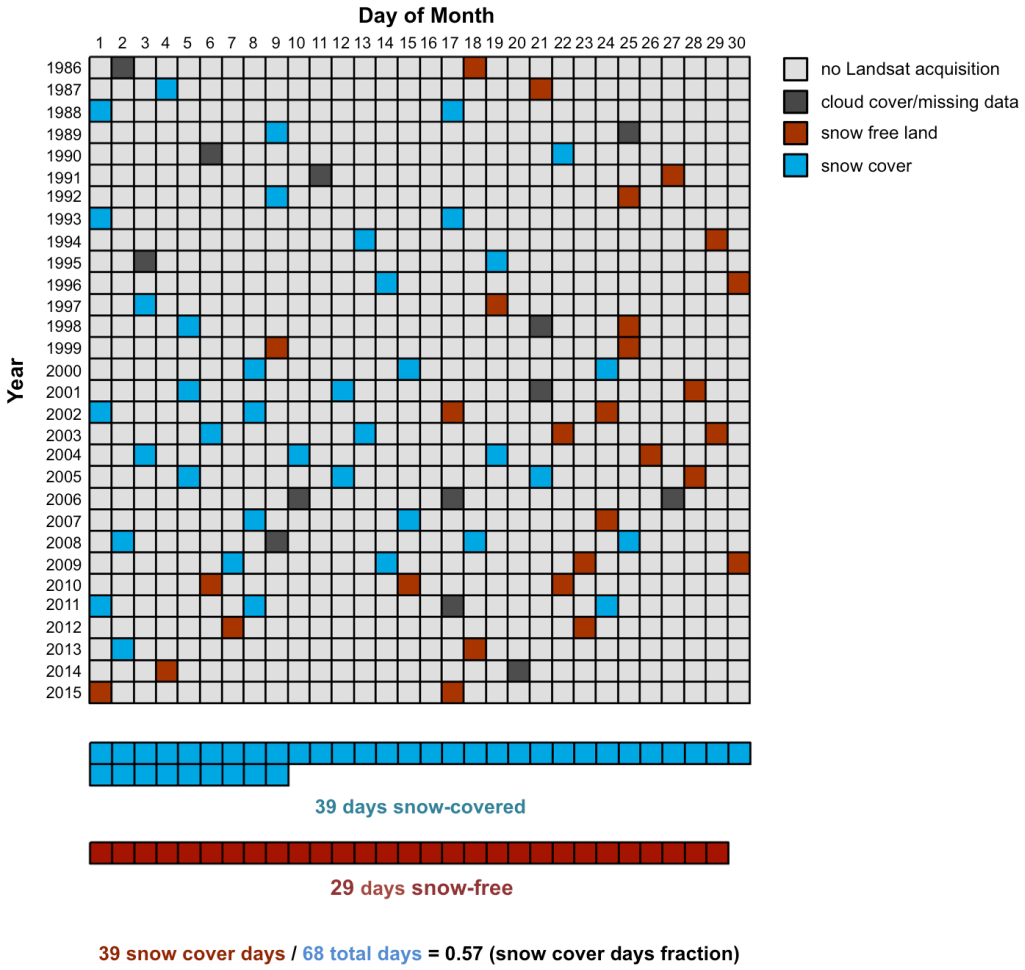

Figure 5.4. Calculation of the fraction of days in June with snow cover for the period 1986-2015 for a single 30 m grid cell. The matrix indicates 1 of 4 potential outcomes for each day in the period 1986-2015. Light grey squares indicate days when no Landsat data were acquired, dark grey squares indicate days when Landsat was acquired, but was not used for calculation of snow cover duration statistics due to cloud cover or missing data, red squares indicate snow free land, and light blue squares indicate snow-cover. The ratio of snow-covered days to snow-covered and snow-free days (total cloud-free days) is used to calculate the snow cover days fraction.

free views are available during the summer months than during the winter months. Consequently, computing the ratio of snow cover days to total cloud-free days for the entire period would result in underestimation of snow cover days because a disproportionate number of cloud-free views usually come from the summer months where snow cover is much less common.

5.2.6 Validation Approach

We use separate datasets to provide an accuracy assessment for the scene-based canopy-adjusted fSCA products and the snow cover duration product. Validation data for canopy-adjusted fSCA from individual Landsat scenes consisted of in situ snow cover fraction data collected at sites across the Sierra Nevada of California, while validation data for the snow cover duration datasets consisted of data from SNOTEL sites maintained by the Natural Resources Conservation Service (NRCS) at locations in California, Oregon, Washington, and Wyoming (Figure 5.1). The two separate datasets were chosen for validation of the two products because the in situ snow cover fraction data allowed for accuracy assessment of fractional snow covered area, which was not possible with SNOTEL data. The in situ snow cover fraction dataset, however, covered only the period 2014-2016 and thus could not be used for validation of mean annual snow cover duration calculated over longer periods. The SNOTEL dataset was selected for validation of the snow cover duration product because this was the only dataset available covering a 30-year period of record with sites covering multiple mountain ranges in the western United States.

5.2.6.1 Validation of Individual Scenes Using In Situ Sensor Arrays

We deployed 100 x 100 m temperature data arrays at 27 forest-covered sites across the Sierra Nevada of California. Sites ranged in elevation from 1860 m to 2930 m, included a wide range of forest canopy densities (4-83%), and included flat, gentle, and moderately steep (up to 23°) slopes on all aspects. Arrays consisted of 6 x 6 sensors spaced at 20 m intervals (2014-2015) or 5 x 5 sensors spaced at 25 m intervals (2015-2016). At each site, an array of temperature data loggers were buried 2-5 cm below the soil surface. Sensors were set to record temperature at 1.5 hour intervals. Temperature data loggers were deployed between August and November each year and retrieved between April and August of each year.

We used the algorithm designed by Raleigh et al. (2013) and adapted by Selkowitz et al. (2014) to convert hourly or 1.5 hourly temperature time series from individual temperature data loggers to daily snow cover fraction for each 100 m grid cell footprint we monitored. This algorithm classifies snow cover if temperature varies by less than 1°C at an individual temperature data logger over two consecutive 24-hour periods. A more detailed discussion of this approach can be found in Raleigh et al. (2013), Selkowitz et al. (2014), and Lundquist and Lott (2008).

The number of temperature data loggers used to compute daily snow cover fraction varied from 15-34. Although either 25 or 36 data loggers were installed at each site, some data loggers malfunctioned or stopped recording due to insufficient battery power and some data loggers could not be located (often as a result of ground disturbance by marmots or ground squirrels).

In order to verify that in situ temperature data loggers could accurately monitor the presence/absence of snow cover, we observed the presence/absence of snow cover at the location of the deployed temperature data loggers at four sites for a total of 5 days (one site was surveyed twice) in the spring and early summer of 2016. We used a GPS unit that provided real-time accuracy of +- 1.5 m or better to navigate to the location of temperature data loggers and record snow cover presence or absence above each temperature data logger. We collected 106 visual snow cover presence/absence observations for comparison with snow cover presence/absence classified using hourly temperature data from the data loggers using the algorithm described above.

5.2.6.2 Validation of Mean Annual Snow Cover Duration for 30-year and 5-year Periods Using SNOTEL Data

In order to assess the accuracy of the snow cover duration product, we used data from 72 SNOTEL sites from California, Oregon, Washington, and Wyoming. While SNOTEL pillow measurements of snow water equivalent cover < 2 m^2, a much smaller area than the 900 m^2 covered by the nominal Landsat pixel size, they are one of the only long term measurements of snow cover in mountains regions of the western U.S. Therefore, despite the mismatch in area monitored by a SNOTEL pillow compared to a Landsat pixel, SNOTEL sites still represent the best source of data for validation of mean annual snow cover duration over decades.

For our analysis, we calculated the mean annual snow cover duration (days with SWE > 0) observed at each SNOTEL station for the 30-year period 1986-2015

and compared this to the mean annual snow cover duration calculated from Landsat using the methods described above. We also conducted the same comparison between SNOTEL and Landsat-derived mean annual snow cover duration for the five year periods 1991-1995, 1996-2000, 2001-2005, 2006-2010, and 2011-2015. The period 1986-1990 was excluded because relatively few Landsat scenes were available during this period.

5.3 Results

5.3.1 Validation of In Situ Temperature Data Logger Snow Cover Monitoring Approach

Assessment of snow cover classification using in situ temperature data loggers compared to visual observations of snow cover in May and June of 2016 indicated agreement in 102 out of 106 cases, with one false positive and three false negatives (96% accuracy).

5.3.2 Landsat-derived fSCA Compared to In Situ fSCA

Comparison of TMSCAG and TMSCAG canopy adjusted fSCA to in situ fSCA from temperature data logger arrays indicated the canopy adjustment approaches used here substantially improved agreement between Landsat-derived and in situ measured fSCA (Table 5.4, Figure 5.5). While the standard canopy adjustment approach alone resulted in a substantial increase in accuracy, reducing RMSE from 0.49 to 0.25, the neighborhood adjustment approach resulted in further

Table 5.4. Accuracy metrics for TMSCAG, canopy adjusted TMSCAG, and neighborhood canopy adjusted TMSCAG.

Metric	TMSCAG	Adjusted	Adjusted + Neighborhood Canopy Adjustment
RMSE	0.49	0.25	0.20
Mean Error (Bias)	-0.38	-0.11	-0.07
Binary Accuracy	0.94	0.94	0.96
Binary Precision	0.99	0.99	0.99
Binary Recall	0.95	0.95	0.97
Binary F	0.97	0.97	0.98

improvement, reducing RMSE to 0.20. The mean error (bias) was initially -0.38 for the unadjusted TMSCAG data but was reduced to -0.07 when both adjustment approaches were applied. In the 139 instances where in situ fSCA was compared with TMSCAG and canopy-adjusted TMSCAG fSCA, there was only a single false positive snow cover result. There were no false positives resulting from addition of snow cover via the neighborhood canopy adjustment approach.

It is important to note that the full impact of the neighborhood canopy adjustment approach is less evident in this comparison because fSCA from 9 Landsat pixels is compared to in situ fSCA across a 100 x 100 m grid, reducing the impact of individual 30 m Landsat pixels where snow cover is missed on the overall accuracy. An example of TMSCAG fSCA compared to fSCA adjusted using both the standard canopy adjustment approach and neighborhood canopy adjustment approach is shown in Figure 5.6, which also maps the spatial distribution of additional snow cover pixels added using the neighborhood canopy adjustment approach.

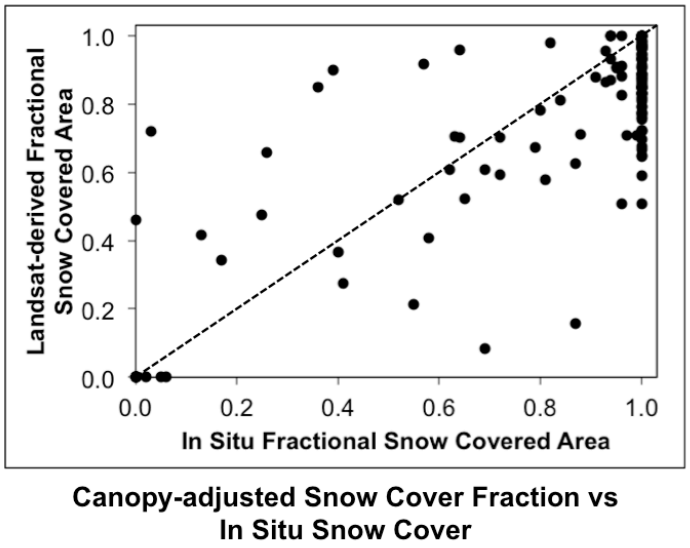

Figure 5.5. TMSCAG canopy-adjusted fSCA compared to in situ fSCA calculated from temperature data logger arrays. Both the standard canopy adjustment approach and the neighborhood canopy adjustment approach were applied to produce canopy-adjusted fSCA.

5.3.3 Mean Annual Snow Cover Duration

Mean annual snow cover duration computed from canopy-adjusted Landsat-derived fSCA for three 30 x 30 km subsets and three corresponding areas of detail are shown in Figure 5.7. The effect of elevation on snow cover duration is evident at the broader scale for the 30 x 30 km subsets, while the effects of both elevation and topographic position are evident at the finer scale shown for the 5 x 5 km areas of detail. The spatial distribution of additional snow cover days added via the canopy adjustment algorithm is shown for the three 30 x 30 km subsets in Figure 5.8. The three maps of additional snow cover days added via neighborhood canopy adjustment and the corresponding cumulative histograms demonstrate that impact of the canopy adjustment algorithm was largest in the Cascades subset, where 30 or more days were added to 27% of all pixels. The impact of the canopy adjustment

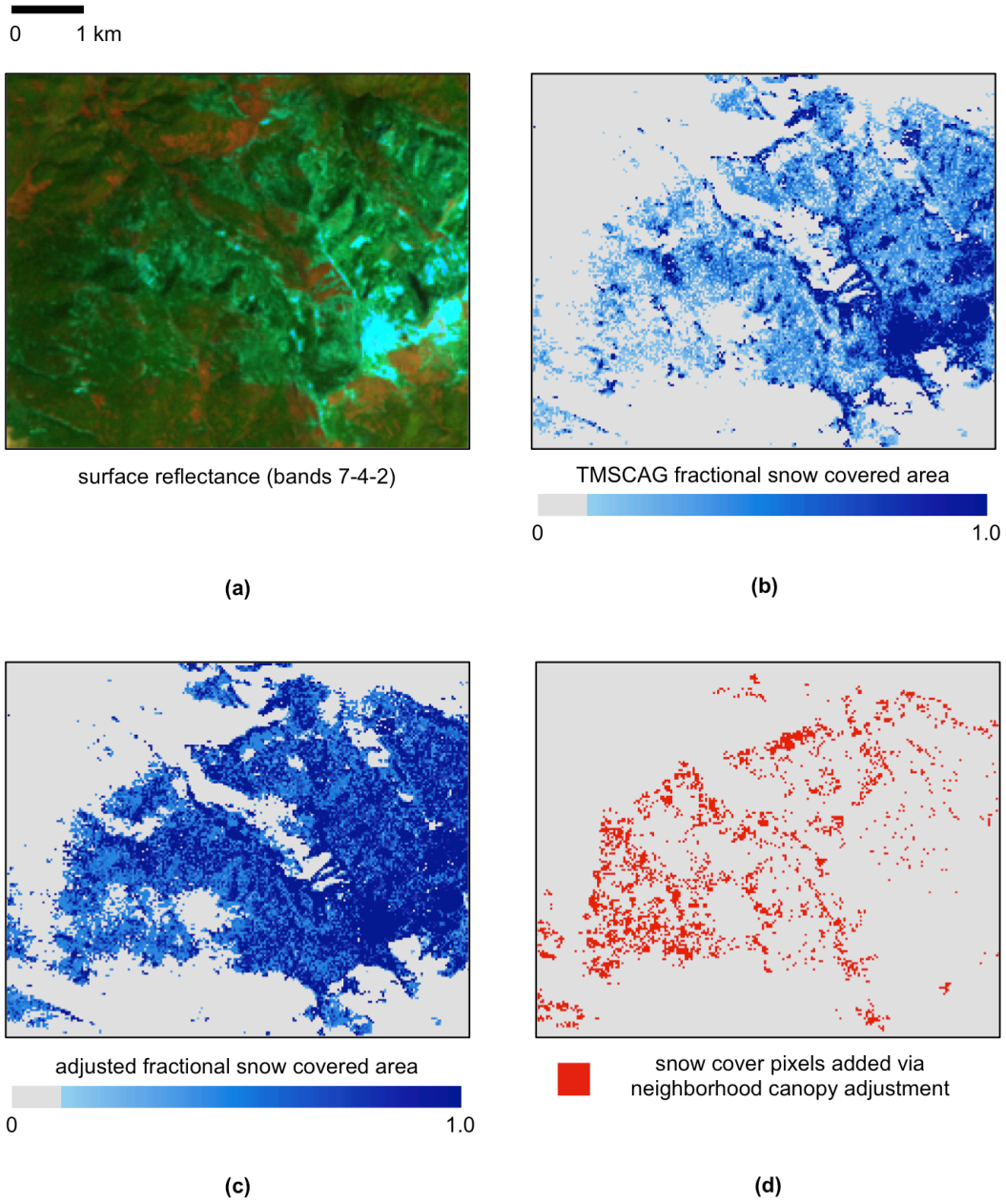

Figure 5.6. Demonstration of canopy adjustment for an area in the northern Sierra Nevada on April 20, 2009: (a) Landsat surface reflectance (bands 7-4-2), (b) TMSCAG fSCA, (c) canopy adjusted TMSCAG fSCA, and (d) areas of snow cover added using the neighborhood canopy adjustment approach.

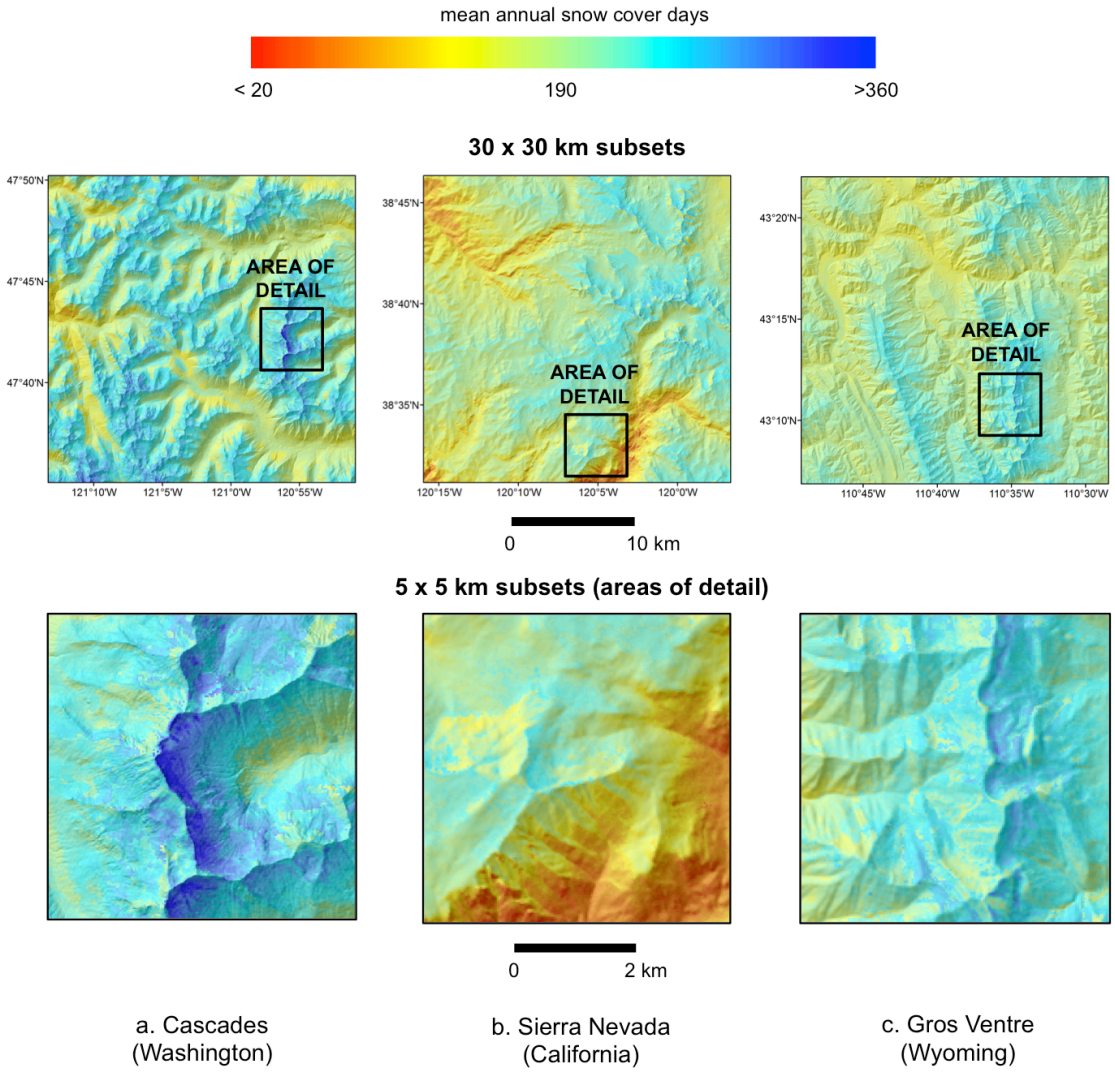

Figure 5.7. Mean annual snow cover duration for three 30 x 30 km subsets: (a) Cascades (Washington), (b) Sierra Nevada (California), and (c) Gros Ventre (Wyoming).

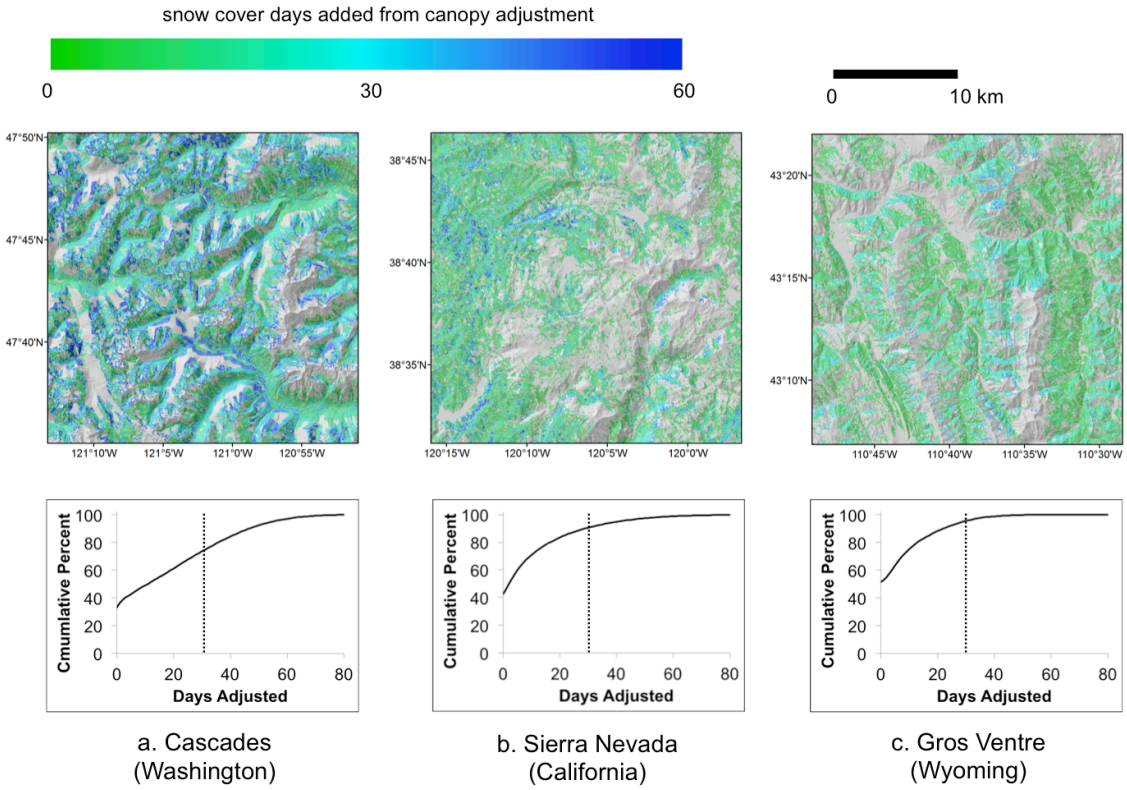

Figure 5.8. Additional snow cover days added using the neighborhood canopy adjustment approach for three 30 x 30 km subsets: (a) Cascades (Washington), (b) Sierra Nevada (California), and (c) Gros Ventre (Wyoming). The dashed line corresponds to 30 days added via the neighborhood canopy adjustment approach.

algorithm was substantially less for the Sierra Nevada subset, where 30 or more days were added to just 9% of pixels, and for the Gros Ventre subset, where 30 more days were added to only 5% of all pixels.

The percent of all cloud-free pixels where snow cover was added via neighborhood canopy adjustment, shown by month (Figure 5.9) tells a similar story, with snow cover added for substantially more instances in the Cascades subset than in the Sierra Nevada subset or Gros Ventre subset. Figure 5.9 also indicates how the impact on mapped SCA varies seasonally. For all three subsets, the percentage of

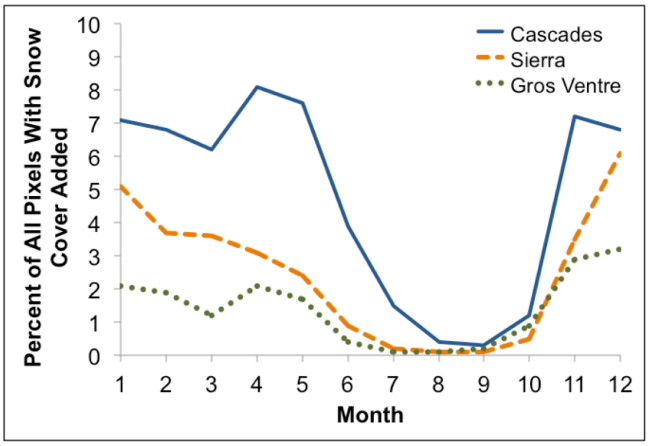

Figure 5.9. Percent of all cloud-free pixels where snow cover was added via canopy adjustment, shown by month.

snow cover pixels added is high during December and January and low during the summer and early fall months. In the Cascades, and to a lesser extent in the Sierra Nevada, a secondary peak in the percentage of added snow cover pixels occurs in April and May. The neighborhood canopy adjustment approach occasionally fails due to insufficient surrogate pixels within both the 11 x 11 and 31 x 31 pixel neighborhoods. The incidence of failure is determined ultimately by not only the prevalence of surrogate pixels within the local neighborhood, but, on a scene-by-scene basis, whether or not those potential surrogate pixels are obscured by clouds or scan-line correction failure gaps. The spatial distribution of failure frequency (as a fraction of total valid cloud-free days at each pixel) is shown in Figure 5.10, along with cumulative histograms that indicate the percent of pixels affected by various model failure rates. These data suggest that failure of the neighborhood canopy adjustment approach is more common in the Cascades subset than in the other two subsets, where 17% of pixels experienced failure in more than 10% of instances. By

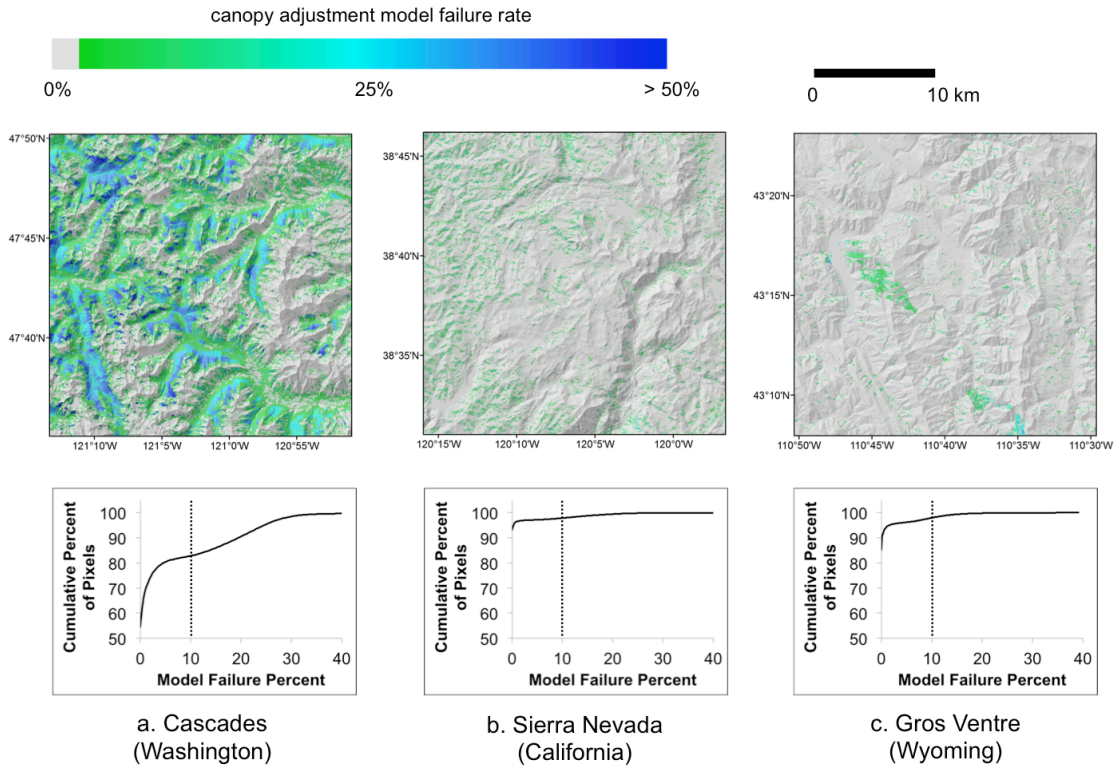

Figure 5.10. Canopy adjustment model failure frequency for three 30 x 30 km subsets: (a) Cascades (Washington), (b) Sierra Nevada (California) and, (c) Gros Ventre (Wyoming).

contrast, in the Sierra Nevada and Gros Ventre subsets, only about 2% of pixels experienced model failure in more than 10% of instances.

Comparison between mean annual snow cover duration calculated from SNOTEL stations and from the original TMSCAG and canopy-adjusted TMSCAG image data allow for quantification of the improvement in accuracy achieved via the neighborhood canopy adjustment approach. This comparison is based on binary snow cover retrievals, where the total fraction of days with fSCA > 0 is compared to the number of days where the corresponding SNOTEL site recorded SWE > 0. It is important to note that the standard canopy adjustment approach described in Equation 2 therefore has no impact on accuracy in this comparison. This is because

the standard canopy adjustment approach only adjusts pixels where a snow cover fraction > 0 has been detected. Consequently, differences between the unadjusted and adjusted results for mean annual snow cover duration are due entirely to the implementation of the neighborhood canopy adjustment approach.

While the unadjusted results are reasonably accurate for sites with canopy cover < 50%, mean annual snow cover duration is severely underestimated at many sites with canopy cover > 50% (Figure 5.11a). When fSCA from individual scenes is adjusted using the neighborhood canopy adjustment approach, however, agreement between mean annual snow cover duration from SNOTEL sites and from Landsat improves substantially at all but one site (Figure 5.11b). The local window canopy adjustment approach reduces RMSE from 22.6 days to 14.7 days and essentially eliminates the negative bias in mean snow cover duration (Table 5.5). Figures 5.11c and 5.11d also indicate that neighborhood canopy adjustment has a much larger impact at sites in the Cascades than at sites in the Sierra Nevada or Rocky Mountains.

Agreement between TMSCAG canopy-adjusted snow cover duration and snow cover duration calculated from SNOTEL sites for 5-year periods is slightly lower than for the full 30 1986-2015 period, with RMSE ranging from 15.4 - 20.7 (Table 5.6). However, the improvement in accuracy resulting from the neighborhood canopy adjustment approach is still evident, and the negative bias for the canopy adjusted results is < 3 days for 4 of the 5 periods considered.

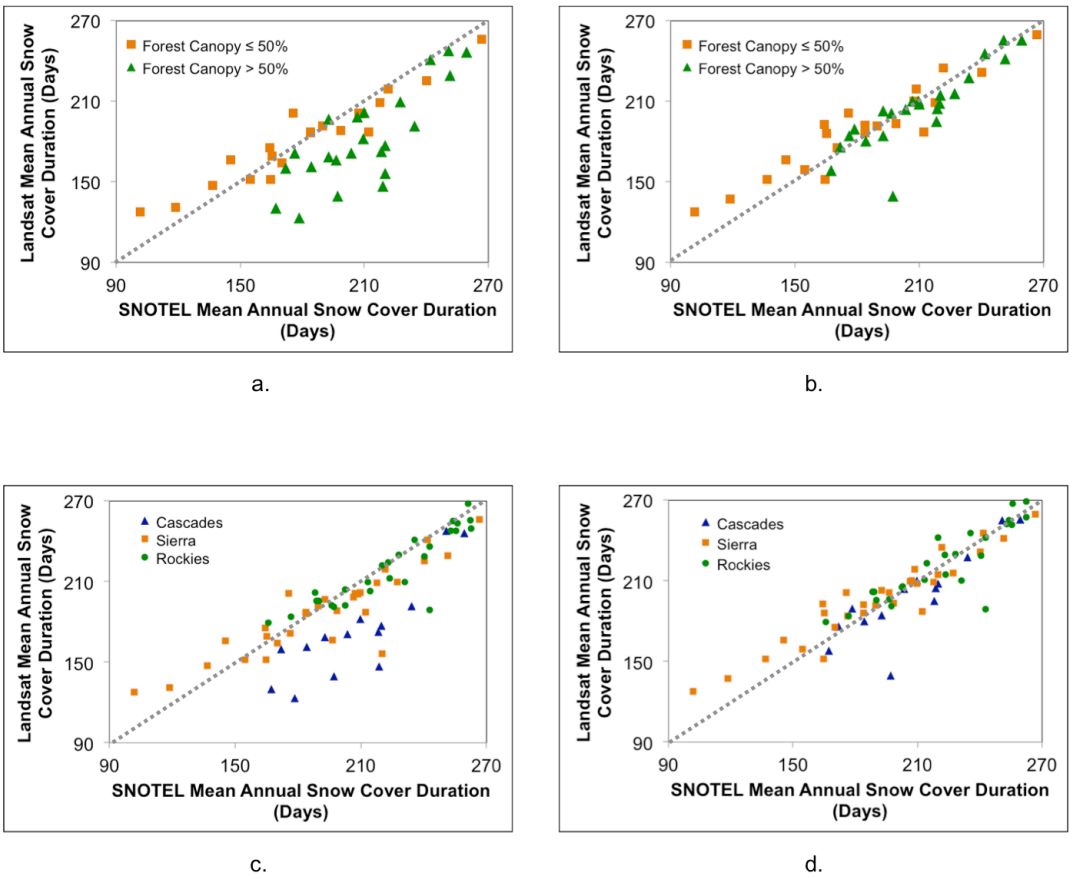

Figure 5.11. Comparison between mean annual snow cover duration calculated from SNOTEL data and mean annual snow cover duration calculated from Landsat. (a) unadjusted snow cover duration, with colors indicating forest canopy density (b) adjusted snow cover duration, with colors indicating forest canopy density, (c) unadjusted snow cover duration, with colors indicating region, and (d) adjusted snow cover duration, with colors indicating region.

Table 5.5. Accuracy metrics for mean annual snow cover duration (days) calculated using unadjusted TMSCAG and canopy adjusted TMSCAG relative to mean annual snow cover duration calculated from SNOTEL sites.

Metric	TMSCAG	Canopy Adjusted
RMSE	22.6	14.7
Mean Error (Bias)	-10.4	0.6

Table 5.6. Accuracy metrics for mean annual snow cover days calculated using adjusted TMSCAG for periods 1991-1995, 1996-2000, 2001-2005, 2006-2011, and 2011-2015.

Metric	1986 - 2015	1991 - 1995	1996 - 2000	2001- 2005	2006 - 2010	2011- 2015
RMSE	15.1	20.0	15.4	18.1	19.3	20.7
Mean Error (Bias)	0.5	-1.3	-5.0	-2.3	0.0	-0.4

5.4 Discussion

TMSCAG has been demonstrated effective for retrieval of visible fSCA across a wide range of snow cover conditions, topography, vegetation types, and solar illumination conditions (Painter et al., in review). When significant forest canopy is present, however, the difference between the retrieved viewable fSCA and in situ fSCA beneath the canopy can be significant. In cases where snow cover is missed entirely, this can also impact mean annual snow cover duration calculated using all available scenes for a period of record. The results presented here indicate that TMSCAG fSCA mapping can be extended to allow for effective retrievals of in situ fSCA under forest canopies across the forests of the western conterminous U.S. mountains, and likely in other regions as well.

The canopy adjustment approach presented here not only adjusts viewable fSCA values > 0, but also adds snow to forested pixels where snow cover was initially not retrieved if conditions at surrounding pixels with similar characteristics suggest that snow cover was likely missed. The adjustment of initial fSCA values > 0

has been applied previously in several studies (Coons et al., 2014; Durand & Molotch, 2008; Molotch & Margulis, 2008; Raleigh et al., 2013). Addition of snow cover to forested pixels initially identified as snow-free, however, is a novel approach critical for effectively monitoring snow cover conditions in forested regions at the Landsat spatial resolution.

Comparison between TMSCAG fSCA and in situ fSCA in forested areas of the Sierra Nevada indicated that, as expected, the viewable snow cover fraction retrieved from TMSCAG is usually substantially lower than the in situ fSCA. While the standard canopy adjustment approach improved agreement between in situ fSCA and Landsat-derived fSCA in many instances, the neighborhood canopy adjustment approach resulted in further improvement in cases where snow cover was initially missed at some of the 9 Landsat pixels covering the 100 x 100 m in situ grid.

The lack of false positives for snow cover resulting from application of the neighborhood canopy adjustment approach suggest that this is a relatively conservative approach to the problem of missed snow cover beneath forest canopy. In fact, the algorithm is structured so that snow cover can only be added if a substantial fraction of pixels within 450 m of the target pixel have been identified as snow covered by TMSCAG. Checks are also in place to prohibit the addition of snow cover when nearby snow cover is only identified at pixels with a lower cumulative solar radiation load or at substantially higher elevations. Despite these conditions and the lack of false positives for snow cover identified in the in situ fSCA

comparison dataset, we acknowledge that some false positives will inevitably result from this canopy adjustment approach.

Our results suggest the importance of the neighborhood canopy adjustment varies both by region and over time, with frequent instances of adjustment to add snow cover initially missed concentrated in both clusters of pixels and specific times of year. The substantially higher amount of snow covered pixels added in the Cascades from neighborhood canopy adjustment relative to the Sierra Nevada and Gros Ventre subsets can be explained primarily by the higher forest density and greater prevalence of dense forest in the Cascades. The canopy adjustment approach may also be less necessary in mid-winter in the colder continental climate of the Gros Ventre subset, where snow cover is often retained for long periods in the canopy (Hedstrom & Pomeroy, 1998), resulting in a higher viewable fSCA and thus fewer missed snow cover pixels.

The higher percentage of added snow cover pixels occurring in the months of November, December, and January for all three subsets can be explained by the relatively poor solar illumination conditions resulting from higher solar zenith angles during these months. Painter et al. (in review) found that TMSCAG is more likely to underestimate snow cover under poor illumination conditions, and this is likely exacerbated by forest canopy that leads to a further reduction in illumination at the snow surface. Under these conditions, which result in a higher frequency of pixels where snow cover is not initially identified by TMSCAG, the neighborhood canopy adjustment approach is employed more frequently. The secondary peak of added snow cover pixels during the months of April and May in the Cascades and

Sierra Nevada is likely due to the higher prevalence of partially snow covered pixels during this period, which typically corresponds with snowmelt across much of these two study areas. The density of forest canopy cover necessary to result in errors of omission declines substantially as the ground snow cover fraction declines.

The comparison between mean annual snow cover duration calculated from SNOTEL data and from Landsat-derived fSCA confirms the effectiveness of the neighborhood canopy adjustment approach. Without an approach that considers nearby pixels or some sort of ancillary data, mean annual snow cover duration calculated from Landsat-derived fSCA is significantly underestimated at many pixels with moderate to dense forest canopy. While the canopy adjustment approach described here is not effective for eliminating all errors of omission at all Landsat pixels in all instances, it significantly reduces underestimation of mean snow cover duration at many forested pixels.

Perhaps the largest limitation for the current approach to production of both scene-based and mean annual snow cover duration products is the inability of the neighborhood canopy adjustment approach to effectively correct all pixels. While instances of failure due to insufficient surrogate pixels are relatively rare, they are typically concentrated in both space and time and can therefore have a notable impact on results in certain areas and for certain periods. It may be possible to reduce the number of cases where the neighborhood canopy adjustment approach fails by extending the size of the neighborhood for identification of surrogate pixels. A completely effective solution to this limitation, however, will likely require the

inclusion of different remote sensing data such as lidar or a physically-based modeling approach.

Another limitation of both the scene-based canopy-adjusted fSCA and the snow cover duration products is that the accuracy of canopy-adjusted snow covered area depends on accurate and consistent forest canopy information. Presently, this information is provided by the NLCD 2011 forest canopy layer, which has been shown to underestimate forest canopy by an average of 9.7% nationally and by 23.4% in the Sierra Nevada (Nowak & Greenfield, 2010). Perhaps more importantly, the NLCD canopy layer represents only a brief period of time and is likely to be incorrect in instances where land cover change has occurred either before or after the publication of the dataset. For example, a large fire might remove most or all of the canopy for a patch of pixels. If the reduction in canopy from the fire is not reflected in the canopy layer, canopy adjustment will be incorrectly applied to this patch of pixels, resulting in an overestimation of fSCA and possibly the generation of false positive snow cover pixels (although only if other nearby pixels are snow covered). A possible solution would be to generate new canopy layers annually or possibly even a new canopy layer for every Landsat scene processed in order to reduce the possibility of these types of errors.

The relatively long 16-day interval between scene acquisitions from Landsat also limits our ability to produce a snow cover duration product for time periods shorter than about 5 years. The sporadic occurrence of cloud cover and the 16-day repeat interval for the Landsat 5 and 7 spacecraft have resulted in an irregular frequency of cloud-free surface views. Over periods longer than approximately 5

years, this irregular availability of cloud-free surface views amounts to a semi-random sample of cloud-free surface views from the early, middle and late portions of each month and from above-average, average, and below-average snow cover years. For shorter periods, however, the impact of the timing of each cloud-free surface view can skew the calculation of mean annual snow cover duration. Our results indicate that accuracy of the snow cover duration product is lower for 5-year periods than it is for the full 1986-2015 period. Future iterations of the Landsat snow cover products will incorporate data from Landsat 8 and possibly from the Sentinel 2A instrument, potentially allowing for generation of snow cover duration products based on as little as one year of data.

5.5 Conclusions

Results presented here indicate that while the unadjusted Landsat snow cover products underestimate fSCA for individual scenes and underestimate mean annual snow cover duration calculated from all available scenes, this underestimation is substantially reduced for the canopy-adjusted versions of these products. The incorporation of a canopy adjustment approach that considers the snow cover status of nearby pixels allows for accurate estimation of scene-based fSCA in many cases even when the initially retrieved fSCA value is zero. When combined with a cloud mask optimized for use in mountainous environments, the resulting canopy-adjusted Landsat fSCA data can be used to provide an accurate estimate of mean annual snow cover duration at 30 m spatial resolution for the entire Landsat period of record as well as for temporal subsets as short as 5 years.

Data from the SNOTEL network indicate the mean annual snow cover duration for the period 1986-2015 calculated using this approach has an RMSE of 14.7 days and a bias of +0.6 days over the range of 90-270 days of annual snow cover.

While the impact of the canopy adjustment approach varies by region due primarily to differences in forest cover, it can have a large impact on local snow cover duration estimates for pixels with forest canopy even within regions where forest cover is relatively sparse or mostly absent. The primary limitation of the canopy adjustment approach is that it is ineffective in cases where an insufficient number of surrogate pixels can be located within the local neighborhood, such as when a target pixel is surrounded by large tracts of contiguous, high density forest cover. Despite this limitation, the canopy adjustment approach substantially increases accuracy of fSCA maps in forested and partially forested regions. Together, the improved accuracy of the scene-based fSCA product and the approach developed to incorporate all Landsat data acquired during a period of record to calculate mean annual snow cover duration enables the production of an accurate snow cover duration product at a higher spatial resolution than has previously been available. The relatively high spatial resolution of both the Landsat scene-based snow cover product and the Landsat snow cover duration product can help illuminate relatively fine scale snow cover patterns common in rugged topography that would be obscured by the coarser spatial resolution of sensors like MODIS or VIIRS. This will result in enhanced understanding and possibly new insights into snow cover patterns and processes, particularly in regions with complex topography that consistently feature a high degree of fine scale snow cover variability.

5.6 Acknowledgements

Funding for this research was provided by the Land Remote Sensing Program of the US Geological Survey. The authors gratefully acknowledge assistance in the field provided by Melanie Cota, Mike Stockwell and Erin Orozco. Part of this work was performed at the Jet Propulsion Laboratory, California Institute of Technology under a contract with NASA

5.7 References

Anderton, S.P., White, S.M., & Alvera, B. (2002). Micro-scale spatial variability and the timing of snow melt runoff in a high mountain catchment. *Journal of Hydrology*, *268*, 158-176.

Aubry, K.B., Mckelvey, K. S., & Copeland, J. P. (2007). Distribution and broadscale habitat relations of the wolverine in the contiguous United States. *The Journal of Wildlife Management*, *71*(7), 2147-2158.

Barnett, T.P., Adam, J.C., & Lettenmaier, D.P. (2005). Potential impacts of a warming climate on water availability in snow-dominated regions. *Nature*, *438*(17), 303-309.

Beck, P. S., Kalmbach, E., Joly, D., Stien, A., & Nilsen, L. (2005). Modelling local distribution of an Arctic dwarf shrub indicates an important role for remote sensing of snow cover. *Remote Sensing of Environment*, *98*(1), 110-121.

Bekker, M. F. (2005). Positive feedback between tree establishment and patterns of subalpine forest advancement, Glacier National Park, Montana, USA. *Arctic, Antarctic, and Alpine Research, 37*(1), 97-107.

Bernhardt, M., Liston, G.E., Strasser, U., Zangl, G., & Schulz, K. (2010). High resolution modeling of snow transport in complex terrain using downscaled MM5 wind fields. *The Cryosphere*, *4*, 99-113.

Bernhardt, M., & Schulz, K. (2010). SnowSlide: A simple routine for calculating gravitational snow transport. *Geophysical Research Letters*, *37*(11).

Bloschl, G., Kirnbauer, R., & Gutknecht, D. (1991). Distributed snowmelt simulations in an alpine catchment 1. Model evaluation on the basis of snow cover patterns. *Water Resources Research*, 27(12), 3171-3179.

Billings, W.D., & Bliss, L.C. (1959). An alpine snowbank environment and its effects on vegetation, plant development, and productivity. *Ecology*, *40*(3), 388-397.

Bronge†, L.B., & Bronge†*, C. (1999). Ice and snow-type classification in the Vestfold Hills, East Antarctica, using Landsat-TM data and ground radiometer measurements. *International Journal of Remote Sensing*, *20*(2), 225-240.

Cline, D.W., Bales, R.C., & Dozier, J. (1998). Estimating the spatial distribution of snow in mountain basins using remote sensing and energy balance modeling. *Water Resources Research*, *34*(5), 1275-1285.

Cohen, J., & Entekhabi, D. (1999). Eurasian snow cover variability and Northern Hemisphere climate predictability. *Geophysical Research Letters*, *26*(3), 345-348.

Coons, L. P., Nolin, A.W., Gleason, K.E., Mar, E.J., Rittger, K., Roth, T.R., & Painter, T.H. (2014). Seeing the snow through the trees: Toward a validated canopy adjustment for satellite snow-covered Area. In V. Lakshmi (Ed.) *Remote Sensing of the Terrestrial Water Cycle*. Hoboken, NJ: John Wiley and Sons.

Deems, J.S., Fassnacht, S.R., & Elder, K. J. (2006). Fractal distribution of snow depth from LiDAR data. *Journal of Hydrometeorology*, *7*(2), 285-297.

Dozier, J. (1984). Snow reflectance from LANDSAT-4 Thematic Mapper. *IEEE Transactions on Geoscience and Remote Sensing*, *GE-22*(3), 323-328.

Durand, M., Molotch, N.P., & Margulis, S.A. (2008). Merging complementary remote sensing datasets in the context of snow water equivalent reconstruction. *Remote Sensing of Environment*, *112*: 1212-1225.

Eastland, W.G., Bowyer, R.T., & Fancy, S.G. (1989). Effects of snow cover on selection of calving sites by caribou. *Journal of Mammology*, *70*(4), 824-828.

Fily, M., Bourdelles, B., Dedieu, J.P., & Sergent, C. (1997). Comparison of in situ and Landsat Thematic Mapper derived snow grain characteristics in the Alps. *Remote Sensing of Environment*, *59*, 452-460.

Fily, M., Dedieu, J.P., & Durand, Y. (1999). Comparison between the results of a snow metamorphism model and remote sensing derived snow parameters in the Alps. *Remote Sensing of Environment*, *68*, 254-263.

Groffman, P.M., Driscoll, C.T., Fahey, T.J., Hardy, J.P., Fitzhugh, R.D., & Tierney, G.L. (2001). Colder soils in a warmer world: A snow manipulation study in the northern hardwood forest ecosystem. *Biogeochemistry*, *56*, 135-150.

Groisman, P.Y, Karl, T.R, & Knight, R.W. (1994). Observed impact of snow cover on the heat balance and the rise of continental spring temperatures. *Science*, *263*, 198-200.

Hall, D.K., Chang, A.T.C., Foster, J.L., Benson, C.S., & Kovalick, W.M. (1989). Comparison of in situ and Landsat derived reflectance of Alaskan glaciers. *Remote Sensing of Environment*, *28*, 23-31.

Hall, D.K., Riggs, G.A., & Salomonson, V.V. (1995). Development of methods for mapping global snow cover using moderate resolution imaging spectroradiometer data. *Remote Sensing of Environment*, *54*, 127-140.

Hedstrom, N. R., & Pomeroy, J. W. (1998). Measurements and modelling of snow interception in the boreal forest. *Hydrological Processes*, *12*(1011), 1611-1625.

Hessl, A.E., & Baker, W.L. (1997). Spruce and fir regeneration and climate in the forest-tundra ecotone of Rocky Mountain National Park, Colorado, USA. *Arctic and Alpine Research*, *29*(2), 173-183.

Huggard, D.J. (1993). Effects of snow depth on predation and scavenging by gray wolves. *The Journal of Wildlife Management*, *57*(2): 382-388.

Klein, A.G., Hall, D.K., & Riggs, G.A. (1998). Improving snow cover mapping in forests through the use of a canopy reflectance model. *Hydrological Processes*, *12*: 1723-1744.

Klein, A.G., & Isacks, B.L. (1999). Spectral mixture analysis of Landsat thematic mapper images applied to the detection of the transient snowline on tropical Andean glaciers. *Global and Planetary Change*, *22*, 139-154.

Laperriere, A.J., & Lent, P.C. (1977). Caribou feeding sites in relation to snow characteristics in northeastern Alaska. *Arctic*, *10*, 101-108.

Letsinger, S.L., & Olyphant, G.A. (2007). Distributed energy-balance modeling of snow-cover evolution and melt in rugged terrain: Tobacco Root Mountains, Montana, USA. *Journal of Hydrology*, *336*(1-2), 48-60.

Luce, C.H., & Tarboton, D.G. (1998). The influence of the spatial distribution of snow on basin-averaged snowmelt. *Hydrological Processes*, *12*, 1671-1683.

Lundquist, J.D., & Dettinger, M.D., (2005). How snowpack heterogeneity affects diurnal streamflow timing. *Water Resources Research*, *41*, W05007.

Lundquist, J.D., & Lott, F. (2008). Using inexpensive temperature sensors to monitor the duration and heterogeneity of snow-covered areas. *Water Resources Research*, *44*(4).

Magee, T.K., & Antos, J.A. (1992). Tree invasion into a mountain-top meadow in the Oregon Coast Range, USA. *Journal of Vegetation Science*, *3*(4), 485-494.

Margulis, S.A., Cortés, G., Girotto, M., & Durand, M. (2016). A Landsat-Era Sierra Nevada snow reanalysis (1985–2015). *Journal of Hydrometeorology*,*17*(4), 1203-1221.

Martinec, J., & Rango, A. (1981). Areal distribution of snow water equivalent evaluated by snow cover monitoring. *Water Resources Research*, 5, 1480-1488.

Masek, J.G., Vermote, E.F., Saleous, N.E., Wolfe, R., Hall, F.G., Huemmrich, K. F., & Lim, T. K. (2006). A Landsat surface reflectance dataset for North America, 1990-2000. *IEEE Geoscience and Remote Sensing Letters*, *3*(1), 68-72.

Mock, C. J., & Birkeland, K. W. (2000). Snow avalanche climatology of the western United States mountain ranges. *Bulletin of the American Meteorological Society*, *81*(10), 2367.

Molotch, N.P. (2009). Reconstructing snow water equivalent in the Rio Grande headwaters using remotely sensed snow cover data and a spatially distributed snowmelt model. *Hydrological Processes*, *23*(7), 1076-1089.

Molotch, N.P., & Margulis, S.A. (2008). Estimating the distribution of snow water equivalent using remotely sensed snow cover data and a spatially distributed snowmelt model: A multi-resolution, multi-sensor comparison. *Advances in Water Resources*, *31*(11), 1503-1514.

Nowak, D.J., & Greenfield, E.J. (2010). Evaluating the National Land Cover Database tree canopy and impervious cover estimates across the conterminous United States: A comparison with photo-interpreted estimates. *Environmental Management*, *46*(3), 378-390.

Painter, T.H., Rittger, K., & Selkowitz, D. (in review). Retrieval of fractional snow-covered area from Landsat Thematic Mapper data.

Painter, T.H., Roberts, D.A., Green, R.O., & Dozier, J. (1998). The effect of grain size on spectral mixture analysis of snow-covered area from AVIRIS data. *Remote Sensing of Environment*, *65*(3), 320-332.

Painter, T.H., Dozier, J., Roberts, D.A., Davis, R.E., & Green, R.O. (2003). Retrieval of subpixel snow-covered area and grain size from imaging spectrometer data. *Remote Sensing of Environment, 85*(1), 64-77.

Painter, T.H., Rittger, K., McKenzie, C., Slaughter, P., & Davis, R.E. (2009). Retrieval of subpixel snow covered area, grain size, and albedo from MODIS. *Remote Sensing of Environment*, *113*(4), 868-879.

Quinton, W.L., Bemrose, R.K., Zhang, Y., & Carey, S.K., (2009). The influence of spatial variability in snowmelt and active layer thaw on hillslope drainage for an alpine tundra hillslope. *Hydrological Processes*, 23(18), 2628-2639.

Rittger, K., Painter, T.H., & Dozier, J. (2013). Assessment of methods for mapping snow cover from MODIS. *Advances in Water Resources*, *51*, 367-380.

Rosenthal, W., & Dozier, J. (1996). Automated mapping of montane snow cover at subpixel resolution from the Landsat Thematic Mapper. *Water Resources Research*, *32*(1), 115-130.

Salomonson, V.V., & Appel, I., (2004). Estimating fractional snow cover from MODIS using the normalized difference snow index. *Remote Sensing of Environment*, *89*(3), 351-360.

Selkowitz, D. J., Forster, R. R., & Caldwell, M. K. (2014). Prevalence of pure versus mixed snow cover pixels across spatial resolutions in alpine environments. *Remote Sensing*, *6*(12), 12478-12508.

Selkowitz, D.J., & Forster, R.R. (2015). An automated approach for mapping persistent ice and snow cover over high latitude regions. *Remote Sensing*, *8*(1), 16.

Stenseth, N.C., Shabbar, A., Chan, K.S., Boutin, S., Rueness, E.K., Ehrich, D., & Jakobsen, K. S. (2004). Snow conditions may create an invisible barrier for lynx. *Proceedings of the National Academy of Sciences of the United States of America*, *101*(29), 10632-10634.

Sweeney, J.M., & Sweeney, J.R. (1984). Snow depths influencing winter movements of elk. *Journal of Mammalogy*, *65*(3), 524-526.

Tinkham, W. T., Smith, A. M., Marshall, H. P., Link, T. E., Falkowski, M. J., & Winstral, A. H. (2014). Quantifying spatial distribution of snow depth errors from LiDAR using Random Forest. *Remote Sensing of Environment*, *141*, 105-115.

Trujillo, E., & Molotch, N.P. (2014). Snowpack regimes of the western United States. *Water Resources Research*, *50*(7), 5611-5623.

Vikhamar, D., & Solberg, R. Snow-cover mapping in forests by constrained linear spectral unmixing of MODIS data. (2003). *Remote Sensing of Environment*, *88*, 309-323.

Walker, D.A., Halfpenny, J.C., Walker, M.D., & Wessman, C.A., (1993). Long-term studies of snow-vegetation interactions. *Bioscience*, *43*(5), 287-301.

Winther, J.G., & Hall, D.K. (1999). Satellite-derived snow coverage related to hydropower production in Norway: Present and future. *International Journal of Remote Sensing*, *20*(15-16), 2991-3008.

Zhang, T., (2005). Influence of the seasonal snow cover on the ground thermal regime: An overview. *Reviews of Geophysics*, *43*: RG4002.

CHAPTER 6

CONCLUSIONS

Work presented in Chapters 2-5 demonstrates the utility of Landsat and other moderate to high spatial resolution multispectral instruments for mapping both seasonal snow cover and persistent ice and snow cover such as glaciers and perennial snowfields. While the approaches described in Chapters 3-5 for mapping persistent ice and snow cover, snow covered area in forested areas, and mean snow cover duration have been validated, additional innovation and adjustments will likely lead to further improvements in product accuracy. There are two specific avenues of research with strong potential for improving Landsat-derived snow cover data products. First, snow covered area mapping algorithms should be extended to work with data from similar multispectral sensors such as the Operational Land Imager (onboard Landsat 8) and the European Space Agency's Sentinel-2 instrument. Extension of the basic algorithms, including the TMSCAG spectral unmixing algorithm, the forest canopy adjustment approach, and the approach for mapping persistent ice and snow cover will be relatively straightforward. However, comprehensive assessment of differences between products resulting from differences in the spectral and spatial resolutions of these sensors will be necessary. In particular, the reduced potential for radiometric

saturation in the visible bands provided by Landsat 8 and Sentinel-2 relative to Landsat 5/7 may have a substantial impact on the retrieval of snow covered area and could bias change analysis that incorporates data from both sensors if not explicitly addressed.

Extension of the algorithms presented here to sensors with similar spatial resolutions and spectral bands will be essential for maximizing the available data for analysis, particularly in regions where cloud-free views of the earth surface are relatively scarce. Ideally, snow cover products will eventually incorporate data from multiple sensors with different capabilities. Combining Landsat-derived snow cover with data from optical remote sensing instruments with significantly different spatial resolutions (e.g., MODIS, VIIRS) offers the potential for providing snow covered area products with better temporal resolution. Finally, combination of data from Landsat, other types of instruments such as radar or lidar, and physically-based snow cover modeling enables the estimation of snow water equivalent, perhaps the most sought-after snow metric.

The science data products described in Chapters 3-5 have a wide array of potential uses across a variety of disciplines. These datasets can improve our understanding of basic snow processes as well as the variability of snow and ice cover in the recent past and into the future. While a comprehensive discussion of potential scientific questions these datasets could help answer is beyond the scope of this work, several of the most pressing questions and research applications that could benefit from Landsat-derived snow cover data are outlined below.

Landsat-derived snow cover datasets are particularly valuable for providing a comprehensive inventory of snow cover across the full range of elevations, slope-aspect combinations and vegetation types present throughout a region such as an individual mountain range. Remotely sensed snow cover data are also crucial for monitoring snow cover above the treeline, where in situ observations are typically sparse or nonexistent. While other remotely sensed snow cover products, such as the MODIS snow products, can also provide this type of comprehensive inventory, Landsat's higher spatial resolution provides a unique opportunity to assess the relationship between snow cover duration and landscape characteristics such as slope, aspect, topographic position, and vegetation type and density. The higher spatial resolution snow cover data can be used to assess changes in snow cover duration for specific landscape types or positions over time. For example, recent research suggests that under future warming scenarios, topographic effects will have a strong impact on the timing of snowmelt (and resulting streamflow), with areas subject to topographic shading potentially more resistant to earlier snowmelt brought on by warmer temperatures (Lundquist & Flint, 2006). Landsat-derived snow cover duration data have the potential to provide a detailed assessment of this hypothesis. In another example, assessment of the spatial patterns of snow cover duration can also provide insight into the physical processes impacting snow accumulation, redistribution, and accumulation. Arctic and alpine environments typically experience substantial redistribution of snow by wind transport, resulting in substantial snow cover heterogeneity at scales < 100 m (Liston, 1998; Pomeroy, 2004). In recent years, understanding and modeling physical processes like wind

redistribution of snow has been a top priority for snow researchers. Landsat-derived patterns of snow cover duration can be used to validate and improve physically-based snow evolution models. These models will in turn be useful for forecasting changes in snow cover that will accompany forecasted changes in temperature and precipitation.

The comprehensive, high spatial resolution snow cover duration datasets derived from Landsat can also be used to identify areas of persistent ice and snow cover, such as glaciers and perennial snow cover, as demonstrated in Chapters 3 and 4. While automated identification of areas of PISC for a single time period represents a significant step forward, the next step is to monitor changes in persistent ice and snow cover over time. While numerous efforts have already explored changes in glacier area for various regions and over various periods of time, the use of automated techniques that exploit the full Landsat data archive will allow this process to be standardized and extended to regions where previous analysis has not been conducted. The creation of regional 30 m resolution datasets at regular temporal intervals can provide further insight into the processes responsible for changes in glaciers by examining the distribution of changes in relation to topography. For example, glaciers with accumulation zones in protected cirque basins (ideal for both enhanced accumulation and reduced insolation) are often less responsive to regional climate signals (Hoffman et al., 2007). Landsat-derived PISC datasets can be used to test this and other hypotheses. Insights derived from this type of analysis can be applied to improve predictions of change for individual glaciers and snowfields.

Landsat-derived snow cover duration datasets can also be used to assess the impact of changes in snow cover duration on the distribution of plant communities. Research has demonstrated feedback loops between snow cover and vegetation often play a role in the establishment of shrubs in arctic tundra (Sturm et al., 2001; Sturm et al., 2005) and trees in alpine tundra (Bekker, 2005; Moir et al., 1999). Since these types of land cover conversion typically occur incrementally and begin as changes isolated to small patches < 100 x 100 m in size, changes occurring since the establishment of satellite remote sensing programs are best observed at finer spatial resolutions such as the 30 m resolution of Landsat. Finally, the detailed patterns of snow cover duration available from Landsat provide the opportunity to assess the impact of snow cover patterns on animal movement, habitat preferences, and reproductive success. For example, ungulates often search out landscape patches with the shallowest snow cover (Ball et al., 2001). Snow cover duration combined with physically-based snow modeling can be used to reconstruct depth and snow water equivalent (Molotch, 2009), over the course of a winter and identify these areas. In another example, caribou often seek out late lying snow patches (easily identified from a Landsat-derived snow cover duration product) for protection from mosquitos during the spring calving season.

The individual questions and scientific applications addressed here represent only a limited subset of those that can be explored using Landsat snow cover data. In summary, the high spatial resolution, wall-to-wall coverage, and relatively long period of record of the Landsat sensors have the potential to provide insight into changing snow and ice cover conditions across arctic, alpine, and

montane systems that would not be possible using limited in situ observations or coarser resolution remote sensing data.

6.1 References

Ball, J.P., Nordengren, C., & Wallin, K. (2001). Partial migration by large ungulates: Characteristics of seasonal moose Alces alces ranges in northern Sweden. *Wildlife Biology*, *7*(1), 39-47.

Bekker, M.F. (2005). Positive feedback between tree establishment and patterns of subalpine forest advancement, Glacier National Park, Montana, USA. *Arctic, Antarctic, and Alpine Research*, *37*(1), 97-107.

Essery, R., & Pomeroy, J. (2004). Vegetation and topographic control of wind-blown snow distributions in distributed and aggregated simulations for an Arctic tundra basin. *Journal of Hydrometeorology*, *5*(5), 735-744.

Hoffman, M.J., Fountain, A.G., & Achuff, J. M. (2007). 20th-century variations in area of cirque glaciers and glacierets, Rocky Mountain National Park, Rocky Mountains, Colorado, USA. *Annals of Glaciology*, *46*(1), 349-354.

Liston, G.E., & Sturm, M. (1998). A snow-transport model for complex terrain. *Journal of Glaciology*, *44*(148), 498-516.

Lundquist, J. D., & Flint, A.L. (2006). Onset of snowmelt and streamflow in 2004 in the western United States: How shading may affect spring streamflow timing in a warmer world. *Journal of Hydrometeorology*, *7*(6), 1199-1217.

Molotch, N.P. (2009). Reconstructing snow water equivalent in the Rio Grande headwaters using remotely sensed snow cover data and a spatially distributed snowmelt model. *Hydrological Processes*, *23*(7), 1076-1089.

Moir, W.H., Rochelle, S.G., & Schoettle, A.W. (1999). Microscale patterns of tree establishment near upper treeline, Snowy Range, Wyoming, USA. *Arctic, Antarctic, and Alpine Research*, 379-388.

Sturm, M., Holmgren, J., McFadden, J.P., Liston, G.E., Chapin III, F.S., & Racine, C.H. (2001). Snow-shrub interactions in Arctic tundra: A hypothesis with climatic implications. *Journal of Climate*, *14*(3), 336-344.

Sturm, M., Schimel, J., Michaelson, G., Welker, J.M., Oberbauer, S.F., Liston, G.E., ... & Romanovsky, V. E. (2005). Winter biological processes could help convert arctic tundra to shrubland. *Bioscience*, *55*(1), 17-26.